INFORMATION TO USERS

This manuscript has been reproduced from the microfilm master. UMI films the text directly from the original or copy submitted. Thus, some thesis and dissertation copies are in typewriter face, while others may be from any type of computer printer.

The quality of this reproduction is dependent upon the quality of the copy submitted. Broken or indistinct print, colored or poor quality illustrations and photographs, print bleedthrough, substandard margins, and improper alignment can adversely affect reproduction.

In the unlikely event that the author did not send UMI a complete manuscript and there are missing pages, these will be noted. Also, if unauthorized copyright material had to be removed, a note will indicate the deletion.

Oversize materials (e.g., maps, drawings, charts) are reproduced by sectioning the original, beginning at the upper left-hand corner and continuing from left to right in equal sections with small overlaps.

Photographs included in the original manuscript have been reproduced xerographically in this copy. Higher quality 6" x 9" black and white photographic prints are available for any photographs or illustrations appearing in this copy for an additional charge. Contact UMI directly to order.

Bell & Howell Information and Learning
300 North Zeeb Road, Ann Arbor, MI 48106-1346 USA
800-521-0600

THE ROLE OF VANADIUM AS A HOMOGENEOUS CATALYST

IN

ALKALINE WATER ELECTROLYSIS

by

Joseph Law

A Thesis Submitted in Partial Fulfillment of The Requirements for the
Master's Degree of Applied Science and Engineering
Department of Chemical Engineering and Applied Science
University of Toronto

Acknowledgments

My deepest gratitude goes to my supervisors, Professor D.W. Kirk and Professor S.J. Thorpe for providing me with guidance, encouragement and an opportunity to conduct research under their supervisions.

I am indebted to Christopher Ho and Alan Tong who have given me countless help for my computer problems that have improved the thesis in so many ways. Dr. J.W. Graydon, Rami Abouatallah , Cam Nhan, Gus Abouatallah, Dave Anthony, Mike Stemp, Roger Cheuk and Daniel Lumanauw also deserve my special thanks for their everyday help and invaluable suggestions on my work.

I would like to thank Fred Neub and Sal Boccia for their help in using the SEM machine, and I would also like to thank Dan Tomchyshyn, Paul Jowlabar and my colleagues in Chemical Engineering for their help and suggestions.

I would like to thank the Electrolyser Corporation and the Ontario Center for Material Research (OCMR) for funding the project.

Finally, I would like to acknowledge the enthusiastic support and assistance given to me by my parents throughout the years of my Master's study.

University : University of Toronto

Title : The Role of Vanadium as a Homogeneous Catalyst in Alkaline Water Electrolysis

Student : Joseph Chun Wai Law M.A.Sc., Department of Chemical Engineering, 1998

Abstract

The effect of addition of vanadium as a catalyst to the electrolyte in alkaline water electrolysis for the hydrogen evolution reaction on Ni-200 and $Ni_{50}Co_{25}P_{15}B_{10}$ was investigated. Chronopotentiometry of catalyst concentration ranged 10 to 1000ppm showed an induced change of potential at the Ni-200 cathode which led to a final potential of -1800mV compared a potential of about -2000mV without catalyst. The same potential was reached for $Ni_{50}Co_{25}P_{15}B_{10}$ cathodes with 50 to 500ppm catalyst additions. Fe in the electrolyte lowered the overpotential and increased the vanadium catalytic effect slightly to -1710mV. Change in Tafel slope for Ni-200 electrodes after catalyst addition showed a reaction mechanism change. Ni-200 electrodes deactivated as step time of Tafel measurement increased. Electrode surface analysis by SEM showed similar coating morphology for both Ni-200 and $Ni_{50}Co_{25}P_{15}B_{10}$ electrodes. EDX, XRD and XPS showed the coatings were composed of mixed vanadium species in the V^{3+} and V^{5+} states.

Table of Contents

ACKNOWLEDGMENTS ii

ABSTRACT iii

TABLE OF CONTENTS iv

LIST OF TABLES vii

LIST OF FIGURES viii

1. INTRODUCTION 1

1.1 History of Water Electrolysis 1

1.2 Hydrogen Production Processes 2
1.2.1 Steam Methane Reforming of Natural Gas 5
1.2.2 Gasification of Coal 5
1.2.3 Electrolysis of Water 6
1.2.4 Thermochemical Processes 10
1.2.5 Photochemical and Photoelectrochemical Processes 11
1.2.6 Photobiological Production of Hydrogen 12

1.3 Electrolyser Designs 12
1.3.1 Unipolar Electrolyser Design 12
1.3.2 Bipolar Electrolyser Design 16

1.4 Electrode Materials for Alkaline Water Electrolysis 20
1.4.1 Nickel 20
1.4.2 Amorphous Alloys 23

1.5 Homogeneous Catalysis in Electrolysis 25

2. OBJECTIVES 29

3. THEORETICAL SECTION 30

3.1 Hydrogen Evolution Reaction in Alkaline Solutions 30

4. EXPERIMENTAL PROCEDURE 35

4.1 Equipment 35

4.2 Materials 37

4.3 Methods 38
4.3.1 Preparation of Nickel Electrodes 38
4.3.2 Preparation of Amorphous Nickel Alloy Electrodes 38
4.3.3 Preparation of Potassium Hydroxide Electrolyte 39
4.3.4 Experimental Procedure 39
4.3.5 Tafel Measurements 41
4.3.6 Analytical Methods 42

4.4 Safety 43

5. RESULTS 45

5.1 Ni-200 46
5.1.1 Ni-200 46
5.1.2 Ni-200 with 10 ppm Catalyst Addition 48
5.1.3 Ni-200 with 50 ppm Catalyst Addition 51
5.1.4 Ni-200 with 100 ppm Catalyst Addition 53
5.1.5 Ni-200 with 500 ppm Catalyst Addition 55
5.1.6 Ni-200 with 0.1 and 1000 ppm Catalyst Addition 57
5.1.7 Effect of Catalyst Concentration 61
5.1.8 Tafel Test for Ni-200 and Ni-200 with 100 ppm Catalyst Addition 63
5.1.9 Effect of Method of Catalyst Addition 64
5.1.10 Effect of Impurities 67
5.1.11 XRD and XPS Analysis on Electrode Surface 70

5.2 Ni-base Amorphous Alloy ($Ni_{50}Co_{25}P_{15}B_{10}$) 76
5.2.1 Ni-base Amorphous Alloy 76
5.2.2 $Ni_{50}Co_{25}P_{15}B_{10}$ with 50 ppm Catalyst Addition 77
5.2.3 $Ni_{50}Co_{25}P_{15}B_{10}$ with 100 ppm Catalyst Addition 80
5.2.4 $Ni_{50}Co_{25}P_{15}B_{10}$ with 500 ppm Catalyst Addition 82
5.2.5 Effect of Catalyst Concentration 84
5.2.6 Tafel Test for $Ni_{50}Co_{25}P_{15}B_{10}$ and $Ni_{50}Co_{25}P_{15}B_{10}$ with 100 ppm 86
5.2.7 XRD Analysis on Ni-base Amorphous Alloy Electrode Surface 87

5.3 Comparison of Ni-200 with $Ni_{50}Co_{25}P_{15}B_{10}$ Results 89
5.3.1 Effect of Catalyst Concentration with Different Electrode Materials 89
5.3.2 Tafel results with Different Electrode Materials 90
5.3.3 Morphology of the Coatings on different Electrode Materials 93

6. DISCUSSION 95

6.1 Ni-200 95
6.1.1 Steady State Potentiostatic Measurement (Tafel) 95
6.1.2 Scanning Electron Microscopy (SEM) with EDX 98
6.1.3 Catalyst Coated Electrodes 98
6.1.3.1 Chronopotentiometry 98
6.1.3.2 Steady State Potentiostatic Measurements 102
6.1.3.3 Scanning Electron Microscopy (SEM) with EDX 103
6.1.3.4 X-ray Photoelectron Spectroscopy (XPS) and XRD 105
6.1.4 Effect of Method of Catalyst Addition 107
6.1.4.1 Chronopotentiometry 108
6.1.4.2 Scanning Electron Microscope (SEM) with EDX 109

6.2 Amorphous Nickel Base Alloy ($Ni_{50}Co_{25}P_{15}B_{10}$) 109
6.2.1 Steady State Potentiostatic Measurements (Tafel) 110
6.2.2 Scanning Electron Microscopy (SEM) with EDX 112
6.2.3 *Catalyst Coated Electrodes* 112
6.2.3.1 Chronopotentiometry 112
6.2.3.2 Steady State Potentiostatic Measurements (Tafel) 113
6.2.3.3 Scanning Electron Microscopy (SEM) with EDX and XRD 115

6.3 Effect of Pre-electrolysis of Electrolyte 116
6.3.1 Chronopotentiometry 116
6.3.2 Scanning Electron Microscopy (SEM) with EDX 117

6.4 Proposed Reaction Mechanism of Catalysis Process 118

7. CONCLUSIONS 124

8. REFERENCES 126

Appendix A - Calculation for Hydrogen Equilibrium Potential, ϕ, at 70°C I
Appendix B - Calculation of Equilibrium Potential of Hg/HgO versus SHE at 25°C III
Appendix C - Calculation of pH V
Appendix D - Calculation of the Amount of Hydrogen Diffused into Nickel VI
Appendix E - Calculation of Electrode Area Enhancement by the Coating VIII
Appendix F - Modification of Data Compiling Program IX
Appendix G Sample Calculation of Coating Thickness X

List of Tables

Page

Table 1 : Commercial Water Electrolyser Manufacturers List 8

Table 2a,b : Nickel Cathodes Activity in 30 w/o KOH at Different Temperatures 21

Table 3 : Tafel Parameters for the HER on a Ni Electrode at Different Overpotentials 22

Table 4 : Tafel Slopes for the HER on Amorphous Alloys 24

Table 5 : Nominal Composition of Commercial Ni-200 37

Table 6 : SEM and EDX Settings 42

Results

Table 5.1.1 : Literature and Experimental Values of XRD Peak Values, d, of Nickel and Several Vanadium Oxides 71

Table 5.1.2 : Literature Values of XPS Binding Energies of Several Vanadium Oxides 73

Table 5.1.3 : Experimental Binding Energies for Vanadium Species for Catalyst Modified Ni-200 Electrode Surface 75

Table 5.3.1 : Tafel Parameters of Ni-200 and $Ni_{50}Co_{25}P_{15}B_{10}$ with and without Catalyst 92

Discussion

Table 7 : Nickel Tafel Slopes in Different Overpotential Range and Temperatures 96

Table 8 : Binding Energies of Vanadium and Oxygen for XPS 106

Table 9 : $Ni_{50}Co_{25}P_{15}B_{10}$ Tafel Slopes in Different Overpotential Range 110

List of Figures

	Page
Fig. 1.1 : Sketch of Early Electrolysis Setup	1
Fig.1.2 : Breakdown of Worldwide Hydrogen Production Methods	4
Fig.1.3 : Typical Solid Polymer Electrolyte (SPE) Cell Setup	9
Fig.1.4 : Unipolar Electrolyser Plant	13
Fig.1.5 : Photo of Commercial Unipolar Electrolyser (A-250 Stuart Cell)	14
Fig.1.6 : Schematic of Unipolar Type Cell	15
Fig.1.7 : Schematic of Bipolar Type Cell	17
Fig.1.8 : Photo of Commercial Bipolar Electrolyser	19
Fig.1.9 : Nickel Cathode Current Density Behaviour Versus Time Before and After Addition of Sodium Molybdate to the Electrolyte	27
Fig.4.1 : Electrochemical Cell Setup	35
Fig.4.2 : Electronic Experimental Equipment Setup	36
Fig.5.1.1 : Chronopotentiometry of Ni-200 in 8M KOH at 70°C	46
Fig.5.1.2 : SEM Micrograph Showing As-polished Ni-200 Sample	47
Fig.5.1.3 : EDX Spectrum of As-polished Ni-200 Sample	47
Fig.5.1.4 : Chronopotentiometry of Ni-200 with 10ppm Vanadium Addition in 8M KOH at 70°C	49
Fig.5.1.5 : SEM Micrograph Showing Electrode Surface After 10ppm Catalyst Addition	50
Fig.5.1.6 : EDX Spectrum of Electrode Surface After 10ppm Catalyst Addition	50
Fig.5.1.7 : Chronopotentiometry of Ni-200 with 50ppm Vanadium Addition in 8M KOH at 70°C	51

Fig.5.1.8 : SEM Micrograph Showing Electrode Surface After 50ppm Catalyst Addition 52

Fig.5.1.9 : EDX Spectrum of Electrode Surface After 50ppm Catalyst Addition 52

Fig.5.1.10 : Chronopotentiometry of Ni-200 with 100ppm Vanadium Addition in 8M KOH at 70°C 53

Fig.5.1.11 : SEM Micrograph Showing Electrode Surface After 100ppm Catalyst Addition 54

Fig.5.1.12 : EDX Spectrum of Electrode Surface After 100ppm Catalyst Addition 54

Fig.5.1.13 : Chronopotentiometry of Ni-200 with 500ppm Vanadium Addition in 8M KOH at 70°C 55

Fig.5.1.14 : SEM Micrograph Showing Electrode Surface After 500ppm Catalyst Addition 56

Fig.5.1.15 : EDX Spectrum of Electrode Surface After 500ppm Catalyst Addition 56

Fig.5.1.16 : Chronopotentiometry of Ni-200 with 0.1ppm Vanadium Addition in 8M KOH at 70°C 58

Fig.5.1.17 : Chronopotentiometry of Ni-200 with 1000ppm Vanadium Addition in 8M KOH at 70°C 58

Fig.5.1.18 : SEM Micrograph Showing Electrode Surface After 0.1ppm Catalyst Addition 59

Fig.5.1.19 : EDX Spectrum of Electrode Surface After 0.1ppm Catalyst Addition 59

Fig.5.1.20 : SEM Micrograph Showing Electrode Surface After 1000ppm Catalyst Addition 60

Fig.5.1.21 : EDX Spectrum of Electrode Surface After 1000ppm Catalyst Addition 60

Fig.5.1.22 : Effect of Catalyst Concentration on Ni-200 Electrode Potential 61

Fig.5.1.23 : SEM Images of Electrode Surface with Different Vanadium Concentration Addition (Ni-200) 62

Fig.5.1.24 : Tafel Plot for Ni-200 63

Fig.5.1.25 : Tafel Plot for Ni-200 After 100ppm Vanadium Addition 63

Fig.5.1.26 : Chronopotentiometry of Ni-200 with Single and Multiple Vanadium Additions 65

Fig.5.1.27 : SEM and EDX Spectrum of Electrode Surface After Single and Multiple Catalyst Additions 66

Fig.5.1.28 : Effect of impurities on Chronopotentiometry of Ni-200 with 100ppm Vanadium Addition 68

Fig.5.1.29 : SEM and EDX Spectrum of Electrode Surface After Catalyst Addition Using Treated and Non-treated Electrolyte 69

Fig.5.1.30 : XRD Spectrum of Electrode Surface After Catalyst Addition 70

Fig.5.1.31 : XPS Spectrum of Ni-200 After Catalyst Addition Showing O1s Peak 72

Fig.5.1.32 : XPS Spectrum of Ni-200 After Catalyst Addition Showing V2p Peaks 72

Fig.5.2.1 : SEM Micrograph Showing As-polished $Ni_{50}Co_{25}P_{15}B_{10}$ Sample 76

Fig.5.2.2 : EDX Spectrum of As-polished $Ni_{50}Co_{25}P_{15}B_{10}$ Sample 77

Fig.5.2.3 : Chronopotentiometry of Amorphous Ni Alloy with 50ppm V Addition in 8M KOH at 70°C 78

Fig.5.2.4 : SEM Micrograph Showing Amorphous Alloy After 50ppm Catalyst Addition 79

Fig.5.2.5 : EDX Spectrum of Amorphous Alloy After 50ppm Catalyst Addition 79

Fig.5.2.6 : Chronopotentiometry of Amorphous Ni Alloy with 100ppm V Addition in 8M KOH at 70°C 80

Fig.5.2.7 : SEM Micrograph Showing Amorphous Alloy After 100ppm Catalyst Addition 81

Fig.5.2.8 : EDX Spectrum of Amorphous Alloy After 100ppm Catalyst Addition 81

Fig.5.2.9 : Chronopotentiometry of Amorphous Ni Alloy with 500ppm V Addition in 8M KOH at 70°C 82

Fig.5.2.10 : SEM Micrograph Showing Amorphous Alloy After 500ppm Catalyst Addition 83

Fig.5.2.11 : EDX Spectrum of Amorphous Alloy After 500ppm Catalyst Addition 83

Fig.5.2.12 : Effect of Catalyst Concentration on $Ni_{50}Co_{25}P_{15}B_{10}$ Electrode Potential 84

Fig.5.2.13 : SEM Images of Electrode Surface with Different Vanadium Concentration Additions ($Ni_{50}Co_{25}P_{15}B_{10}$) 85

Fig.5.2.14 : Tafel Plot on Amorphous Ni Alloy 86

Fig.5.2.15 : Tafel Plot for Amorphous Ni Alloy After 100ppm Catalyst Addition 86

Fig.5.2.16 : XRD Spectrum of Amorphous Ni Alloy Electrode Surface After Catalyst Addition 88

Fig.5.3.1 : Effect of Catalyst Concentration on Both Ni-200 and $Ni_{50}Co_{25}P_{15}B_{10}$ Electrode Potential 89

Fig.5.3.2 : Tafel Plot for Ni-200 at Different Sweep Rate 90

Fig.5.3.3 : Tafel Plot for Amorphous Ni Alloy and After 100ppm Catalyst Addition 91

Fig.5.3.4 : Tafel Plot for Amorphous Ni Alloy and Ni-200 After 100ppm Catalyst Addition 91

Fig.5.3.5 : SEM on Coated Surface of Ni-200 and $Ni_{50}Co_{25}P_{15}B_{10}$ at Different Catalyst Concentration 94

Fig.6.1 : EDX Spectrum on Coating of the Pt Pre-electrolysis Electrode 100

Fig.6.2 : Surface of a Raney Nickel Coated Electrode 121

Fig.6.3 : Surface of Vanadium Coated Electrode (100ppm Addition) 121

1. INTRODUCTION

1.1 History of Water Electrolysis

The process of electrolytic decomposition of water is one of the most important and interesting processes in the field of electrochemistry. It was discovered more than two hundred years ago. In the year 1789, Paets van Troostwijk and Deimann had released their observations on the decomposition of combined bodies by an electric spark. They claimed they had decomposed water by the electric spark into combustible air and vitalized air [1]. A few years later, J. W. Ritter [1] also recognized the relation between chemical and electrochemical phenomena in 1798. In fact, he was indeed the first to observe the decomposition of water by the application of an electric current. In 1800, two Englishmen, Nicholson and Carlisle [1] observed the evolution of gas took place when the water was decomposed into its constituents by electricity. They noticed that as long as the conducting wires were in contact with the water, one of the wires consisted of an unoxidizable metal which led to the idea of metal protection using electricity. The publication of Nicholson's

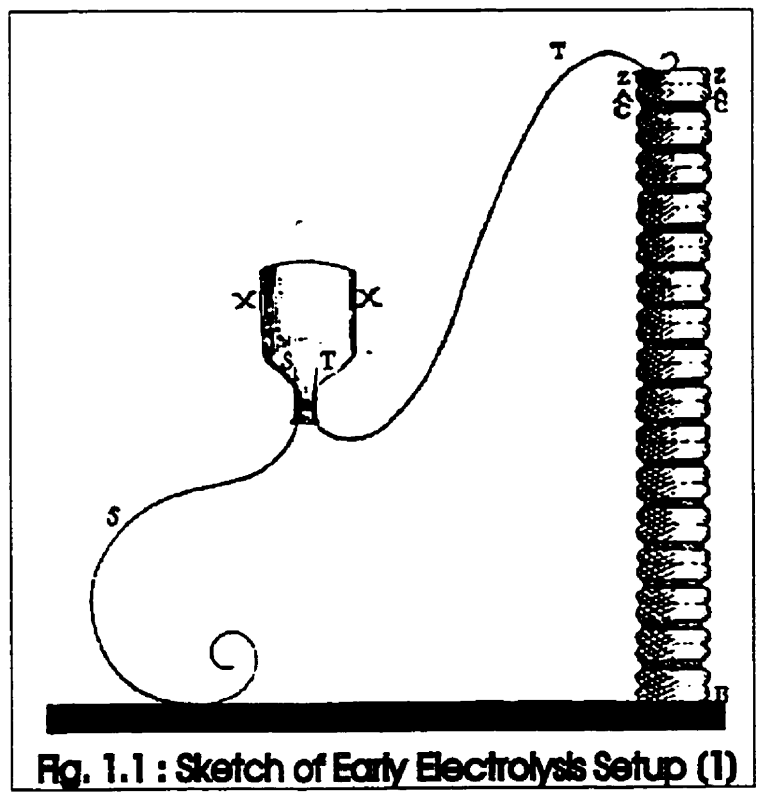

Fig. 1.1 : Sketch of Early Electrolysis Setup (1)

observations led others such as Landriani to repeat and explore the effects of the voltage pile setup on water electrolysis [1]. Fig. 1.1 shows the sketch of his apparatus with a series of copper zinc voltage piles.

1.2 Hydrogen Production Processes

A source of pure hydrogen is often needed in many industrial production processes, as well as in electrochemical and analytical laboratory applications. Hydrogen has its largest application in the petroleum industry. The Ontario Petroleum Association predicted that the refineries in Ontario alone may need 296 Mscf/d of hydrogen for hydrogenation processes and ammonia manufacture by the year 2015 [39], a more than 200% increase in thirty years. In metallurgical industries, hydrogen is used in reduction hydrogenation processes to obtain rare-earth metals and their alloys. Karpov *et al.* reported that by hydrogenation-dehydrogenation under a thermocycling process in hydrogen, a finely dispersed powder of hafnium-iron alloy was produced which could be further refined until the iron content was lower than 3% without any additional chemical processing methods [41]. This process increased the degree of extraction of the expensive hafnium, and thus lowered the production cost.

As the world's energy needs increase and the present "cheap" fossil energy source depletes, hydrogen can be considered as a clean energy carrier for the future. Hydrogen-powered vehicle development programs are underway in countries such as Germany, Japan, Canada and U.S.A. The need for these vehicles are increased as new environmental laws on exhaust emissions are being added by governments. There is the Zero Emission Vehicle Law of California. According to this law, about 10% of the cars

sold by major car companies in 2003 must have zero emission, which means electric cars or hydrogen cars [42]. Mercedes and Mazda have both developed their own hydrogen fueled vehicles [7]. City buses, converted from diesel buses to hydrogen fuelled ones, in countries such as Canada and Belgium are being tested [43] along with hydrogen powdered fuel cell buses (Ballard) in the U.S. and Canada. Hydrogen is stored in gaseous form as well as liquid form in the experimental cars. A detailed description of a hydrogen powered engine design is given by Peschka [44]. In addition, liquid hydrogen is used as the fuel to power rockets at NASA in the United States [6] and the space programs around the world, such as Russia, Europe, China, Japan and India [42].

Hydrogen applications also exist in other industries. The use of hydrogen as a fuel for torch brazing and soldering gives cleaner, less porous joints, a more directional and controllable flame, and greater safety for it is a low pressure system [2]. Liquid hydrogen has potential to use as a coolant for the refrigerators in vehicles. A liquid hydrogen refrigerator van has been developed by Yamane and his group in Japan [45]. In their design, liquid hydrogen is not only used as the cold fluid but also as the fuel for the van. The refrigerator box will maintain a temperature at 0 ± 5°C in order to carry fresh vegetables, fish or flowers to their markets. Other than earth-bound vehicles, liquid hydrogen aeroplanes are being developed. An International team comprising Russian, German and US companies is studying the production of an aircraft fueled by liquid hydrogen [46]. The design is for subsonic aircraft which can carry up to 400 passengers. Other countries like Britain and France both have similar plans to develop liquid hydrogen fueled hypersonic planes.

Since the worldwide demand for hydrogen is increasing significantly in a short time, considerable effort has been put in the research of better hydrogen generation, storage and utilization processes. Therefore, the technology used for industrial production of hydrogen has been improved in the past decades and various hydrogen production processes have been developed.

Steam reforming of natural gas is the most commonly used method of producing hydrogen. Water electrolysis is also well developed. Other processes such as thermochemical processes, photochemical and photoelectrochemical processes and photobiological production of hydrogen are being developed or investigated. Fig. 1.2 shows the percentage of worldwide hydrogen production used by each method.

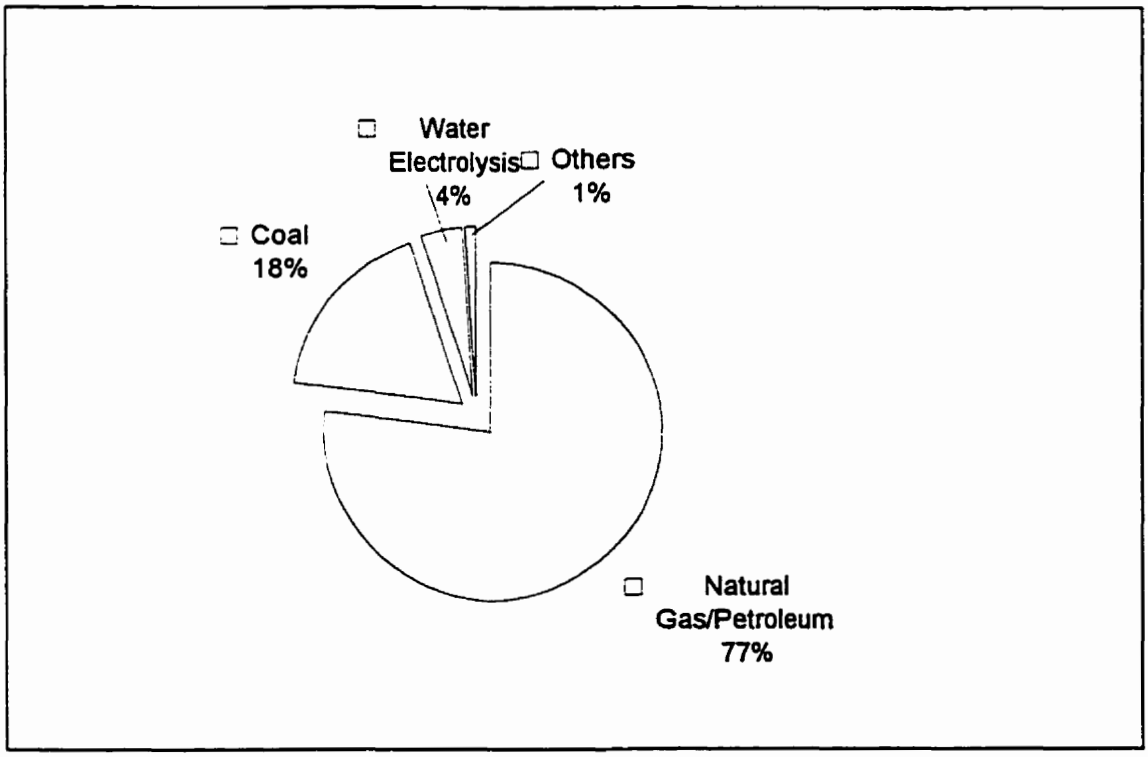

Fig. 1.2 Breakdown of Worldwide Hydrogen Production Methods [7]

A short description for each process is summarized in sections 1.2.1 to 1.2.6.

1.2.1 Steam Methane Reforming of Natural Gas

Steam reforming of natural gas provides almost 77% of the worldwide production of hydrogen. The process produces hydrogen from natural gas and water according to the following overall reaction:

$$CH_4 + 2H_2O \rightarrow CO_2 + 4H_2 \qquad (1)$$

Light hydrocarbon feeds ranging from natural gas to straight run saturated naphtha are also used in the process. First, the feed is desulfurized and then reacted with steam over a nickel catalyst in a reformer furnace and is converted to synthesis gases (H_2, CO and CO_2). The next step is to convert CO in the product gases to CO_2 and hydrogen by the water gas shift reaction :

$$CO + H_2O \rightarrow H_2 + CO_2 \qquad (2)$$

Chromium-promoted iron oxide catalyst is used in the first high temperature shift reactor (about 370°C). The converted gases are then cooled and sent to the low temperature shift converter (about 200°C). Copper-zinc oxide catalyst is used in this converter. The CO_2 in the product gases is scrubbed out by hot potassium carbonate. Finally, entrained water in the outlet gases is removed in a droplet separator. A typical hydrogen product is 98.2% H_2 and 1.8% CH_4, but maybe as low as 92-95% H_2 in some cases [7].

1.2.2 Gasification of Coal

Hydrogen from gasification of coal is well established, but is not as economically competitive as steam reforming of natural gas. The process follows reaction (3) as follows:

$$CH_{0.8} + 0.6H_2O + 0.7O_2 \rightarrow CO_2 + H_2 \qquad (3)$$

There are a number of coal gasification processes. They are differentiated by the type of gasifier and the operation conditions employed. Fixed bed, fluidized bed and entrained-flow are the three principle gasifier designs and the process can be operate at low, medium or high temperatures.

In a typical coal gasification process: coal, steam and oxygen are feed into the gasifier to produce the raw gas which will then undergo desulfurization. The synthesis gas will then go through shift conversion as in the steam reforming process. Finally, hydrogen gas is produced after the carbon dioxide removal process.

1.2.3 Electrolysis of Water

After the discovery of the water electrolysis process for oxygen and hydrogen production, a number of small and large scale electrolyzers were designed. In 1899, a German scientist, Dr. O. Schmidt invented the first industrial bipolar water electrolyzer in the form of a filter press like construction. A perspective view of the historical Schmidt electrolyzer can be found in reference [1]. The purity of the oxygen gas was 97 percent and the hydrogen gas was 99 percent [1]. This bipolar design is still used in modern water electrolyzers. There was another common design, the unipolar or tank-type electrolysis cell. The two electrolyzer designs generally have some common features; 20-30% solution of potassium hydroxide (KOH) in pure water as the electrolyte; the use of iron as a cathode and nickel or nickel-plated iron as an anode; and the use of an asbestos diaphragm to divide the cell compartments. The distinguishing difference between the unipolar and bipolar designs is the way that the individual electrolysis cells were assembled

[3]. More details of the designs will be given in the Section 1.3. Of the two designs, the bipolar cell has the greater industrial usage because it required less space and was believed to be less expensive. However, recent developments of the unipolar design have made the two technologies more competitive. Several international manufacturers offering commercial water electrolyzers are listed in Table 1 [4].

A third type of electrolyser was developed based on bipolar design. However, it uses a solid polymer electrolyte (SPE) instead of a caustic or acid liquid electrolyte. The SPE is composed of TFE Teflon linked sulfonic acid groups in the form of a plastic sheet. The sheet of SPE material is approximately 10 mils thick and a thin catalyst film is pressed on each face to form the anode and the cathode electrode [3]. A typical SPE electrolytic cell is shown in Fig. 1.3 as an example. This technology was first developed by General Electric as a fuel cell power source for the Gemini spacecraft. However, it was adapted for use as an electrolyser in the early 1970's. Typical applications of this design included spacecraft regenerative life support systems, oxygen generation systems for nuclear submarines and generation of pure hydrogen for laboratory use [3, 5]. The SPE has the physical characteristics of Teflon, but unlike Teflon, it has excellent ion exchange characteristics when saturated with water that make it highly conductive to hydrogen ions. Unfortunately, it is highly acidic and corrosive to material directly in contact with it. Therefore, expensive current collector and electrode materials must be used. Moreover, very pure feed water is required to avoid organic, biological and chemical undesirable products which may poison the electrolyte material. A more detail discussion of the design and performance of modern SPE electrolysers is given by Millet [47].

Table 1 : Commercial Water Electrolyser Manufacturers List [4]

Company	Type	Pressure	Status
1, Brown, Boveri & Cie	Bipolar, Alkaline	Atmospheric	Mature Technology
2, Constructors John Brown Development Ltd.	Bipolar, Alkaline	Atmospheric	Mature Technology
3, Denora S.P.A.	Bipolar, Alkaline	Atmospheric	Mature Technology
4, Krebskosao	Bipolar, Alkaline	Atmospheric	Mature Technology
5, Lurgi Apparate Technik GmbH	Bipolar, Alkaline	3 MPa	Mature Technology
6, Moritz Chemicals Engineering Ltd.	Bipolar, Alkaline	Atmospheric	Mature Technology
7, Norsk Hydro A.S.	Bipolar, Alkaline	Atmospheric	Mature Technology
8, Pintsh Bamag A.G.	Bipolar, Alkaline	Atmospheric	Mature Technology
9, Teledyne Energy System	Bipolar, Alkaline	0.7 MPa	Mature on small Scale
10, The Electrolyser Corp. Ltd.	Unipolar, Alkaline	Atmospheric	Mature Technology
11, BARC	Bipolar, Alkaline	2 MPa	Know how transferred to M/s.GMM. Protype under installation

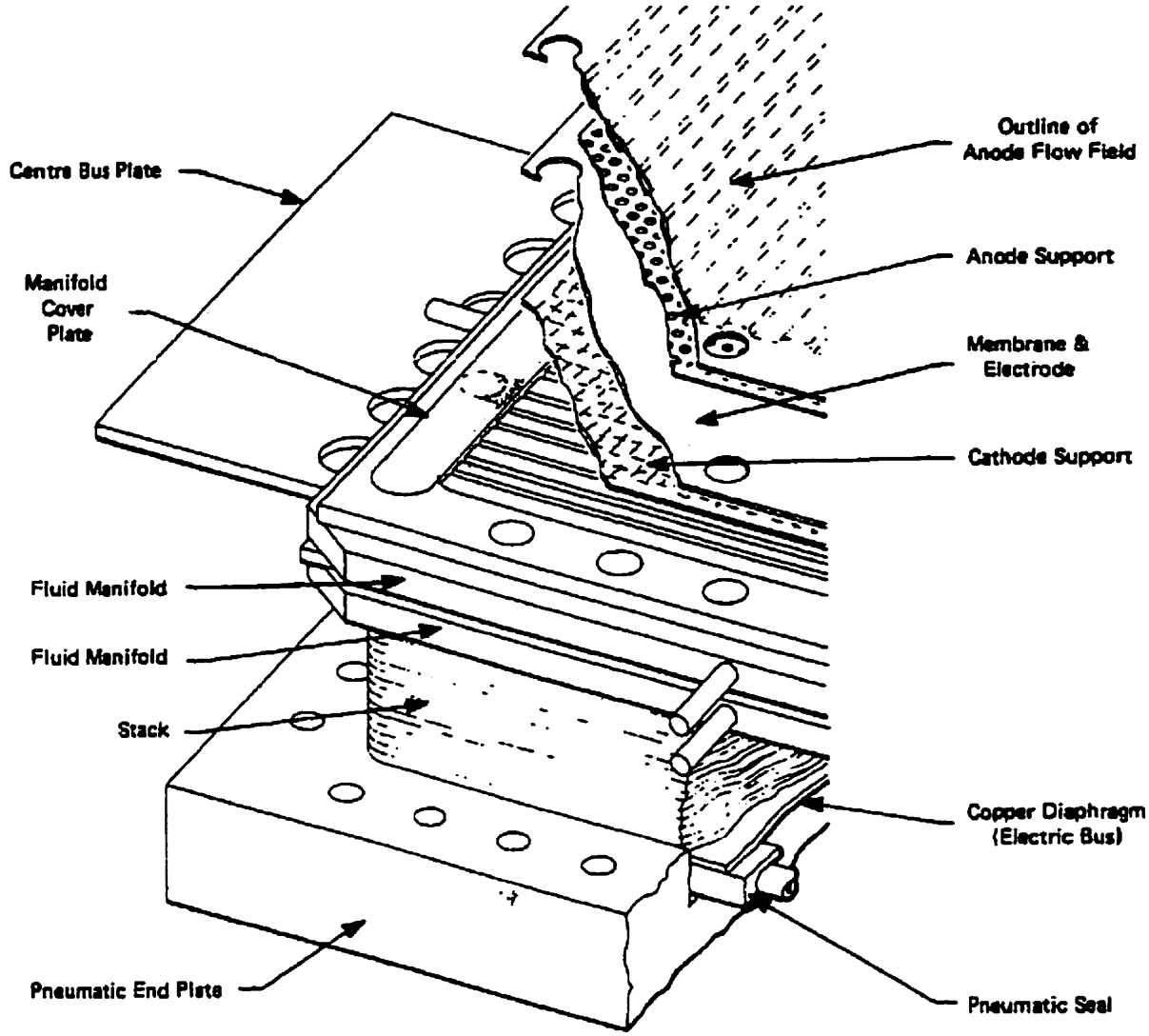

Fig. 1.3 : Typical Solid Polymer Electrolyte (SPE) Cell Setup [3]

1.2.4 Thermochemical Processes

Water can be decomposed into hydrogen and oxygen by direct thermal decomposition. Since the enthalpy of formation of water is very high, the decomposition needs an extremely high temperature, in excess of 3000 K, in order to carry out the process in one step. These temperatures are very difficult to manage and therefore, these thermochemical processes are all proposed to operate using a series of lower energy reaction combinations to provide hydrogen. All necessary steps, including recycling of all the intermediaries produced, represent a thermochemical cycle. With the help of computer programs, some 2000 to 3000 different cycles have been proposed [23]. However, most exist only on paper. A very few of the cycles have been examined in some detail. The Sulfur-Iodine cycle is an example which includes following three chemical reactions:

$$2H_2O(l) + SO_2(g) + xI_2 = H_2SO_4(sol) + 2HI_x(sol) \qquad 300K \qquad (4)$$

$$2HI_x(sol) = H_2(g) + xI_2(g) \qquad 600K \qquad (5)$$

$$H_2SO_4(g) = H_2O(g) + SO_2(g) + \frac{1}{2}O_2(g) \qquad 1100K \qquad (6)$$

It has been under development since 1974 [3, 24]. Some thermochemical processes are combined with electrolysis, which are called hybrid cycles. Sulfur-Bromine cycle is an example [3, 24]. In this cycle, HBr is decomposed into H_2 and Br_2 by electrolysis followed by two chemical reactions. Other cycles with more than three reactions were also developed. Calcium-Bromine-Iron cycle named UT-3 is an example which has been under development in the University of Tokyo since 1978 [24, 48]. Since a large quantity

of energy in the form of electrical energy, photon energy or chemical energy is needed to carry out these processes, they are not as practical as conventional alkaline water electrolysis.

1.2.5 Photochemical and Photoelectrochemical Processes

In photochemical processes, hydrogen is produced using water photolysis by solar radiation [3]. An example of a photolysis scheme is:

$$A + H_2O \overset{h\nu}{\Leftrightarrow} AO + H_2 \qquad (7)$$

$$AO \Leftrightarrow A + \frac{1}{2}O_2 \qquad (8)$$

where A is a catalyst. This method is still under development and the whole process is still not well understood. Catalysts like cerium ion and rhodium complex [3] are used in the process, but they are still in the research stage and no commercial product has been developed yet.

Photoelectrochemical process is based on the absorption of photons and generation of electron-holes in a semiconductor electrode in contact with an aqueous electrolyte. The hole moves to the surface of the semiconductor and reacts with water to release oxygen. Two protons (H^+ ions) migrate to the cathode and reduce to form a H_2 molecule [3, 23]. Titanium dioxide and gallium phosphide have been studied as the electrode materials. Problems are encountered in searching for a suitable semiconductor for this process since the semiconductors tend to be unstable under photoelectrolysis (photo-corrosion) while the more stable ones are poor in energy utilization for they are

mostly transparent. Commercializing this process would need further technological development to improve the electrode material.

1.2.6 Photobiological Production of Hydrogen

This method of hydrogen production has been demonstrated in laboratories. Hydrogen is produced from water or organic molecules using efficient biological converters, algae or photosynthetic bacteria and low cost photobioreactors. In order to obtain high hydrogen production rate, microalgae is used in photobioreactors which expose the contents to sunlight in a closed system allowing the recovery of gas [49].

The hydrogen production rate by this method is small. The upper efficiency of biophotolytic splitting of water into molecular hydrogen and oxygen by microalgae is found to be 11%. In non ideal conditions, with transmission or reflection of solar photons, the upper efficiency will become 6-8% only [50]. The research in this area is still in the early development stage [24, 49], but it could be of lower cost than other solar hydrogen production processes.

1.3 Electrolyser Designs

1.3.1 Unipolar Electrolyser Design

Unipolar or tank-type design includes a series of electrodes, anodes and cathodes. They are alternately suspended vertically and parallel to one another in a tank containing the electrolyte. Each electrode has the same polarity on both surfaces and carries out a single electrode process, i.e. either oxygen or hydrogen evolution. The electrodes are

connected in parallel in order to allow the tank to operate across a low voltage dc supply [3]. The resultant overall cell voltage is equivalent to that of one anode/cathode pair which is usually 1.7-2.0 V [21]. Asbestos, or an equivalent separate material acts as a diaphragm to separate anodes and cathodes. This prevents the passage of gas from one electrode compartment to another. Although the diaphragm is impermeable to gas, it is permeable to the electrolyte in order to offer the least resistance to the ion flow through the electrolytes. Copper bus bars are used to connect all the anodes and cathodes to form an electrolyzer unit. These units may be connected to form a bank of cells to give the desired hydrogen output.

The unipolar design has two major advantages. First, the cell is composed of few parts which are relative inexpensive. Second, the maintance or replacement of the cell is very simple. A weakness of the design is that the diaphragm may allow gas to diffuse through if pressure builds up during electrolysis affecting product gases purity. Also the plant size is bigger than that of a bipolar electrolyser plant. However, the recent improvements of the design has made its space requirements comparable to that of the bipolar design. A sample of a unipolar electrolysis plant (Standard Stuart-cell plant) layout is shown in Fig. 1.4 [21]. Currently, the major company supplying unipolar technology is the Electrolyser Corporation Ltd. of Etobicoke. Fig. 1.5 shows a commercial EI-250 alkaline water electrolyser and Fig 1.6 shows a schematic of the unipolar electrolyser [3].

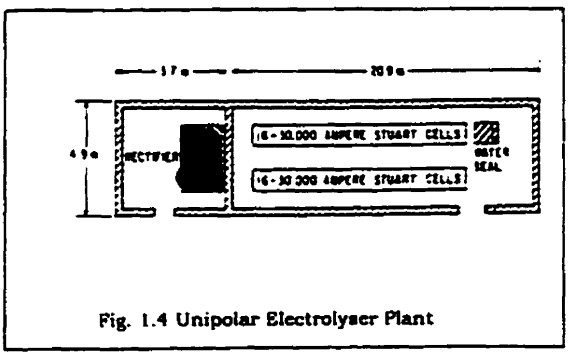

Fig. 1.4 Unipolar Electrolyser Plant

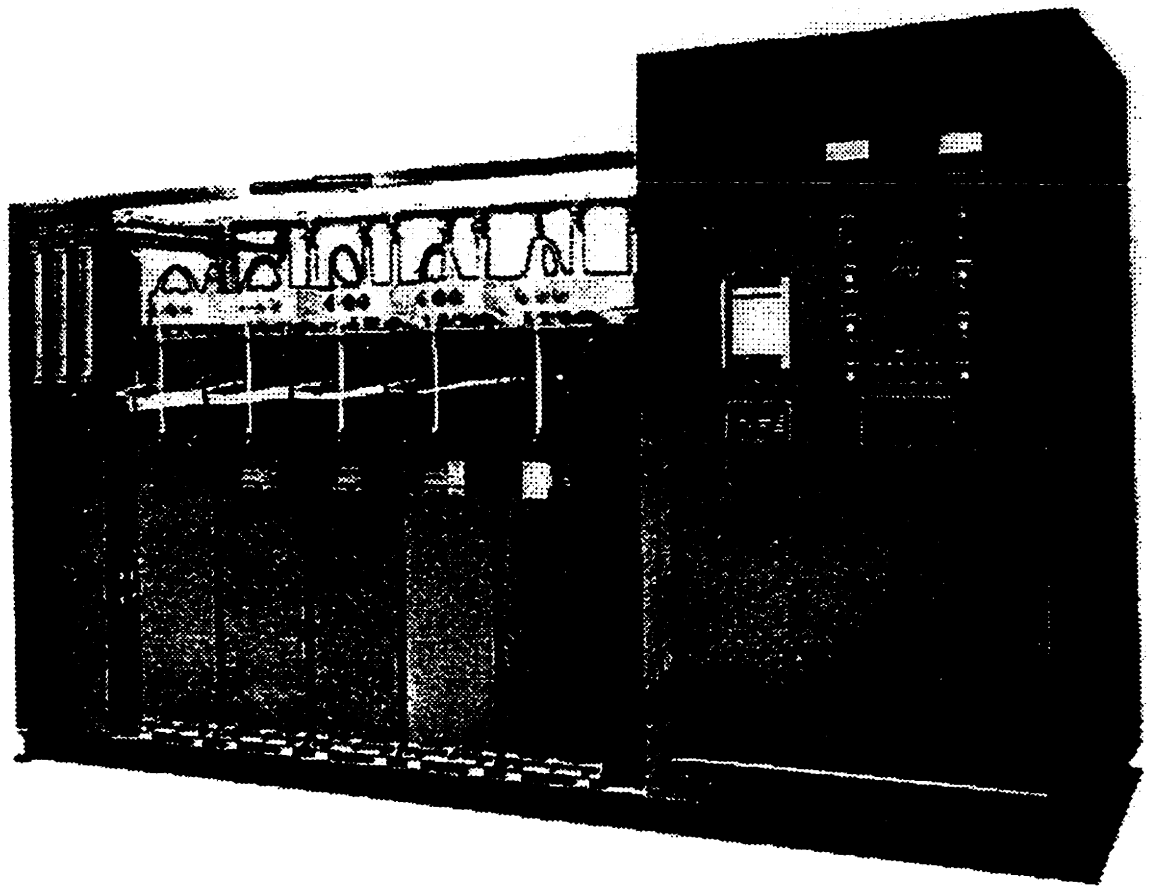

Fig. 1.5 Photo of Commercial Unipolar Electrolyser (A-250 Stuart Cell)

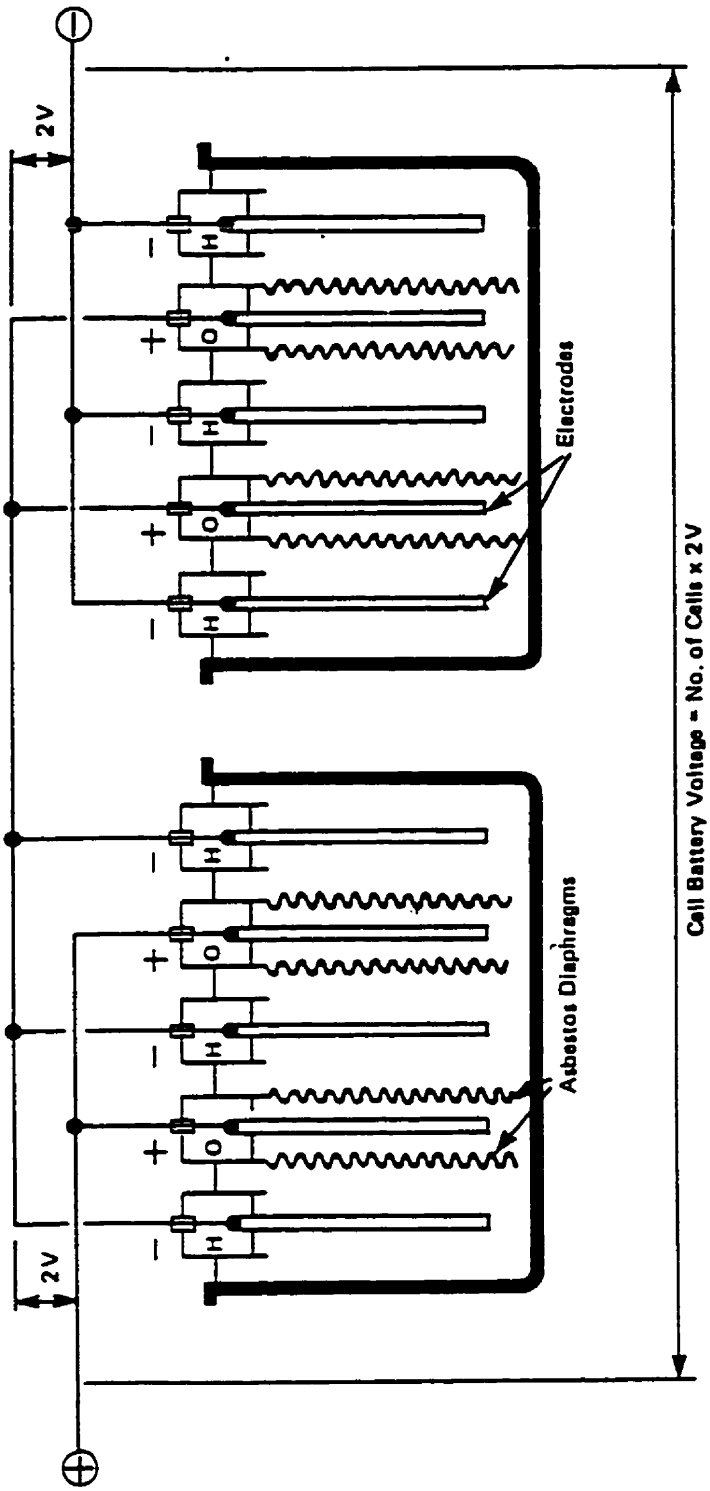

Fig. 1.6 Schematic of Unipolar Type Cell

1.3.2 Bipolar Electrolyser Design

Except for Solid Polymer Electrolyte electrolysers, all commercially available bipolar type of electrolyser are in the form of a plate and frame filter press. The design consists of a sandwich construction of a relatively large number of electrode plates, separator materials and gasket insulators. One side of the electrode plate acts as an anode in one cell and the other side of the plate acts as the cathode of the next cell. Each electrode is connected electrically in series with its neighbour. Diaphragms are used to separate each pair of electrodes which forms an individual cell unit. It was usually made of asbestos cloth reinforced with nickel wire. From each side of the diaphragm, there is a passage into one of the gas ducts which can be seen at the top rim of the diaphragm ring. An exploded view of one electrolyser cell can be found in reference [22]. The whole cell module is held together by a number of heavy longitudinal tie bolts. The direction of current flow is from one end of the cell pack to the other. A bipolar electrolyser may contain from thirty to several hundred individual cell unit in series at 1.7 to 2.0 V each. The corresponding applied voltage ranges from 50 to 600 V d.c. , depending on the required output capacity [21]. Fig. 1.7 shows a typical filter press construction of a bipolar electrolyser cells [3].

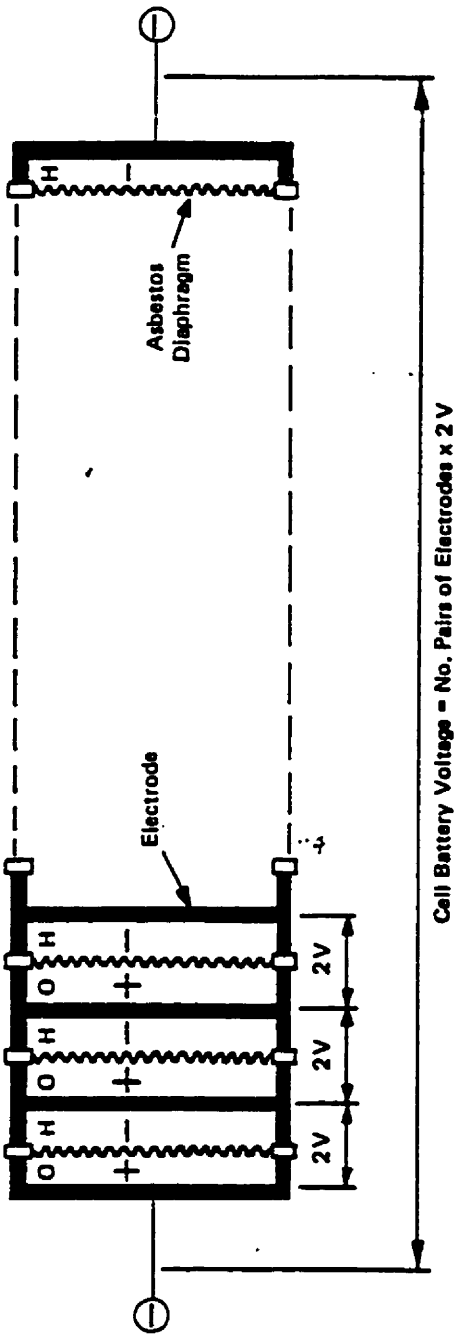

Fig. 1.7 Schematic of Bipolar Type Cell

The advantages of bipolar electrolyser design include:

- Moderate cell thickness with filter press assembly enables a fairly compact electrolyser to be built.
- A simple electrical arrangement in the cell.
- It does not require the intercell bus connections.
- The whole cell module takes up a relatively small floor space.

The disadvantage of the design is the cell maintenance. Since all the cells are connected in series, if one cell component fails, the entire stack has to be dismantled and removed from service for repair.

Most of the bipolar electrolysers operate at atmospheric pressure. The designs with elevated pressure pose higher safety risks, maintenance costs and more complicated start up and shut procedures which create more problems and are not commonly used. A photo of a typical bipolar electrolyser is shown in Fig. 1.8 [3].

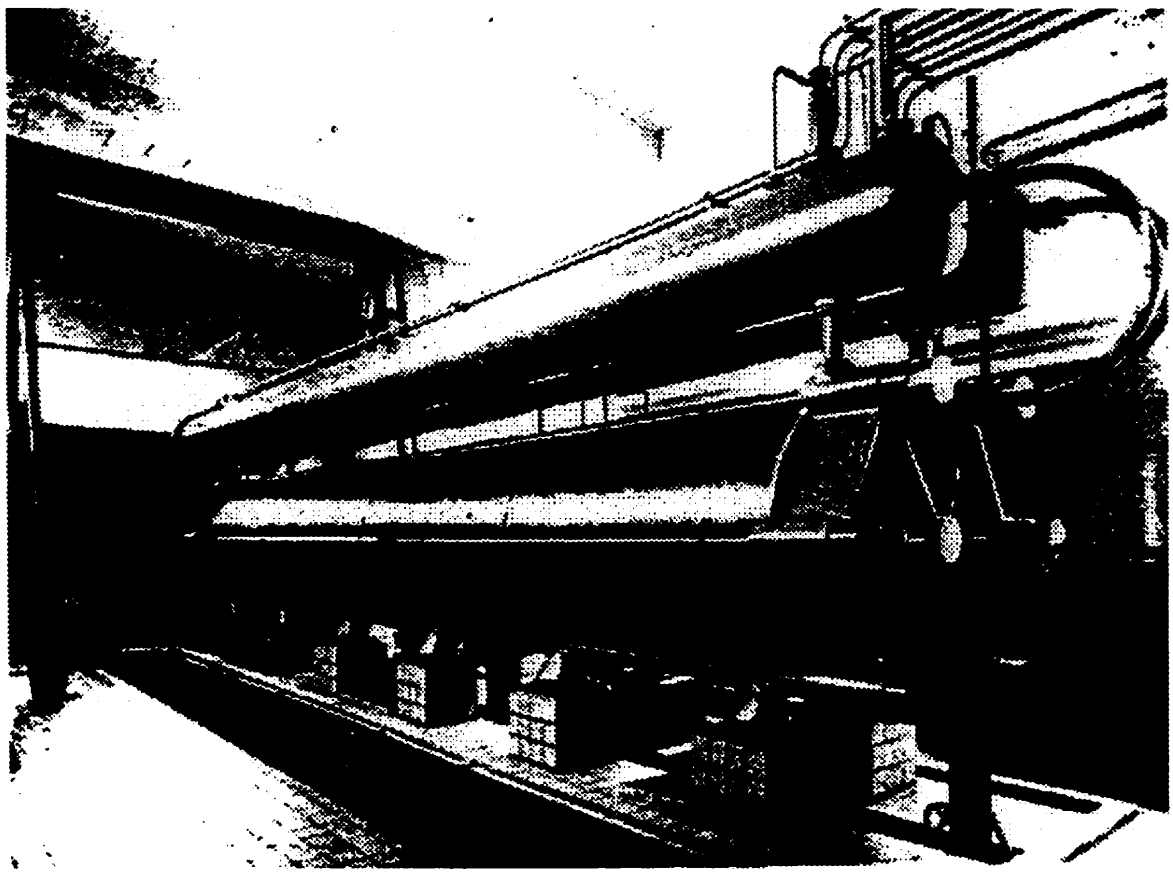

Fig. 1.8 : Photo of Commercial Bipolar Electrolyser

1.4 Electrode Materials for Alkaline Water Electrolysis

The choice of electrode materials is very important in order to obtain reliable, energy efficient, low cost electrolysis. There are a number of requirements in selecting a material for use as an electrode. Most importantly, it must have good electrode conductivity to minimize energy losses in the structure. Chemical and electrochemical stability is also required. Furthermore, low overpotential for the desired reaction is critical. In this thesis, nickel and a nickel base amorphous alloy developed at the University of Toronto were studied as cathode materials for the evolution of hydrogen.

1.4.1 Nickel

Nickel is widely used as electrode material in alkaline water electrolysis because of its corrosion resistance in high pH electrolytes and its low cost. Therefore, its performance for the hydrogen evolution reaction (HER) has been examined by a number of researchers [8, 26-30]. The HER mechanism in alkaline media consists of three reactions:

1. Hydrogen ion electrochemical adsorption reaction and,

2a. Electrochemical reaction to hydrogen molecules or,

2b. Chemical desorption reaction to hydrogen gas.

where reactions 2a and 2b are parallel competitive steps. A more detailed description is given in section 3.1. In general, it has been proposed that for nickel, reaction 1 would be the rate limiting step (rds) [26]. The Tafel slope (an indicator of the rds) calculated for step 1, gives a value of 120 mV/decade. A smooth nickel electrode is usually experimentally measured to be around 100-120 mV/dec. However, the slope is

temperature dependent. The following Table 2a shows the changes of Tafel slope with temperature data obtained by Huot [8].

Table 2a : Nickel Cathodes Activity in 30 w/o KOH at Different Temperatures [8]

Temperature (K)	Tafel Slope, b (mV/dec)	Tafel Slope, b (mV/dec) Theoretical (assuming step 2 is rds)
303	115	120
323	111	128
343	104	136
363	103	144

The different trend in the change of slope may due to the experimental condition, such as impurities in the electrolyte. Some other authors got more consistent trend with the theoretical predictions. Table 2b shows their results:

Table 2b : Nickel Cathodes Activity in KOH at Different Temperatures

Temperature (K)	Tafel slope (mV/dec.)	Conc. of KOH	Author
303	146	1M	61
363	159	1M	61
323	167	8M	70
350	166	8M	70

Apart from the temperature dependence, the Tafel slope also changes with the magnitude of the electrode overpotential. The following Table 3 shows the change of Tafel slopes obtained at different overpotentials by Kibria et al [26] and Lian et al [37].

Table 3 : Tafel Parameters for the HER on a Ni at Different Overpotentials

	Tafel Slope, b (mV/dec)	Temperature (K)	Author
Low Overpotentials (~ 100 - 200mV vs. Hg/HgO)	80	325	[26]
High Overpotentials (~ 200 - 400mV vs. Hg/HgO)	167	325	[26]
Low Overpotentials (~ 355 - 555mV vs. Hg/HgO)	148	303	[37]
High Overpotentials (~ 555 - 705mV vs. Hg/HgO)	96	303	[37]

The HER overpotential for smooth nickel electrodes increases with prolonged polarization. The cause of the change of the electrode activities has been reported to be due to atomic hydrogen absorption into the lattice of the nickel cathode [27, 31, 32]. From Rommal et al., the Tafel slope of nickel cathode after 1 minute of polarization was 100 mV/dec which would increase to 300 mV/dec after 6 hours of polarization [27].

1.4.2 Amorphous Alloys

Amorphous metallic alloys consist of two or more metals or metal-metalloids and are produced with no long range atomic order but with short range chemical ordering. They are made by rapid solidification so that the atoms are effectively frozen in their liquid configuration. The rate of cooling required ($\sim 10^6$ °C/s) is much greater than employed in conventional cooling techniques for solids. Methods for rapid cooling were first developed by Duwez [33]. These alloys have attracted attention for their superior electrical, magnetic, and chemical properties.

Much of the initial work on amorphous alloys focused on the improvement of corrosion resistance through the alloying of metals having good corrosion resistance. The corrosion rate of amorphous iron-metalloid alloys without a second metallic element is higher than that of crystalline pure iron. However, the corrosion rate is decreased by addition of a second elements such as chromium, vanadium, copper and nickel. Hashimoto has listed a few examples in his paper [36]. Since the composition of amorphous alloys can be controlled during the manufacturing process, they have potential use as electrocatalysts in the oxidation reaction of hydrocarbons [34, 35] or as electrodes for fuel cells [36]. However, the as-produced low surface area has limited their application.

Amorphous alloys have been studied as a HER electrode material. Similar to nickel, two Tafel slopes in low and high overpotential regions were found. The following Table 4 shows the Tafel slopes of some alloys Lian et al [37] and Suzuki [40] obtained from their experiments. In most of the alloys, two linear regions were found which was the same as Ni Tafel plot.

Table 4: Tafel Slopes for the HER on Amorphous Alloys

Materials	Tafel slope	(mV/dec.)
	b_1 Overpotential : ~ 355 - 555mV	b_2 Overpotential : ~ 555 - 705mV
$Co_{50}Ni_{25}Si_{15}B_{10}$ [37]	174 ± 7.4	124 ± 2.7
$Ni_{50}Co_{25}Si_{15}B_{10}$ [37]	178 ± 6.3	110 ± 6.5
$Ni_{50}Co_{25}P_{15}B_{10}$ [37]	144 ± 9.8	101 ± 9.2
Materials	Tafel slope (mV/dec.)	b, Overpotential range (mV)
$Ni_{72}Co_2Mo_6B_{20}$ [40]	114 ± 3	75 -505
$Ni_{72}Mo_8B_{20}$ [40]	175 ± 1	25 - 525
$Ni_{72}Co_6Mo_2B_{20}$ [40]	147 ± 2	0 - 465

All data obtained at 303K.

1.5 Homogeneous Catalysis in Electrolysis

Electrolysis is an established and proven process to convert water to hydrogen and oxygen. It is a very clean, reliable process and very pure hydrogen without inert gas contamination can be produced [6]. However, a significant fact in the overall cost of hydrogen produced by electrolysis is the cost of the electricity. The electricity used to drive the process is 3-5 times more expensive than fossil fuel-derived energy [7]. Therefore, research on lowering the energy required by reducing the hydrogen overpotential, the potential difference between the electrode potential and the reversible potential, in the electrolysis process is an ongoing process. Homogeneous catalysis, the subject of this thesis, is one of the techniques that might be used to lower the hydrogen overpotential. The catalysts can either produce metastable complexes in the electrolyte or absorb directly on the electrode surface. The cell voltage is then lowered through a reduction of the activation energy barrier.

A number of research papers have been done on the effect of the presence of metallic ions in the electrolyte for both the hydrogen evolution reaction [8-12] and oxygen evolution reaction [13-16]. In most industrial water electrolysers, there are always iron impurities present in the alkaline electrolyte. In view of this, the influence of iron impurities on the hydrogen and oxygen evolution reactions have received the most attention. For the hydrogen evolution reaction, iron was found to be deposited on the cathode surface which resulted in a change of the Tafel slope [11] and an improvement in the electrocatalytic activity towards the reaction [9-12]. Huot suggested that there were two consecutive steps for iron to deposit [8]: the reversible reduction of Fe^{3+} to Fe^{2+} followed by the reduction of Fe^{2+} to metallic iron at a hydrogen overpotential close to -

200 mV. Time is required for the iron to deposit. It took about 20 hours of cathodic polarization at a current density of 100 mA/cm^2 with 0.5 ppm of iron, Fe, in order to obtain an iron deposit on a platinum cathode. In order to cover most of the electrode surface, it would need more than eight days [12]. In addition to iron, other transition metals such as molybdenum and cobalt were also investigated.

In another study by Huot and Brossard [31], they reported that the galvanostatic deactivation of nickel cathode consisted of two stages, probably due to the change of the electrode surface. The first stage of deactivation is due to the hydrogen penetration in the metal lattice which induces hydride formation. The second region of deactivation is followed by a slight reactivation. With the increase in iron-rich deposit, the degree of deactivation increase with time after the reactivation. By adding molybdate into the electrolyte before the second deactivation, the second deactivation disappears. An active metallic form of molybdenum deposits on the electrode surface and is responsible for the activation process. A similar activation process was observed in potentiostatic tests. Fig. 1.9 shows the current density behaviour with time before and after the addition of 4×10^{-3} M of sodium molybdate to the 30 w/o KOH electrolyte at 70°C.

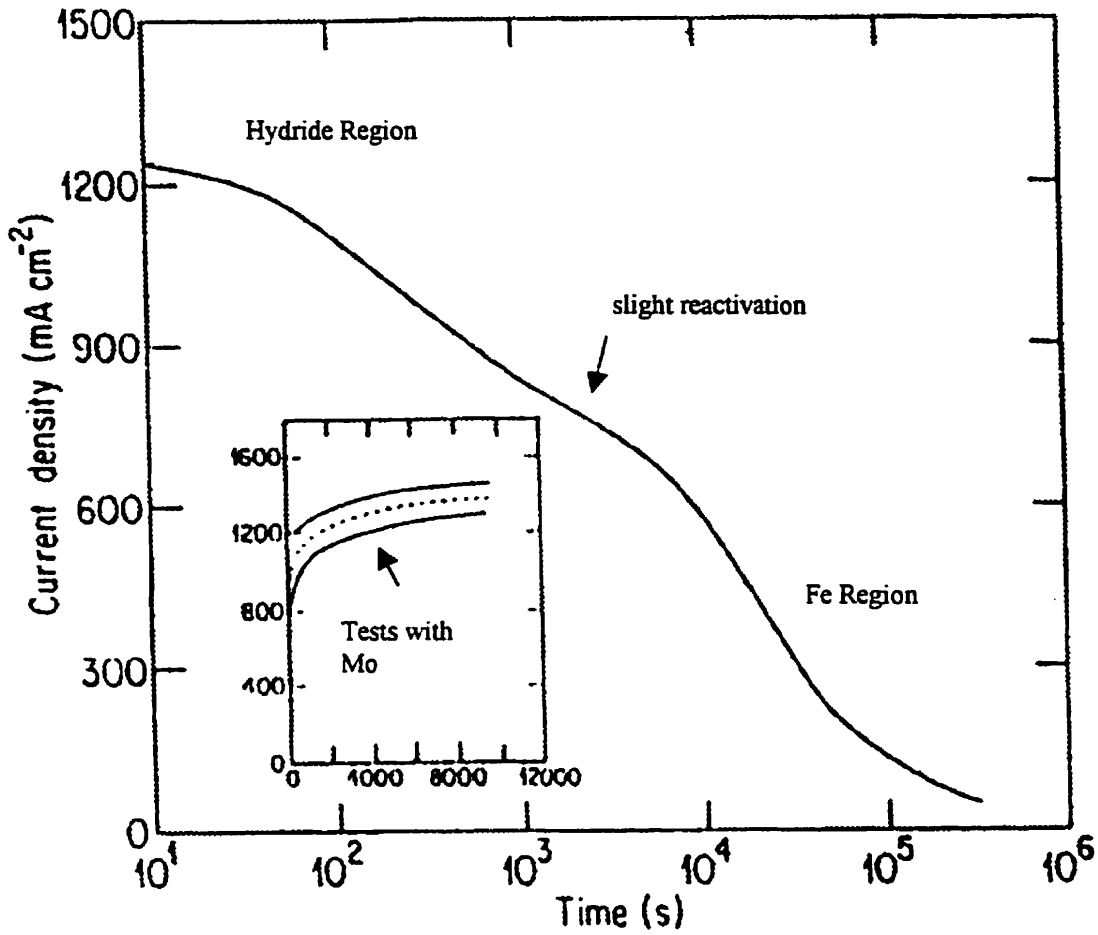

Fig. 1.9 : Nickel cathode current density behavior versus time before and (insert) after addition of sodium molybdate to the electrolyte at constant potential (-1.5 $V_{Hg/HgO}$) [9].

The curve shows a decrease in current density with time at a constant potential of -1.5 $V_{Hg/HgO}$. The dashed line in the small inserted graph shows the current density versus time after the addition of molybdate. The addition of molybdate results in a significant increase in current. For example, after 1.5 x 10^5 s of deactivation, the current density (original curve) was about ten times lower than it was at 10^4 s (insert curve) after the addition of molybdate.

Cobalt is another homogeneous catalyst. It is mostly used in catalyzing the oxygen evolution reaction [15, 51]. A Co-Cu coating by electrodeposition was also studied for

hydrogen evolution reaction [51]. It was found that the electrocatalytic activity (the overpotential of HER) is approximately the same as cobalt and copper wire electrodes. Most transition metals are reported to improve the hydrogen evolution reaction and the effect seems to be concentration dependent [12].

2. OBJECTIVES

The objectives of this work are:

1. to determine the role of a reported catalytic solution species, VO_4^{3-}, on the hydrogen evolution reaction under industrial alkaline water electrolysis conditions (8M KOH, 70°C and 250 mA/cm^2),
2. to determine the effect of electrode substrate by studying pure nickel and amorphous $Ni_{50}Co_{25}P_{15}B_{10}$ alloy on the difference of their electrochemical behaviour,
3. to determine the effect of catalyst concentration on electrode overpotentials,
4. to investigate possible reaction mechanisms for the catalysis process.

3. THEORETICAL BACKGROUND

3.1 Hydrogen Evolution Reaction in Alkaline Solutions

The hydrogen evolution reaction is one of the most important electrochemical processes. Intensive studies have been performed during the last few decades. A well known three reaction step mechanism for the hydrogen evolution reaction has been developed and used by many authors [17-20].

In alkaline solutions, the hydrogen evolution reaction generally proceeds via the following steps:

$$H_2O + M + e^- \Leftrightarrow MH_{ads} + OH^- \qquad \text{Volmer} \qquad (9)$$

$$MH_{ads} + H_2O + e^- \Leftrightarrow H_2 + OH^- + M \qquad \text{Heyrovsky} \qquad (10) \text{ or}$$

$$2MH_{ads} \Leftrightarrow H_2 + 2M \qquad \text{Tafel} \qquad (11)$$

where M represents the free metal surface, MH_{ads} represents the surface occupied by absorbed hydrogen. In this mechanism, there are two reaction pathways leading to hydrogen evolution. The hydrogen adsorption reaction (Volmer, (9)), occurs followed by either the electrochemical reaction (Heyrovsky, (10)) or the chemical desorption reaction (Tafel, (11)). For nickel, the hydrogen evolution reaction usually proceeds via the Volmer-Heyrovsky mechanism [18]. In addition, in the presence of hydrogen, a reaction representing transfer of surface-adsorbed hydrogen into the metal at the surface should also be added [18]

$$MH_{ads,surface} \Leftrightarrow MH_{abs,metal} \qquad (12)$$

Reaction (12) is then followed by hydrogen diffusion into the bulk of the metal phase. Reactions (9) to (11) cannot be separated from reaction (12) and are integral parts of the mechanism.

From the electrode mechanism, a transfer coefficient (α) can be calculated and compared with an experimentally determined value. The Butler-Volmer Equation is given by [25]:

$$i_{net} = i_o\left\{\exp\left(+\frac{\alpha_a F\eta_a}{RT}\right) - \exp\left(-\frac{\alpha_c F\eta_c}{RT}\right)\right\} \qquad (13)$$

where i_{net} - net current density (A/m^2)

i_o - exchange current density (A/m^2)

α_a, α_c - anodic and cathodic transfer coefficient

F - Faraday constant (C/mol)

η_a, η_c - anodic and cathodic electrode polarization (V)

R - molar gas constant (J/mol.K)

T - temperature (K)

It is a general expression which relates current density and electrode polarization (anodic and cathodic) for a multi-step electrode reaction. In situations where the polarization of one component (anodic or cathodic) is high enough, the current density component in the opposite direction can be neglected. In cathodic case, when the cathodic polarization is more negative than -100mV, the anodic term in equation (13) can be neglected. Equation (13) becomes:

$$\eta_{cat}^{act} = +\frac{2.303RT}{\alpha_c F}\log\left(i_{o,c}\right) - \frac{2.303RT}{\alpha_c F}\log|i_c| \qquad (14)$$

The subscript c means cathodic and i_c becomes equal to i_{net} . Equation (14) is the basis for the Tafel equation for a cathode. The same procedure can be used to reduce equation (13) to the Tafel equation for an anode. The two equations are in the form of :

$$\eta = a \pm b \log i \tag{15}$$

This is the Tafel Equation. In a Tafel plot where η is plotted versus log i, the slope of the plot gives the value of b in equation (15). Therefore,

$$Tafel\ slope = -\frac{2.303RT}{\alpha F} \tag{16}$$

So, the transfer coefficient can be obtained experimentally.

From the reaction mechanism, it can be shown that :

$$\alpha_c = \frac{\gamma}{\nu} + r\beta \qquad \text{Cathodic Transfer Coefficient} \tag{17}$$

$$\alpha_a = \frac{n-\gamma}{\nu} - r\beta \qquad \text{Anodic Transfer Coefficient} \tag{18}$$

$$\alpha_a + \alpha_c = \frac{n}{\nu} \tag{19}$$

where γ - the number of electron transfer steps occurring before the rate determining step (RDS)

n - the number of electrons transferred in one act of the overall reaction

β - the symmetry factor for the RDS (usually taken as β = 0.5)

r - a factor depending on the type of RDS:
r = 1 if the RDS is an electron transfer step; r = 0 if the RDS is a chemical step

ν - the number of times the RDS occurs in one act of the overall reaction.

In order to confirm a postulated reaction mechanism, Equation (15) to (19) are used to calculate what the transfer coefficient of the mechanism should be, and then the

actual transfer coefficient is determined experimentally to see if it is the same as the calculated value. If they are the same, the postulated mechanism is compatible with the actual mechanism, and maybe the actual mechanism [25].

Using the above procedure, the Tafel slope of the hydrogen evolution reactions at 298K can be calculated as follows:

1, Using Volmer reaction as the RDS of the mechanism:

γ	ν	*r*	β
0	1	1	0.5

Insert the above values into equation (17), the cathodic transfer coefficient, α_c is calculated to be 0.5. Then insert this value into equation (16):

$$Tafel\ slope = -\frac{(2.303)(8.314 J / mol.K)(298K)}{(0.5)(96486C / mol)}$$

$$= -0.118\ V / dec$$

$$= -118\ mV / dec$$

At 343K $= -135\ mV / dec$

2, Using Heyrovsky reaction as the RDS of the mechanism:

γ	ν	*r*	β
1	1	1	0.5

Insert the above values into equation (17), the cathodic transfer coefficient, α_c is calculated to be 1.5. Then insert this value into equation (16):

$$Tafel\ slope = -\frac{(2.303)(8.314 J / mol.K)(298K)}{(1.5)(96486C / mol)}$$

$$= -0.040\ V / dec$$

$$= -40\ mV / dec$$

$$At\ 343K \quad = -46\ mV / dec$$

3, Using Tafel reaction as the RDS of the mechanism:

γ	ν	r	β
2	1	0	0.5

Insert the above values into equation (17), the cathodic transfer coefficient, α_c is calculated to be 2. Then insert this value into equation (16):

$$Tafel\ slope = -\frac{(2.303)(8.314 J / mol.K)(298K)}{(2)(96486C / mol)}$$

$$= -0.030\ V / dec$$

$$= -30\ mV / dec$$

$$At\ 343K \quad = -35\ mV / dec$$

4. EXPERIMENTAL PROCEDURE

4.1 Equipment

A Teflon 250 mL cylindrical cell was used in the experiments. There were six openings at the cover of the cell which allowed sampling, inserting electrodes and releasing exhaust gases. A Mercury/Mercuric oxide electrode at 25°C was used as the reference electrode. It was placed in a 100 mL polypropylene centrifugal tube and connected to the cell by Teflon tubing. Both the tube and the Teflon tubing were filled with the same electrolyte as the cell. Nickel sheet or amorphous nickel alloy foil and platinum mesh were used as the working and the counter electrodes respectively. A schematic diagram of the experimental cell is shown in Figure 4.1.

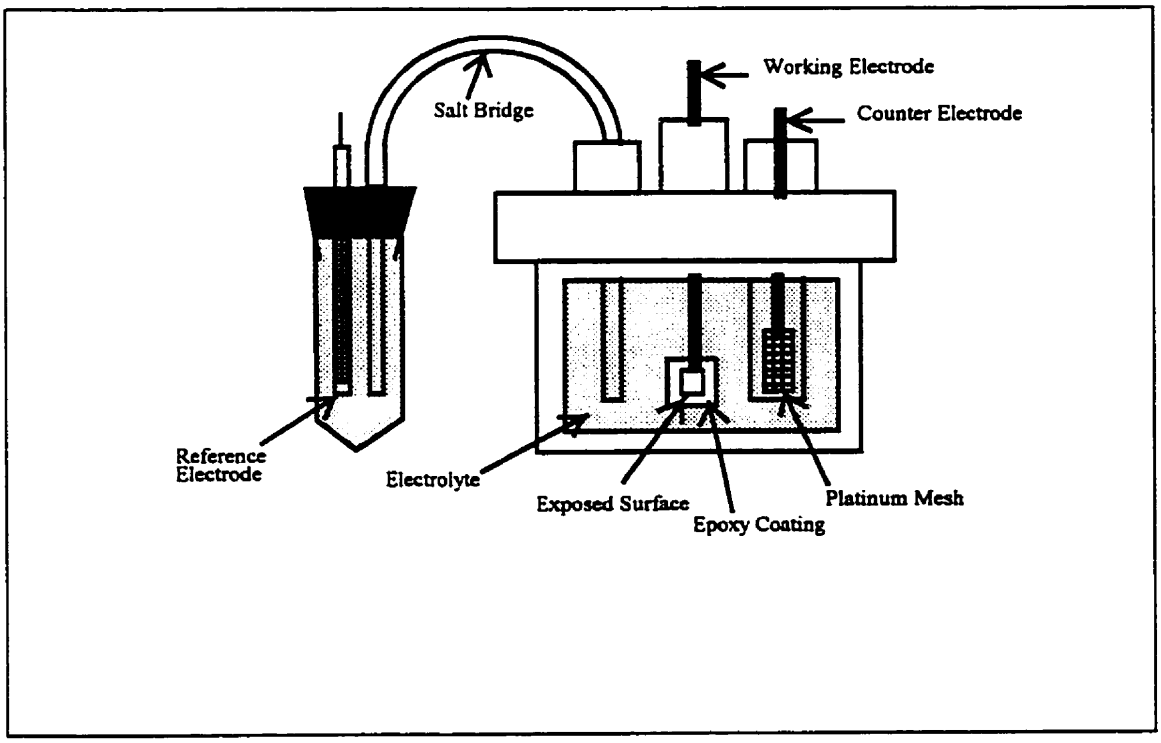

Figure 4.1 : Schematic Diagram of Electrochemical Cell

A complete electronic equipment setup diagram is show in Figure 4.2. All electrodes were connected to the Hokuto HA-501G GPIB potentiostat/galvanostat (Hokuto Denko Ltd.). The potentiostat was connected to the Hokuto HB-105 arbitrary function generator. Both the potentiostat and the function generator were controlled by a personal computer. Data recording was done using Hokuto data acquisition program installed in the computer. A water bath was used to maintain a constant cell temperature of 70 °C. A cold water condenser was used to condense water vapor in the exhaust gases outlet in order to minimize evaporative losses of electrolyte volume in the cell.

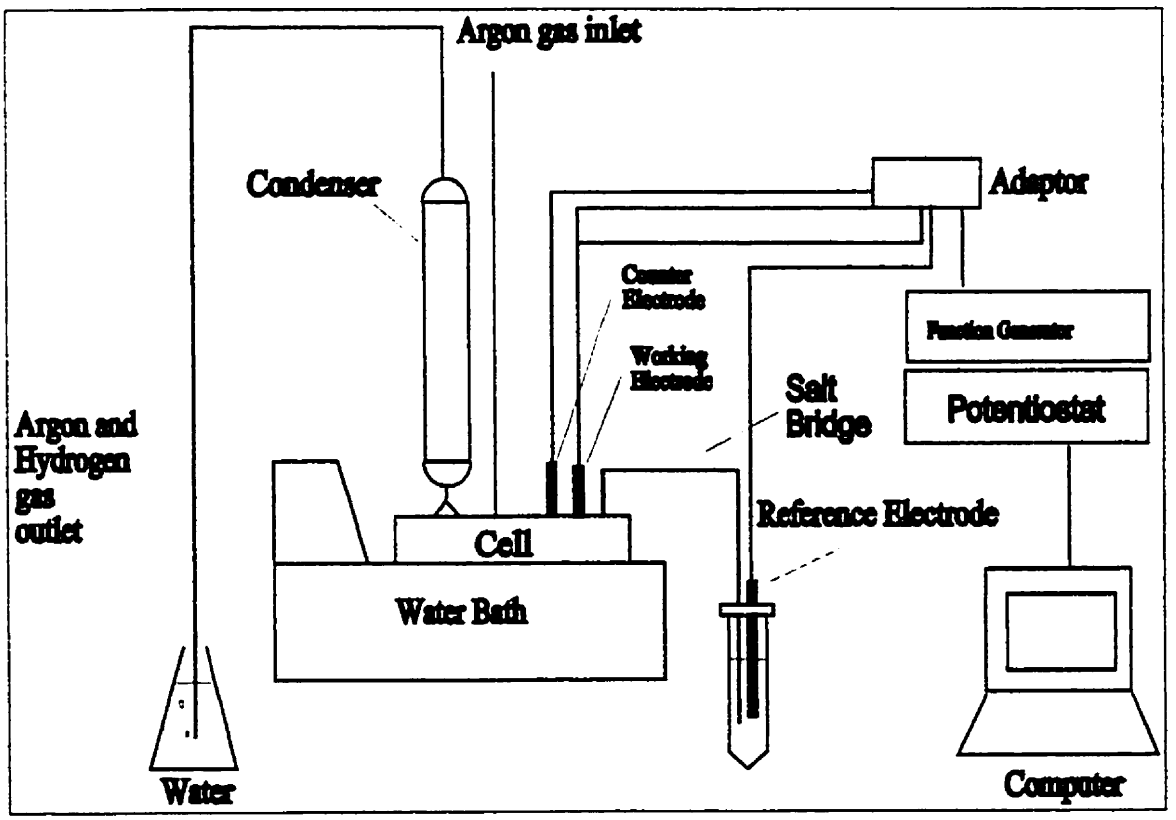

Figure 4.2 : Electronic Experimental Equipment Setup

4.2 Materials

The electrolyte used in the experiment was 8M potassium hydroxide solution. It was prepared by dissolving BDH analar grade, minimum assay 85.0% potassium hydroxide pellets in purified (Type I, 18 MΩ-cm) water produced by Millipore Milli-Q Water System. Vanadium solutions were made by dissolving vanadium (V) oxide (Assay 99.8%, Aesar Chemicals) in the 8M potassium hydroxide solution.

Argon gas was used to purge the electrolyte throughout the whole experiment to provide a low oxygen content environment in the cell.

The working electrodes were made using Nickel 200 or an amorphous nickel alloy ($Ni_{50}Co_{25}P_{15}B_{10}$) and were then soldered to a copper wire using solder wire (Kester, 3mm wire, 50Pb-50Sn). The nominal composition of Ni 200 is given in Table 5. Amercoat 90HS™ epoxy-phenolic coating was used to coat the electrodes and the soldered connection.

Table 5 : Nominal Composition of Commercial Ni 200 [38]

Element	Composition (wt %)
Ni	99.5
C	< 0.08
Mn	< 0.18
Fe	< 0.2
Cu	< 0.13
Si	< 0.18

4.3 Methods

4.3.1 Preparation of Nickel Electrodes

Nickel sheets of about 1 cm^2 were cut from a piece of Nickel 200 sheet using a shear cutter. One surface of the nickel plates was polished. First, the surface was ground using silicon carbide grit 600 paper (Leco GP-25 Grinder-Polisher, model 023-200). It was then polished using 6 micron followed by one micron diamond paste polishing paper. All nickel plates were washed with acetone, methanol and distilled water between each grinding and polishing procedure. After the final polish, the nickel surface was examined under a microscope for any unpolished areas and the polishing procedure was repeated if necessary. The perimeter of the polished surface was roughened with a grit 320 sand paper leaving a polished area of about 0.1 cm^2 in the middle of the nickel plates. The nickel plates were then attached to a copper wire by a soldered connection. Finally, Amercoat was painted on the roughened electrodes surface and covered the copper wire, the back and the perimeter of the electrodes. The coating procedure was repeated three times according to the manufacturer's instructions at 24 hours intervals to allow for curing. A window of about 0.1 cm^2 was left uncovered on the polished nickel surface. The exact area of the window for each electrode was imaged by a video camera (Olympus LZ-II Stereo Macrograph with Leco Video Camera XC-77) and determined by the IA-3001 Image Analysis Program from Leco Cooperation.

4.3.2 Preparation of Amorphous Nickel Alloy Electrodes

Amorphous nickel alloy ribbon of composition $Ni_{50}Co_{25}P_{15}B_{10}$ was used for the experiments. The ribbon was cut into small coupons with an area of about 1 cm^2. They

were then polished using 1 micron diamond paste. After that, each coupon would be spot welded on a Ni-200 coupon at two of the four corners. In this way, crystallization of the amorphous alloy ribbon would not occur. The nickel side of the combined coupons would then be soldered to the copper wire and coated with Amercoat using the same procedure as the preparation of Ni-200 electrodes. The electrode areas were then measured using the same image analysis equipment. The resistance between the electrodes ends (nickel end to wire end) were measured in order to check if there was a defect in the manufacturing process. The resistance measured should be between 0 and 0.1Ω.

4.3.3 Preparation of Potassium Hydroxide Electrolyte

The 8M potassium hydroxide (KOH) electrolyte was prepared by dissolving KOH pellets in Millipore purified water using a 1L polypropylene volummetric flask. Glass volummetric flasks were not used because the caustic would attack the glass and contaminate the solution. The electrolyte was then purified by pre-electrolysis for 48 hours up to a potential of -1900 mV versus Hg/HgO. Platinum was used as both the working and counter electrodes. They were cleaned in dilute nitric acid after 24 hours of pre-electrolysis and then continued for another 24 hours. The purified KOH was then stored in polypropylene bottles.

4.3.4 Experimental Procedure

Experiments were performed using Ni-200 electrodes as standard testing material which were used to compare with the nickel base amorphous alloy electrodes. After an appropriate amount of 8M KOH was measured and transferred to the Teflon cell, the cell

was connected to the condenser and put in the water bath at 70 ± 1°C. Argon gas flow at 90mL/min was started to purge the cell. After one hour of purging, the nickel working electrode was inserted in the cell and argon gas was continued purging for another hour. The reference electrode was put into the polypropylene centrifugal tube containing the electrolyte. The Teflon tubing connecting the reference electrode tube and the cell was then filled with the electrolyte using a syringe. All electrodes were connected to the potentiostat. Cathodic cleaning of the nickel electrode surface would begin after two hours of argon gas purging. A potential of -1350 mV was applied to the nickel electrode for 3 hours for cathodic cleaning. After that, the rest potential of the electrode would be monitored for half an hour. Chronopotentiometry was then begun. A constant current was applied to the working electrode and the potential was monitored as a function of time. The current was set to give a current density of 250 mA/cm^2 for all experiments. A personal computer was used to monitor the potential and record data every five minutes for a period of 48 hours. A slight modification of the data compiling program was needed and was shown in Appendix F. When the potential became steady, a specific amount of vanadium was injected into the cell using a syringe. The vanadium solution was prepared by dissolving vanadium pentoxide powder, V_2O_5, into the pre-electrolyzed KOH. After that, the experiment would be continued until another steady potential was reached. The concentration of the vanadium in the electrolyte was varied in different experiments in order to obtain the concentration effect of the vanadium addition (0.1, 10, 50, 100, 500 and 1000ppm). A sample of the electrolyte, about 1 mL, would be obtained after the vanadium addition of the experiment so as to confirm the vanadium concentration in the electrolyte during the experiment using NAA. After each experiment, the cell was washed

first with soap and then with nitric acid for 12 hours, then washed with purified water for 2 minutes. Finally, potassium hydroxide solution was used to rinse the cell before the next experiment.

4.3.5 Tafel Measurements

Steady state potentiostatic measurements using a potential step method was applied to the working electrode and the current response was recorded. The working electrodes were cleaned cathodically at -1350 mV versus Hg/HgO for 3 hours to remove any reducible surface oxides before the Tafel measurement. The potential range of the scan was between -1000 mV to -1700 mV versus Hg/HgO. In order to obtain the steady current readings, the potential at each data point of the Tafel plot was held for 10 hours before stepping to another potential. After the first Tafel measurement, vanadium was added to the electrolyte and a constant current was applied to the electrode following the same procedure as chronopotentiometry experiments. After 20 hours of chronopotentiometry, a second Tafel measurement would be performed. Since the time required for stabilization after vanadium was added to the electrolyte was much shorter, the time between two potential steps was set to be 30 minutes. The Tafel measurement was performed once for Ni-200 and amorphous nickel alloy. The Tafel data was plotted as log of current density versus cathodic overpotential. The Tafel slope (b) was calculated from this plot and used to determine if there was any change in reaction mechanism pre and post catalyst addition.

4.3.6 Analytical Methods

The vanadium concentration in the electrolyte was analysed by Neutron Activation Analysis provided by the SLOWPOKE reactor located in the Haultain Building, University of Toronto. The samples were irradiated at 2 kW for 1 minute and then measured the radiation for 100 seconds. The data was converted to vanadium concentrations using the difference of the peak count area from the background counts and comparing with a calibration count.

After the experiments, the nickel electrode surface was analyzed by Hitachi S-2500 scanning electron microscope (SEM). SEM photos of different magnifications were taken. In addition, the electrode surface was also analyzed using energy dispersive x-ray analysis (EDX) included in the same microscope. The EDX spectrum was used to identify the elements present on the nickel electrode surface. The working parameters of the SEM are given in Table 6.

Table 6 : SEM and EDX Settings

Applications	**Settings**
Accelerating Voltage	20 keV
Emission Beam Current	100 μA
Tilt Angle	15 degree
Working distance SEM EDX	 15 mm 30-35 mm

Some of the electrode surfaces were analyzed using x-ray photoelectron spectroscopy (XPS) and x-ray diffraction. The Leybold Max 200 X-ray Photoelectron Spectrometer was located in the Centre for Biomaterials in the Mining Building at the University of Toronto. The machine was calibrated using Ag $3d_{5/2}$ and Cu $2P_{3/2}$ binding energy peaks at 368.3 and 932.7 eV respectively. The resulting spectra were calibrated using C 1s peak at 284.6 eV before fitting. A dual anode X-ray source produced an unmonochromatized Mg-Kα radiation (1253.6 eV) which operated at 15 kV and a 20 mA emission current. Low resolution scans (survey, pass energy = 192 eV) were used to determine the components in the surface film and high resolution scans (pass energy = 48eV) were used to determine the oxidation states of the species in the surface film..

The XRD analysis was performed using Siemens D5000 θ/2θ Diffractometer with Cu-Kα source operating at 50 kV, 35 mA. The secondary beam was monochromatized by a Kevex solid state detector. Data were processed by Diffrac AT™ software.

4.4 Safety

Care was taken handling concentrated potassium hydroxide solutions. Gloves and laboratory coat were worn during the preparation of the KOH solution and at any time when contact with the solutions was possible. Waste bottles were set up for waste vanadium solution storage before carrying out suitable chemical disposal procedures. Since hydrogen was produced during the experiments, there was a potential fire hazard. In the experimental setup, the exhaust gas was passed into a water trap to prevent sparks or fire from igniting the hydrogen present in the cell.

The Amercoat for electrode coating contains volatile organic solvents, xylene and ethyl benzene, which are hazardous. The coating procedure was done inside a fumehood and the coated electrodes were also kept in the fumehood until fully cured.

5. RESULTS

This section consists of three mains sections. The first section will present the results from experiments using Ni-200 electrodes. This includes chronopotentiometry from different catalyst concentrations, steady state potentiostatic polarization (Tafel plots), before and after catalyst addition, the effect of the method of catalyst addition and the effect of electrolyte impurities.

Results of chronopotentiometry from different catalyst concentrations will be presented followed by their corresponding SEM and EDX spectra. The range of concentrations of catalyst additions include 10, 50, 100 and 500 ppm. Results of more extreme catalyst concentrations, 0.1 and 1000 ppm, will be presented and compared with the results of the other catalyst concentrations additions. The results of XPS and XRD on catalyst coated electrode surface will be presented at the end.

The second section will present the results from experiments using a Ni-base amorphous alloy. These will be used to compared with the Ni-200 results. The range of concentrations of catalyst additions include 50, 100 and 500 ppm. Results of steady state potentiostatic polarization and surface analysis using XRD will also be presented.

The third section will compare the results of Ni-200 and Ni-base amorphous alloy. This include chronopotentiometry, Tafel results and morphology of the coatings.

5.1 Ni-200

5.1.1 Ni-200

The results obtained for Ni-200 samples will be presented in this section. Fig. 5.1.1 shows the chronopotentiogram of nickel before catalyst addition plotted as the average of 5 tests. The final potential was about -1920mV. Fig. 5.1.2 shows the SEM micrograph for polished Ni-200 sample and Fig. 5.1.3 shows the corresponding EDX spectrum for this sample. The smooth featureless surface shown in Fig. 5.1.2 serves as a standard to compare with the coated nickel electrode surfaces in the later sections. The corresponding EDX spectrum shows only nickel peaks on the nickel electrode.

Fig. 5.1.1 : Chronopotentiometry of Ni-200 in 8M KOH at 70°C

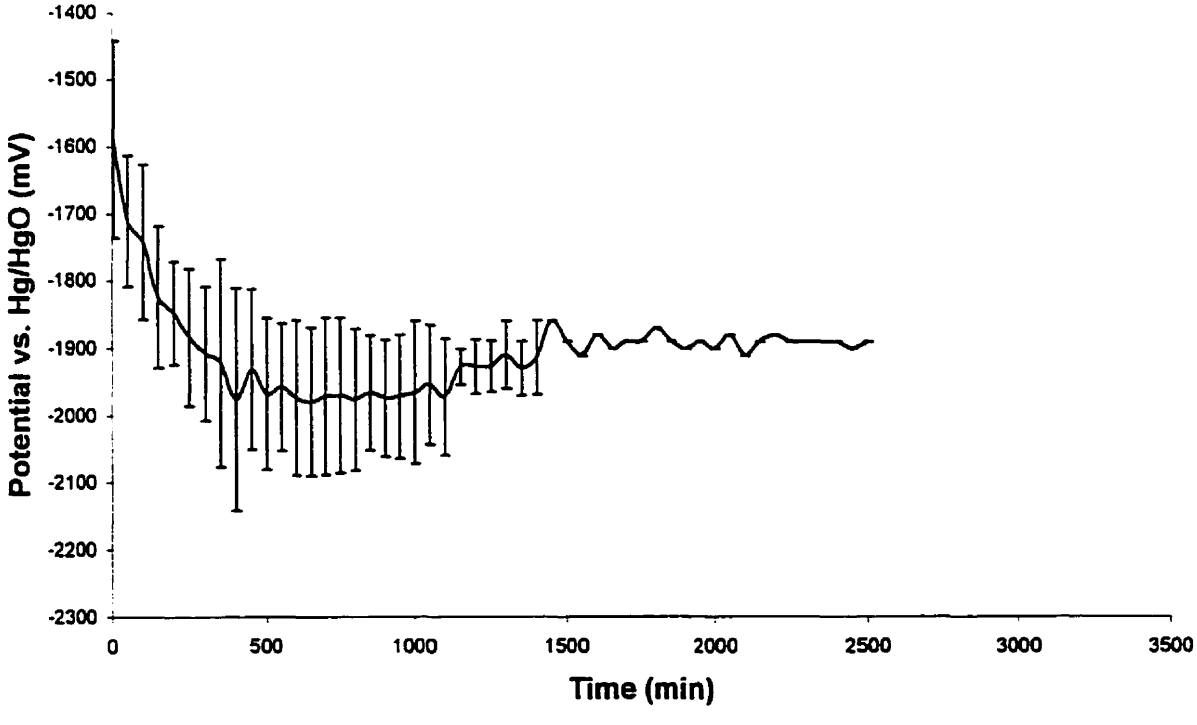

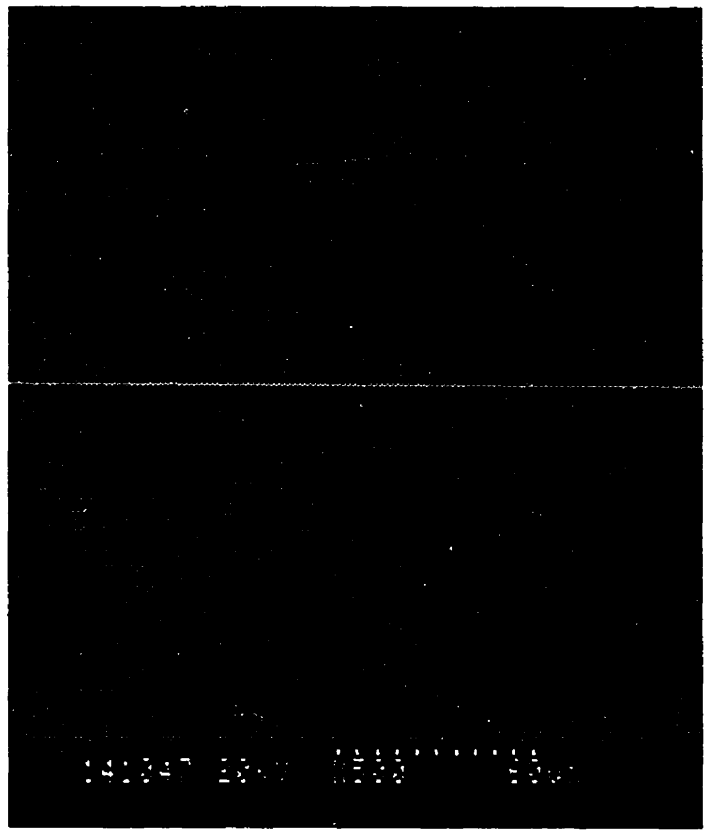

Fig. 5.1.2 SEM micrograph showing as-polished Ni-200 sample.

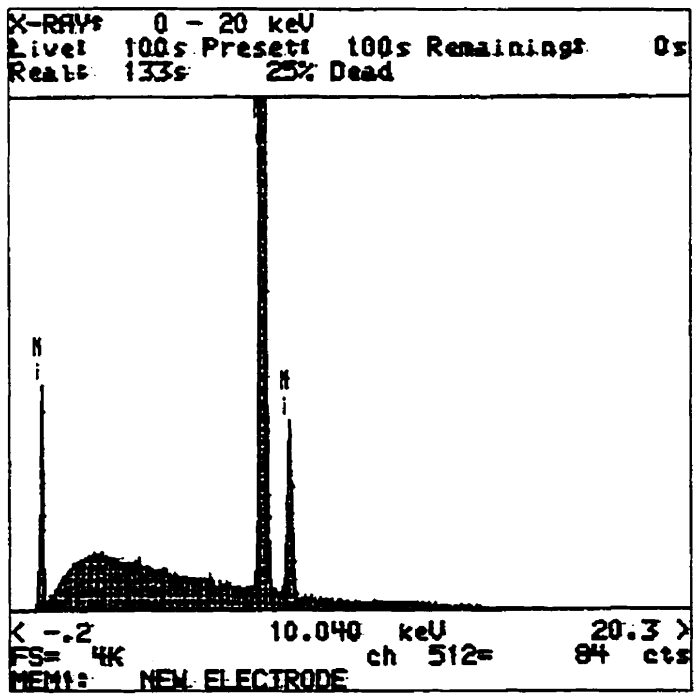

Fig. 5.1.3 EDX spectrum of as-polished Ni-200 sample.

Sections 5.1.2 to 5.1.7 shows the chronopotentiometry results of the catalyst coated electrode with their SEM and EDX spectra. Section 5.1.8 shows the Tafel behaviour of the Ni-200 before and after catalyst addition. Catalyst concentrations ranged from 10 to 1000 ppm.

5.1.2 Ni-200 with 10 ppm Catalyst Addition

The results obtained for a Ni-200 sample with 10 ppm catalyst addition will be presented in this section. Fig. 5.1.4 shows the chronopotentiograms for three identical separate tests. Deactivation was observed with the onset of polarization and the reactivation after the addition of the catalyst. The final potential after the addition of catalyst was about -1800mV for all three tests.

Fig. 5.1.5 shows the SEM micrograph for the electrode after 10 ppm catalyst addition and Fig. 5.1.6 shows the corresponding EDX spectrum for this sample. The SEM shows a coated surface with cracks and it contains potassium, vanadium, zinc and iron as shown in the EDX spectrum.

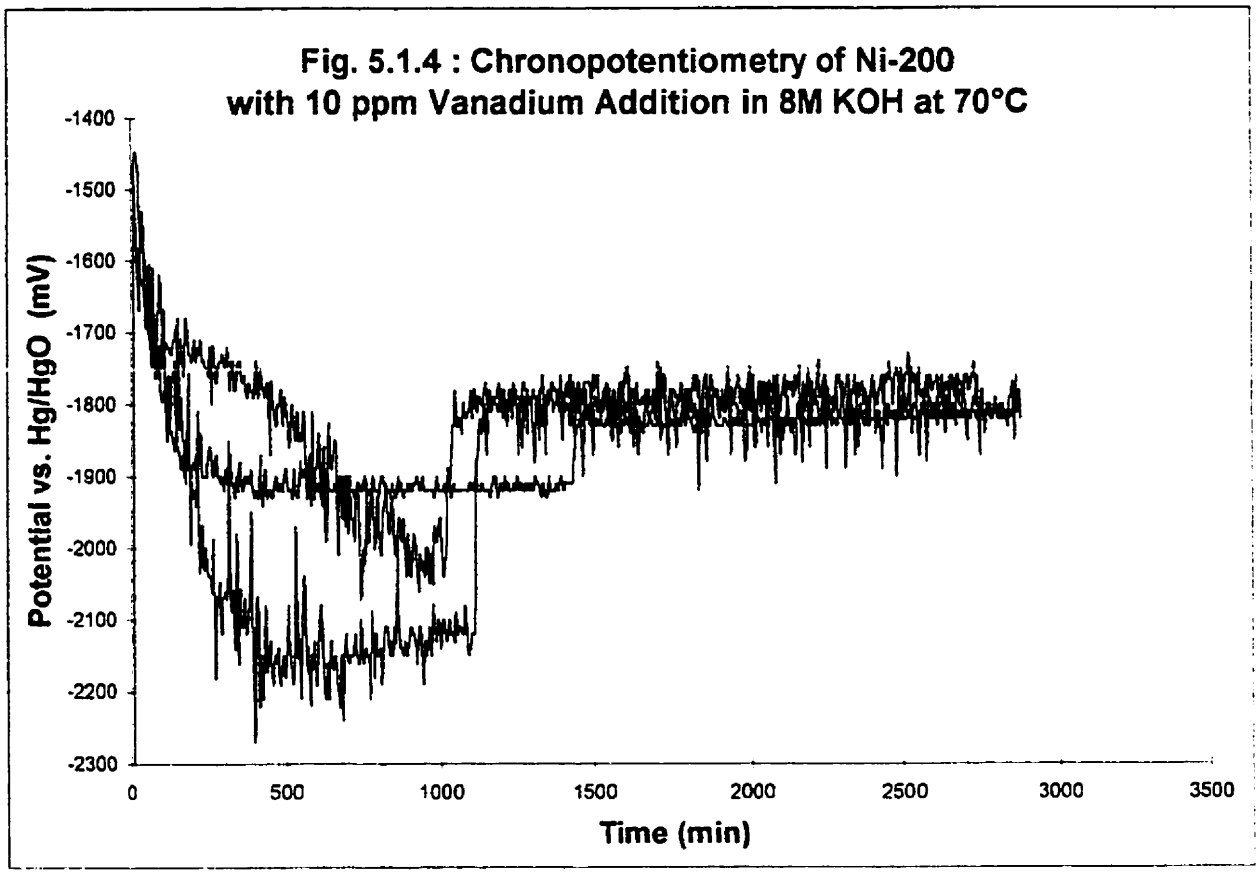
Fig. 5.1.4 : Chronopotentiometry of Ni-200
with 10 ppm Vanadium Addition in 8M KOH at 70°C
Potential vs. Hg/HgO (mV)
-1400
-1500
-1600
-1700
-1800
-1900
-2000
-2100
-2200
-2300
0
500
1000
1500
2000
2500
3000
3500
Time (min)

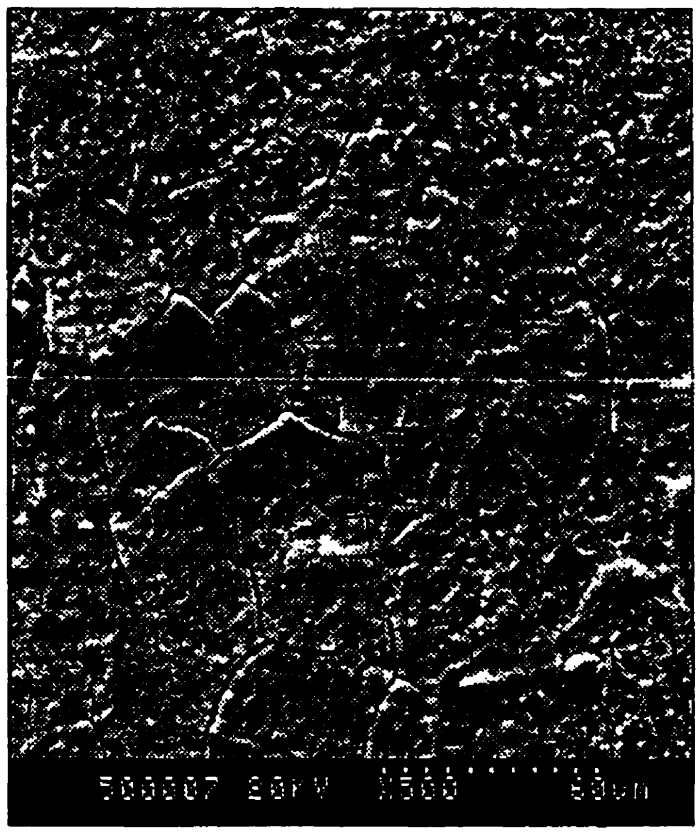

Fig. 5.1.5 SEM micrograph showing electrode surface after 10 ppm catalyst addition.

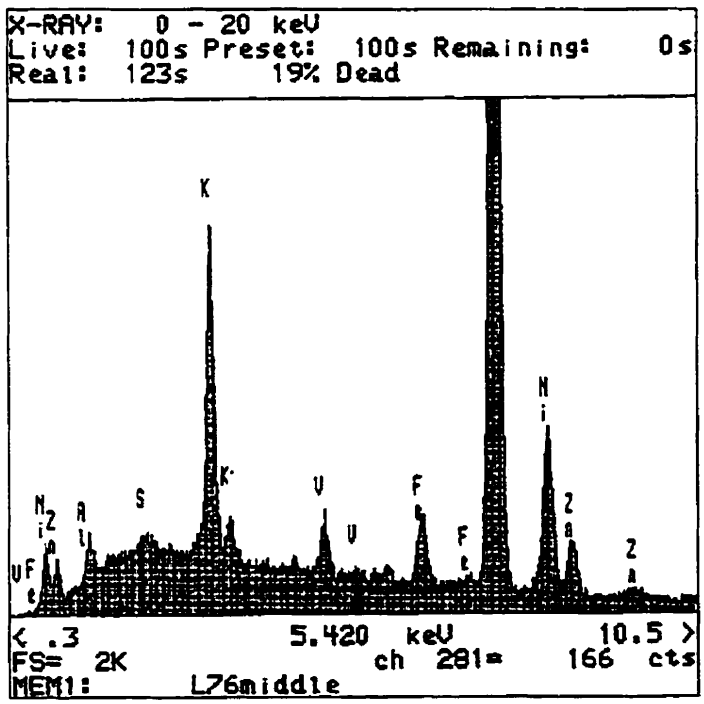

Fig. 5.1.6 EDX spectrum of electrode surface after 10 ppm catalyst addition.

5.1.3 Ni-200 with 50 ppm Catalyst Addition

The results obtained for a Ni-200 sample with 50 ppm catalyst addition will be presented in this section. Fig. 5.1.7 shows the chronopotentiograms for three identical separate tests. The final potential after the addition of catalyst was about -1800mV for all three tests.

Fig. 5.1.8 shows the SEM micrograph for the electrode after 50 ppm catalyst addition and Fig. 5.1.9 shows the corresponding EDX spectrum for this sample. SEM photo shows a few cracked patches form on top of the rough coated surface and the vanadium content is much higher than the coating of the 10ppm catalyst addition.

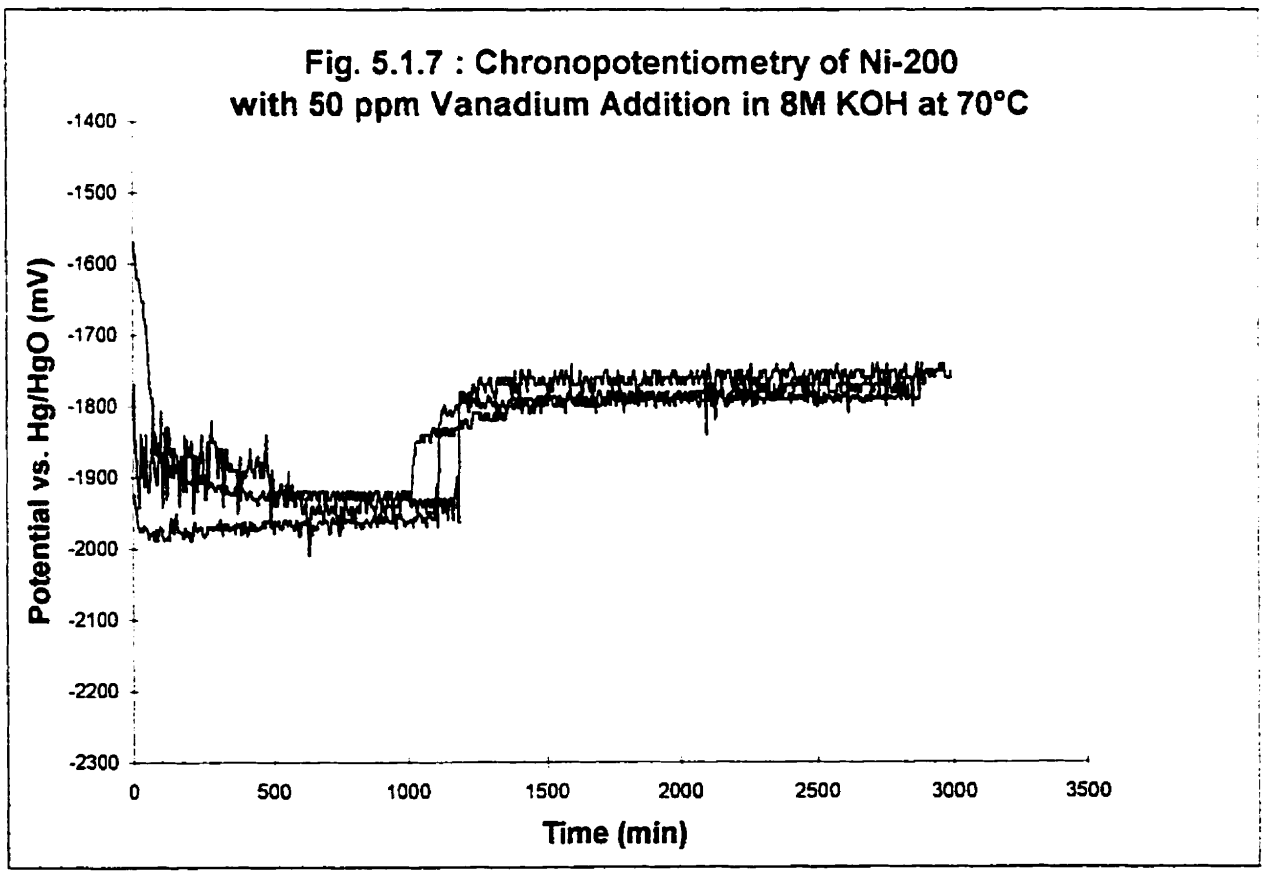

Fig. 5.1.8 SEM micrograph showing electrode surface after 50 ppm catalyst addition.

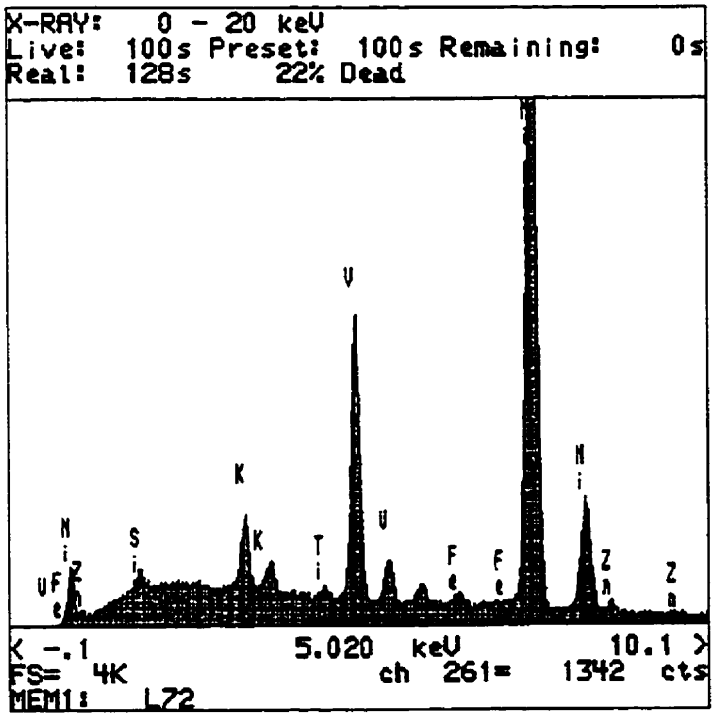

Fig. 5.1.9 EDX spectrum of electrode surface after 50 ppm catalyst addition.

5.1.4 Ni-200 with 100 ppm Catalyst Addition

The results obtained for an Ni-200 sample with 100 ppm catalyst addition will be presented in this section. Fig. 5.1.10 shows the chronopotentiograms for three separate tests. The final potential after the addition of catalyst was about -1800mV for all three tests.

Fig. 5.1.11 shows the SEM micrograph for the electrode after 100 ppm catalyst addition and Fig. 5.1.12 shows the corresponding EDX spectrum for this sample. The SEM shows very large catalyst addition causes rough patches of coating to form on top of the surface compared to the 50ppm addition. Vanadium is the major specie in the coating as it has the largest peak in the EDX spectrum.

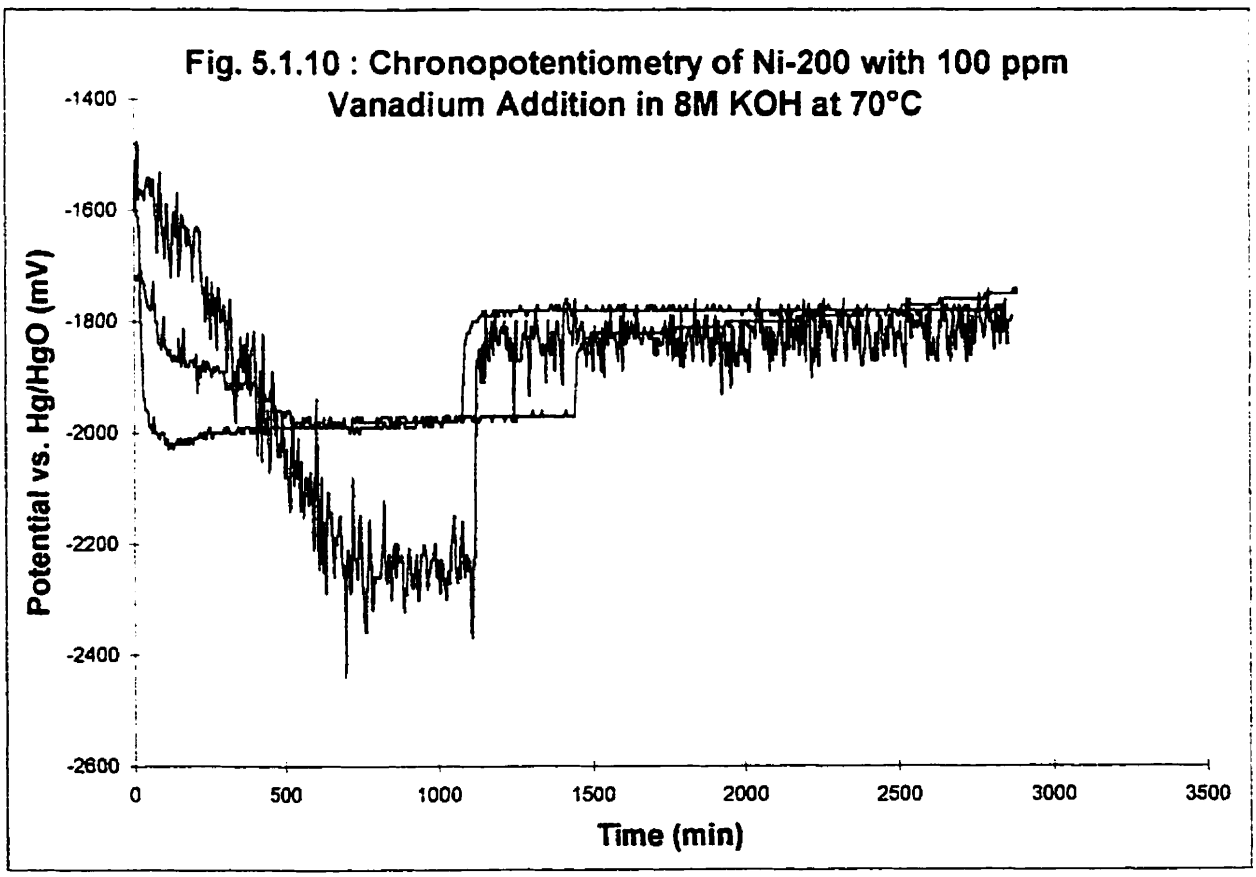

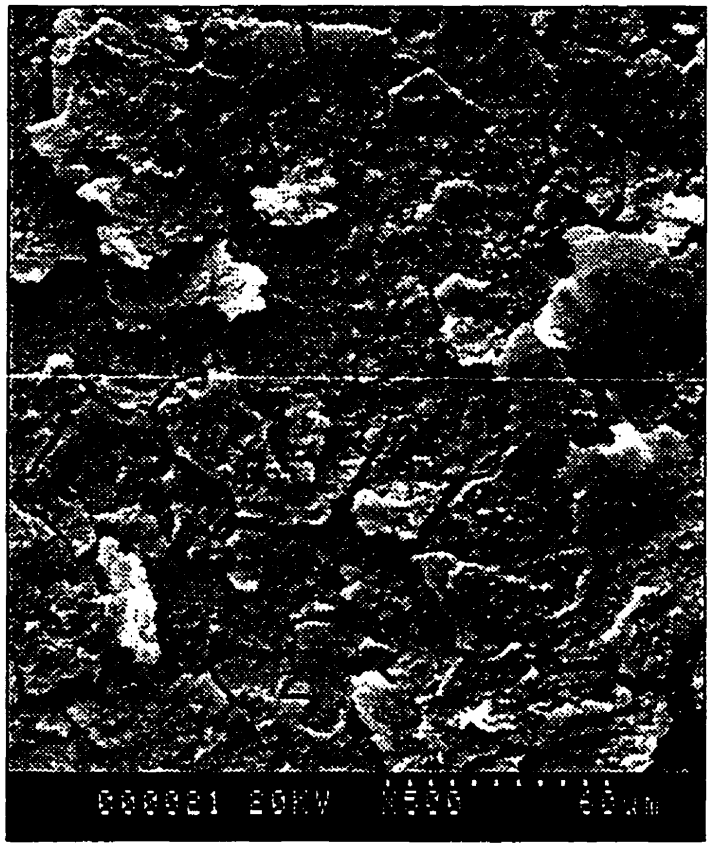

Fig. 5.1.11 SEM micrograph showing electrode surface after 100 ppm catalyst addition.

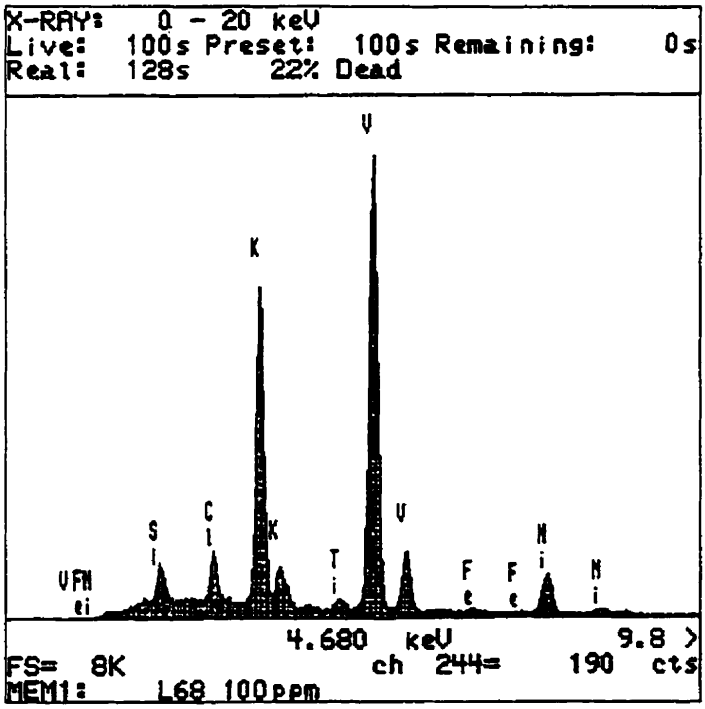

Fig. 5.1.12 EDX spectrum of electrode surface after 100 ppm catalyst addition.

5.1.5 Ni-200 with 500 ppm Catalyst Addition

The results obtained for a Ni-200 sample with 500 ppm catalyst addition will be presented in this section. Fig. 5.1.13 shows the chronopotentiograms for three separate tests. The final potential after the addition of catalyst was about -1800mV for all three tests.

Fig. 5.1.14 shows the SEM micrograph for the electrode after 500 ppm catalyst addition and Fig. 5.1.15 shows the corresponding EDX spectrum for this sample. The SEM photo shows thick cracked coating surface of the electrode. Vanadium to nickel peak ratios are larger in the EDX spectrum for the coating compares to the EDX spectrum for 100ppm addition. No Fe is detected in the coating.

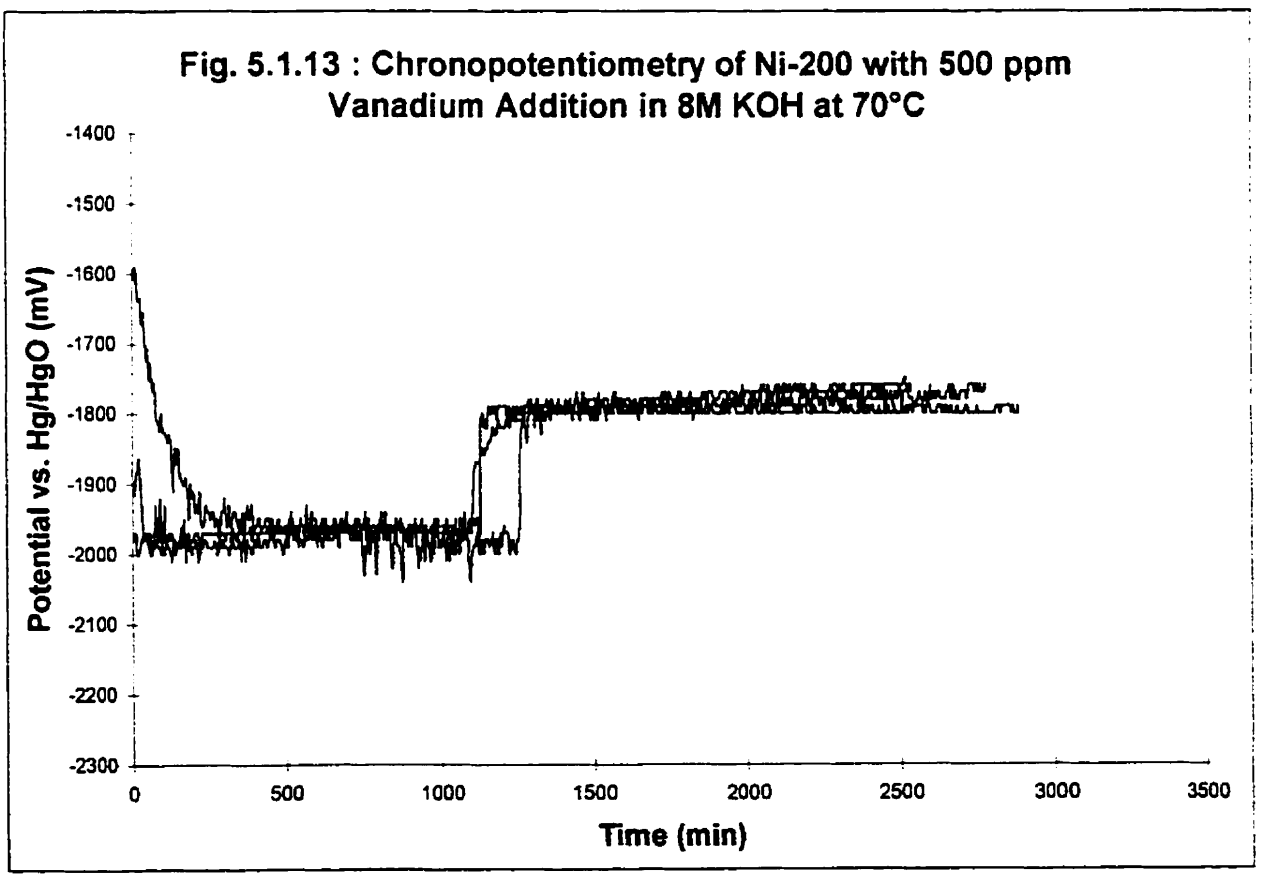

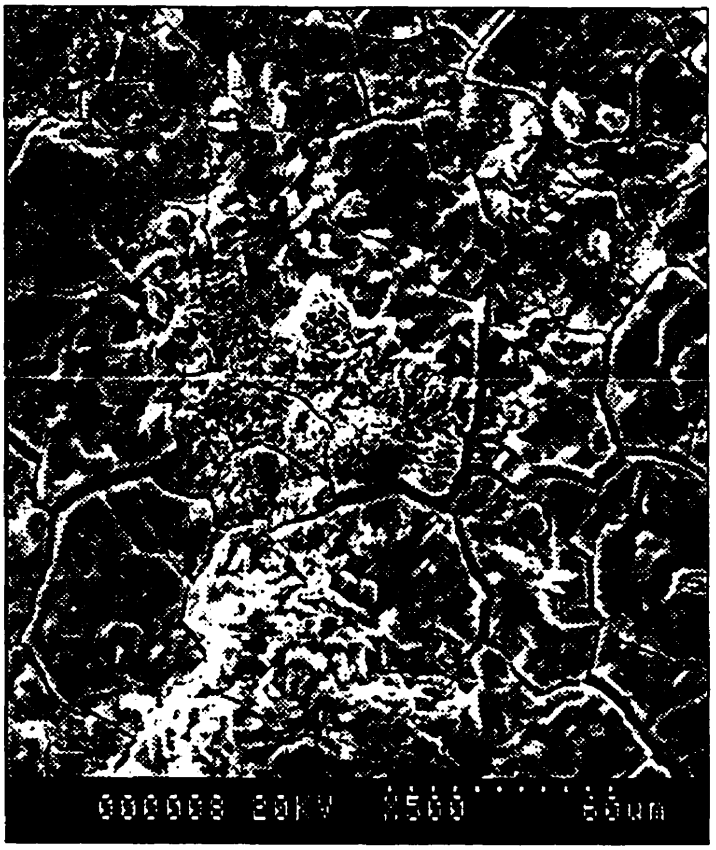

Fig. 5.1.14 SEM micrograph showing electrode surface after 500 ppm catalyst addition.

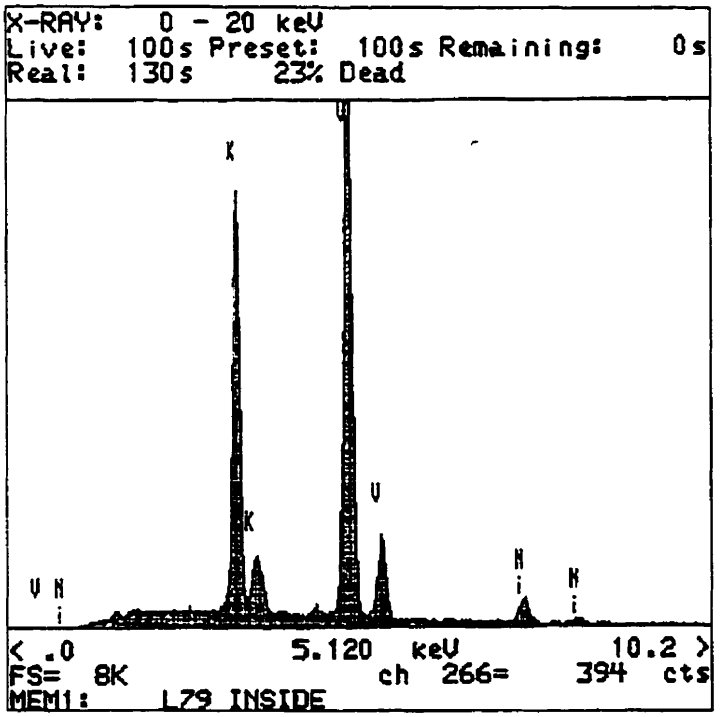

Fig. 5.1.15 EDX spectrum of electrode surface after 500 ppm catalyst addition.

5.1.6 Ni-200 with 0.1 and 1000 ppm Catalyst Addition

The results obtained for a Ni-200 sample with 0.1 and 1000 ppm catalyst addition will be presented in this section. These tests were done in order to study the potential behaviour at more extreme catalyst concentrations. Only one test was perform at each catalyst concentration. Fig. 5.1.16 and Fig. 5.1.17 show the chronopotentiograms for Ni-200 with 0.1 ppm and 1000 ppm catalyst addition respectively. As with other catalyst concentrations, the final potential after the 1000ppm catalyst addition was about -1800mV. For 0.1ppm, the final potential after catalyst addition was about -1830mV.

Fig. 5.1.18 shows the SEM micrograph for the electrode after 0.1 ppm catalyst addition and Fig. 5.1.19 shows the corresponding EDX spectrum for this sample. Small crystal plates were found on the electrode surface while the EDX spectrum identified them to be Fe crystals. The crystals were concentrated around a metal defect.

Fig. 5.1.20 shows the SEM micrograph for the electrode after 1000 ppm catalyst addition and Fig. 5.1.21 shows the corresponding EDX spectrum for this sample. The SEM photo shows a multi-layer coating was formed with cracks all over the coating. As with other catalyst concentrations coating, vanadium was the major component of the coating as shown in the corresponding EDX spectrum.

Fig. 5.1.16 : Chronopotentiometry of Ni-200 with 0.1ppm Vanadium Addition in 8M KOH at 70°C

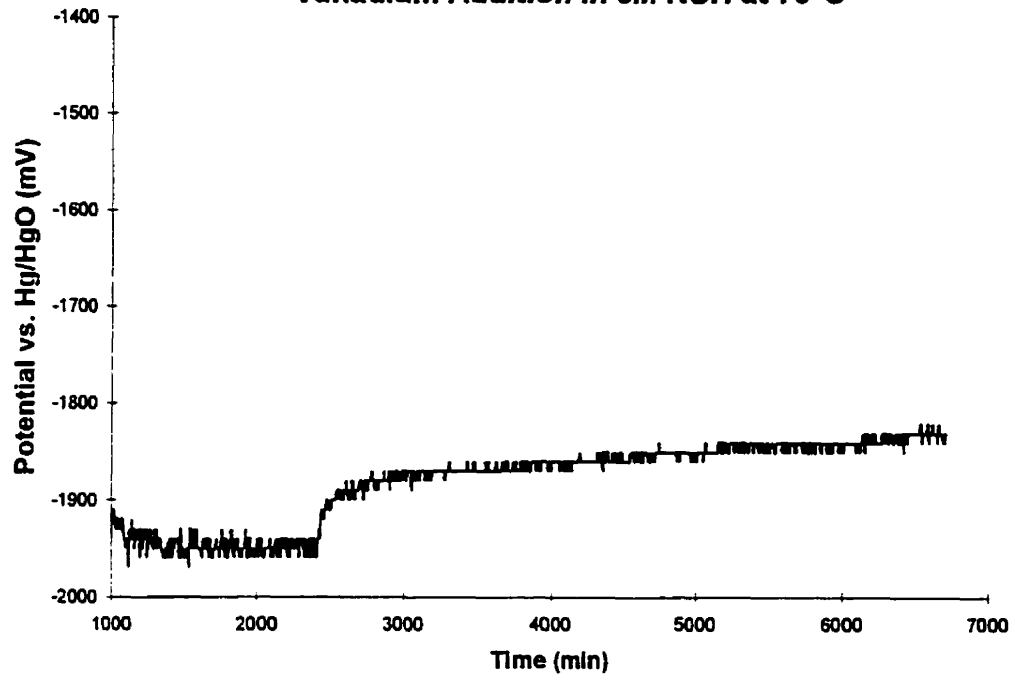

Fig. 5.1.17 : Chronopotentiometry of Ni-200 with 1000ppm Vanadium Addition in 8M KOH at 70°C

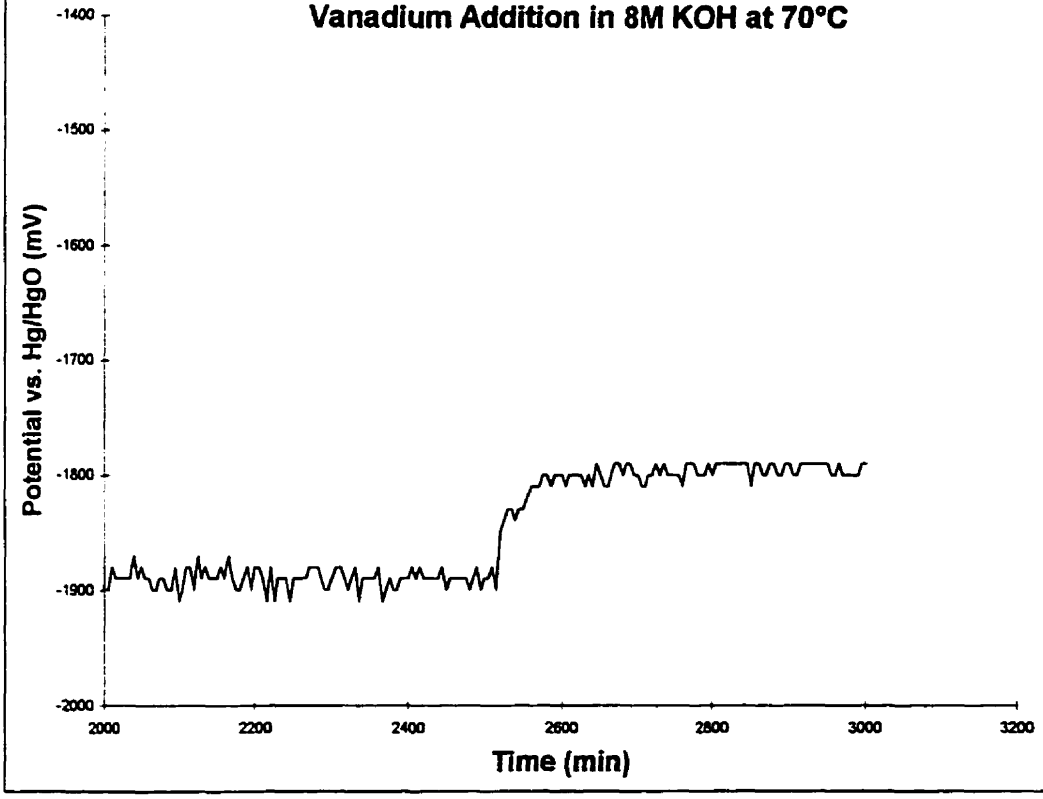

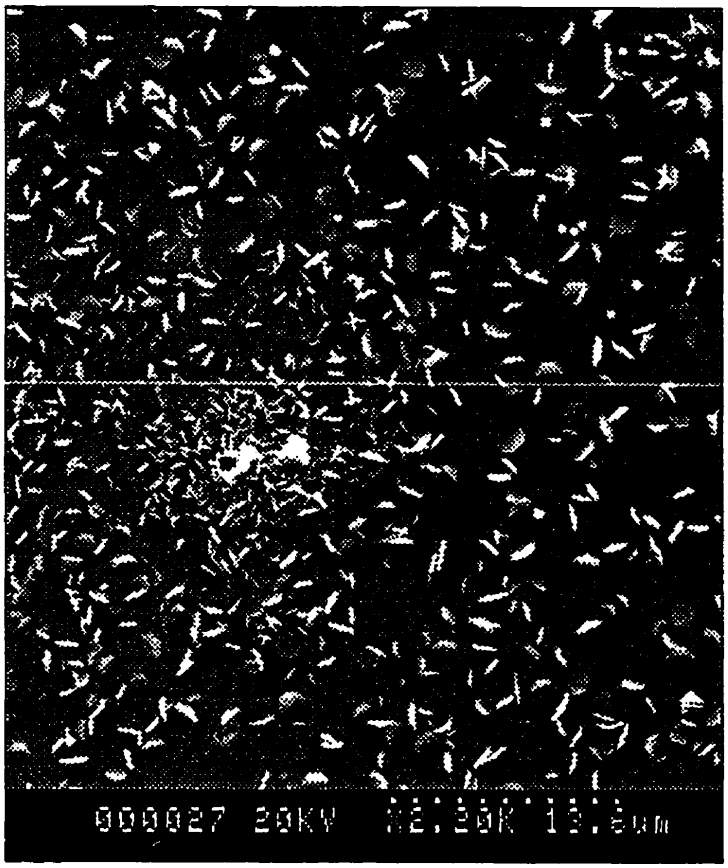

Fig. 5.1.18 SEM micrograph showing the electrode surface after 0.1 ppm catalyst addition.

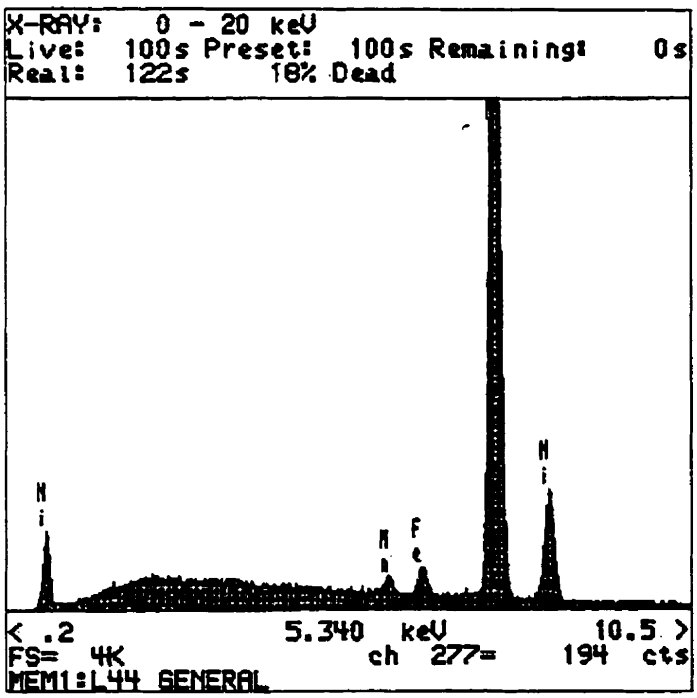

Fig. 5.1.19 EDX spectrum of the electrode surface after 0.1 ppm catalyst addition.

Fig. 5.1.20 SEM micrograph showing the electrode surface after 1000 ppm catalyst addition.

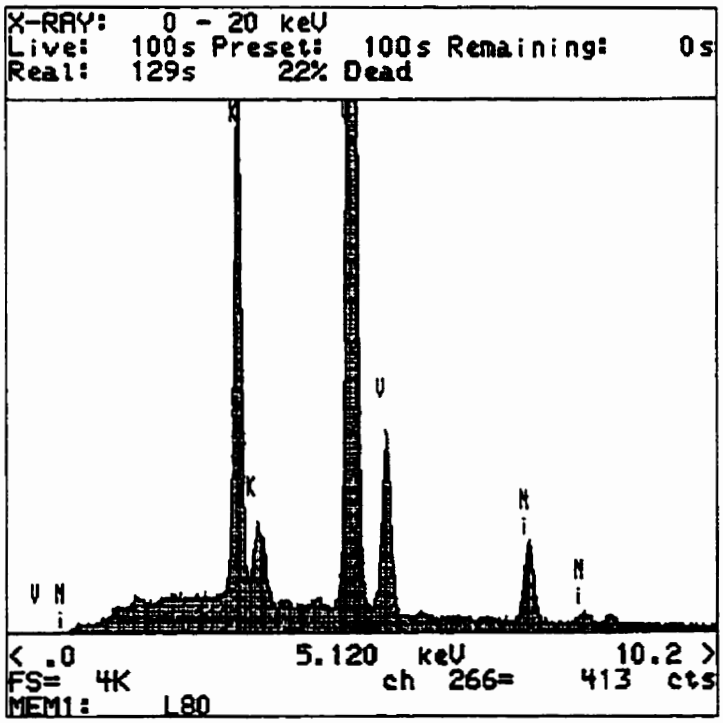

Fig. 5.1.21 EDX spectrum of the electrode surface after 1000 ppm catalyst addition.

5.1.7 Effect of Catalyst Concentration

This section will summarize the effect of different catalyst concentrations additions to the Ni-200 electrode potential. Fig. 5.1.22 shows the potential versus catalyst concentration plot. For vanadium concentrations higher than 10ppm, the change of the electrode potential was not dependent on the vanadium concentration in the electrolyte. Fig. 5.1.23 shows the SEM images of the electrode surface after different vanadium concentration additions. Except for 0.1ppm, all electrodes were fully coated and the coating became thicker at higher vanadium concentrations.

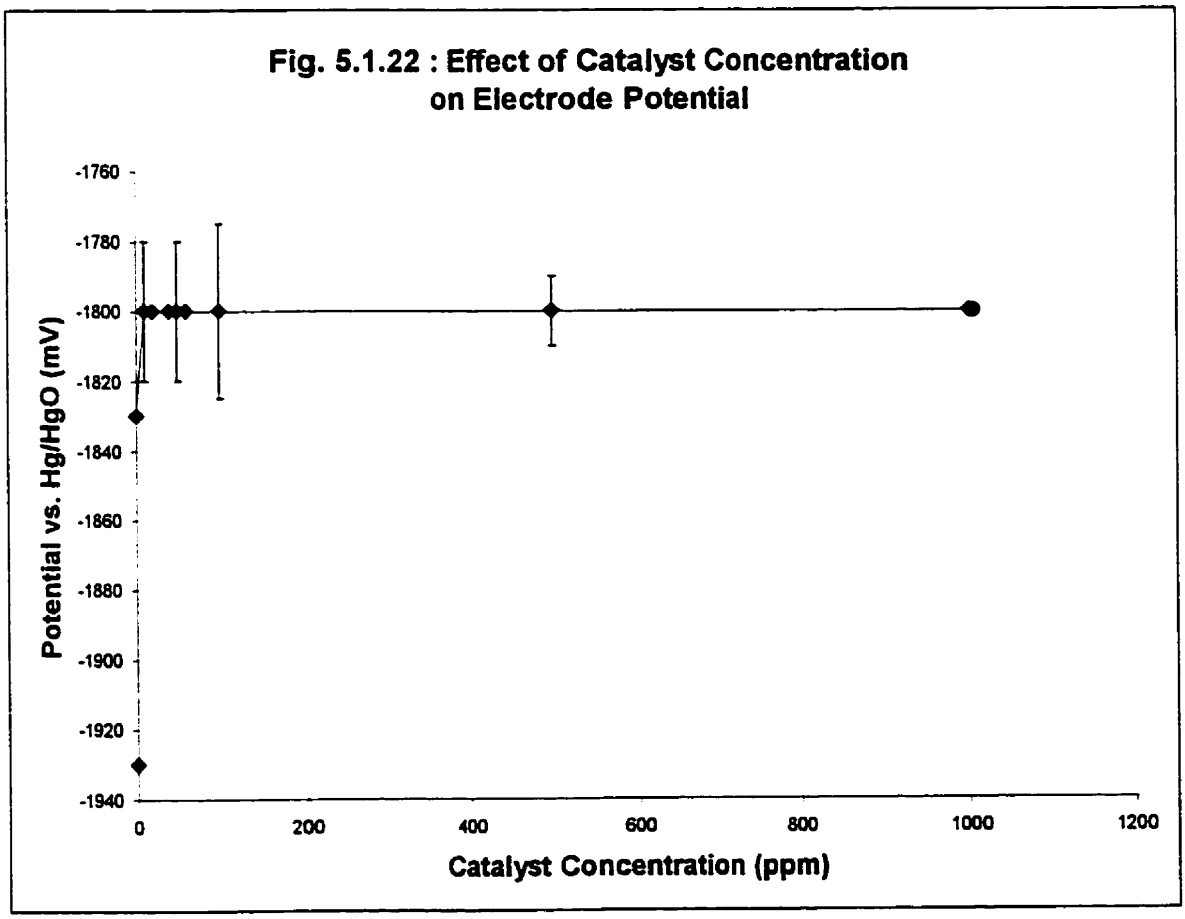

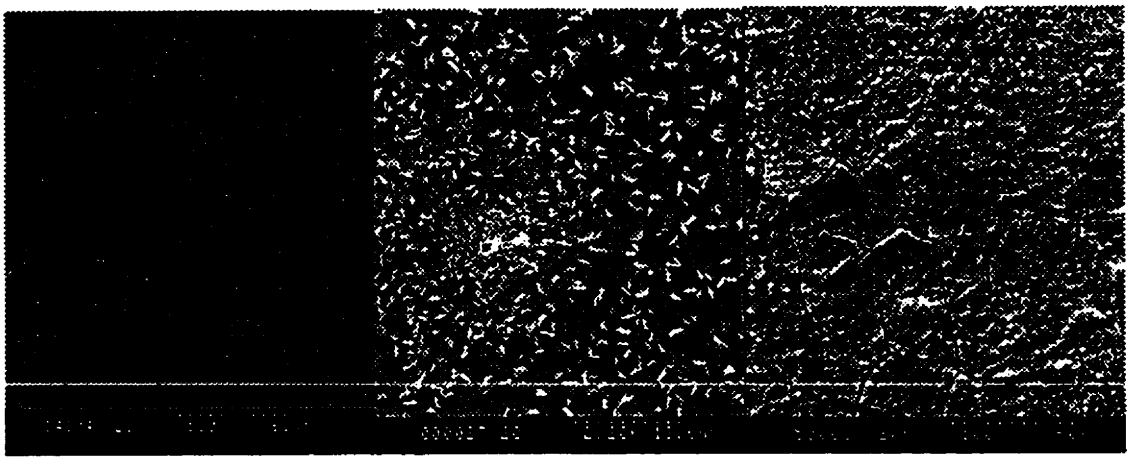

Ni-200 0.1ppm 10ppm

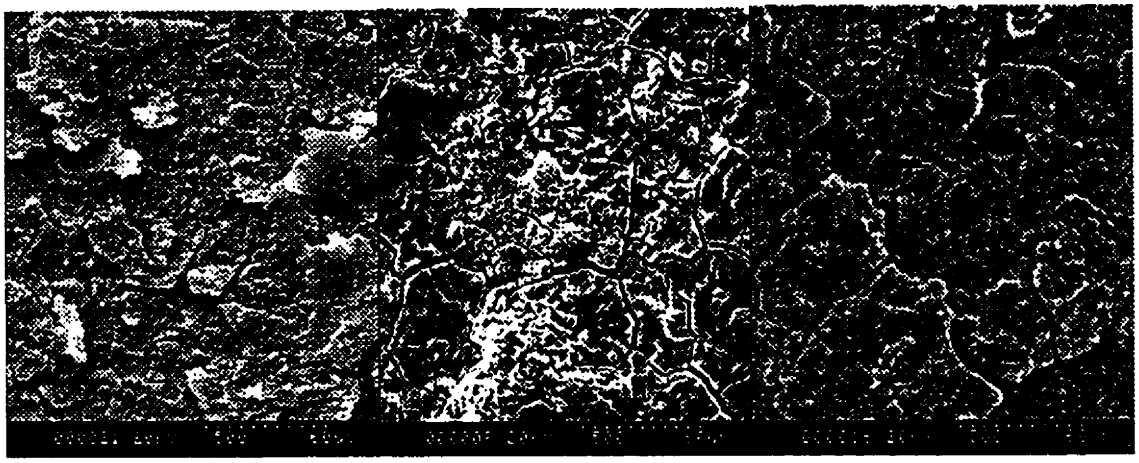

100ppm 500ppm 1000ppm

Fig. 5.1.23 : SEM images of electrode surface with different vanadium concentration additions (Ni-200).

5.1.8 Tafel Test for Ni-200 and Ni-200 with 100 ppm Catalyst Addition

Fig. 5.1.24 and Fig. 5.1.25 show the Tafel tests for the Ni-200 sample before and after 100 ppm catalyst addition respectively.

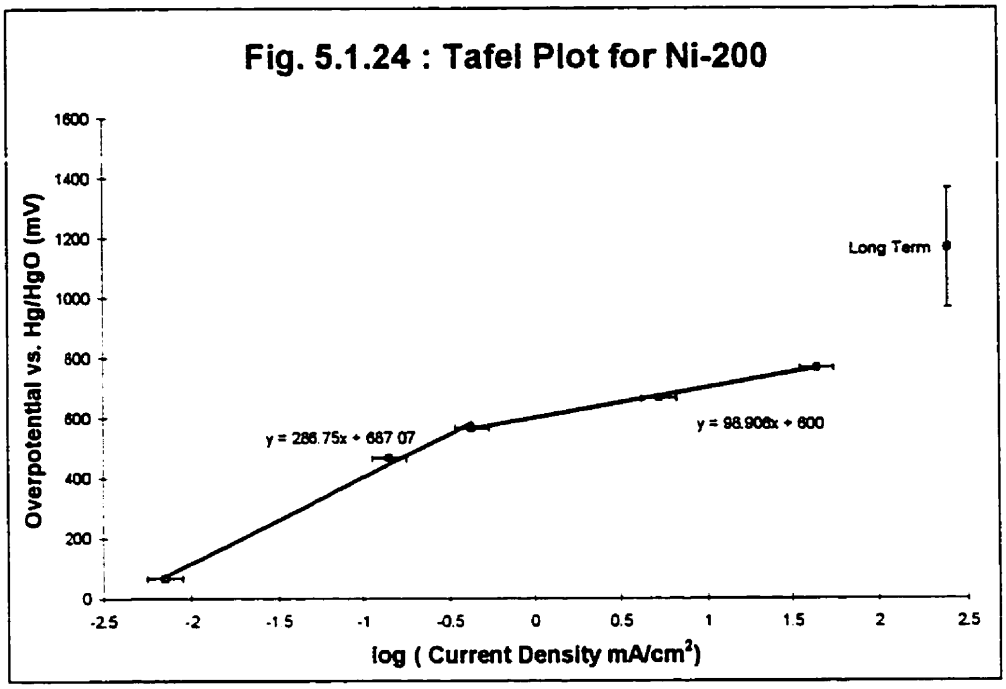

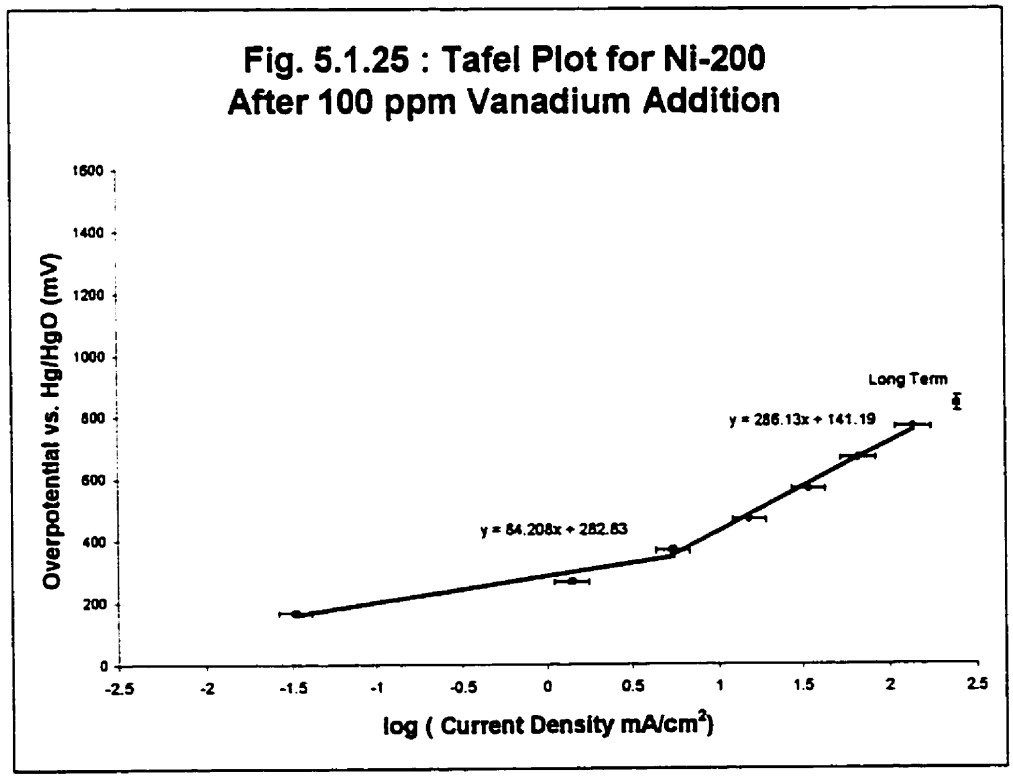

The error bars of the Tafel measurements represented the noise level of the current densities of an experiment. A long term point from the chronopotentiometry measurement was included in the figures which showed the vanadium coated electrode had Tafel data closer to steady state value.

5.1.9 Effect of Method of Catalyst Addition

This section will include the results of the single and multiple catalyst addition tests which would indicate whether the electrode potential and the morphology of the coating was affected by different addition procedures. In multiple addition tests, 2 additions of 10 ppm followed by 2 additions of 20 ppm and one 40 ppm were made in order to obtain a final concentration of 100 ppm. All additions were made when a steady potential was reached (~500 to 1000 min after the previous addition). Fig. 5.1.26 shows the chronopotentiograms of both single and multiple additions of 100 ppm catalyst addition. Both final potentials after catalyst additions were about -1790mV. For multiple additions, the potential became steady after the first 10ppm additon and no change in potential was observed upon subsequence additions.

Fig. 5.1.27 shows the SEM micrograph and corresponding EDX spectrum of electrode surface after a single and multiple catalyst additions. The surface with multiple additions had more cracks in the coating than the single addition one. Both EDX spectrum shows vanadium is the major component of the coating. However, the Ni to vanadium peak ratio is much smaller for the single addition than that of the multiple addition.

Fig. 5.1.26 : Chronopotentiometry of Ni-200 with Single and Multiple Vanadium Additions

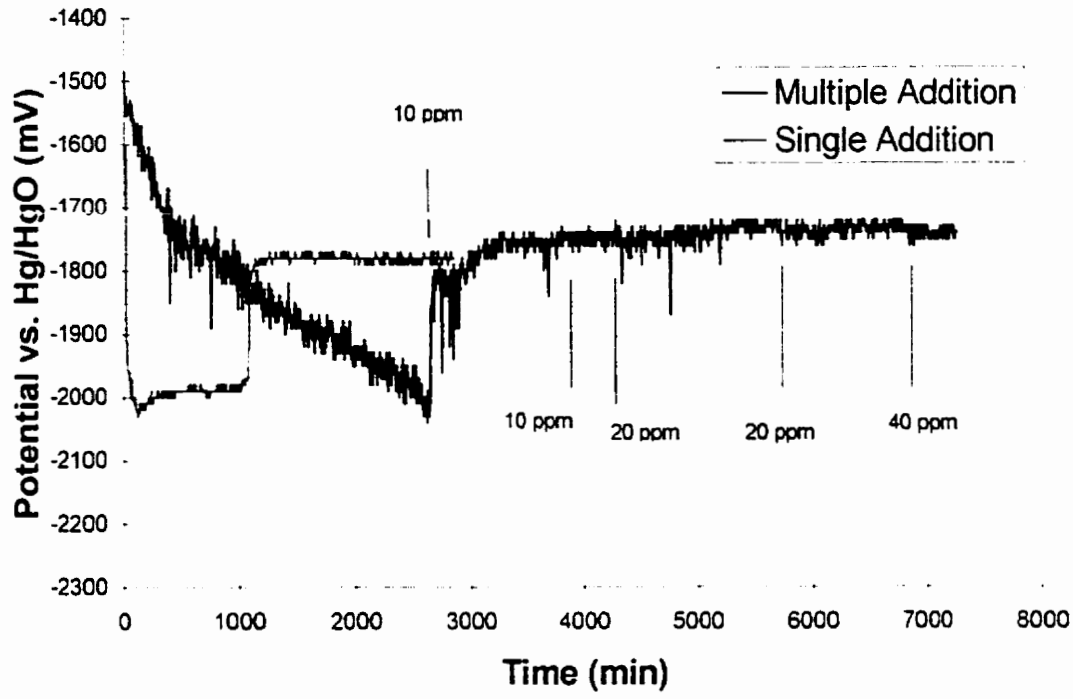

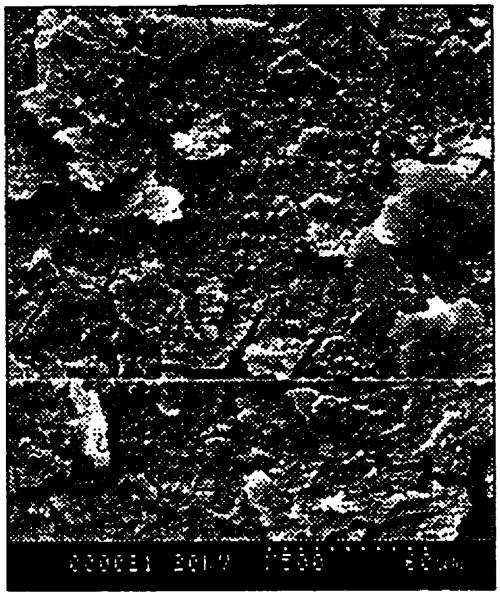

SEM of single addition (100ppm)

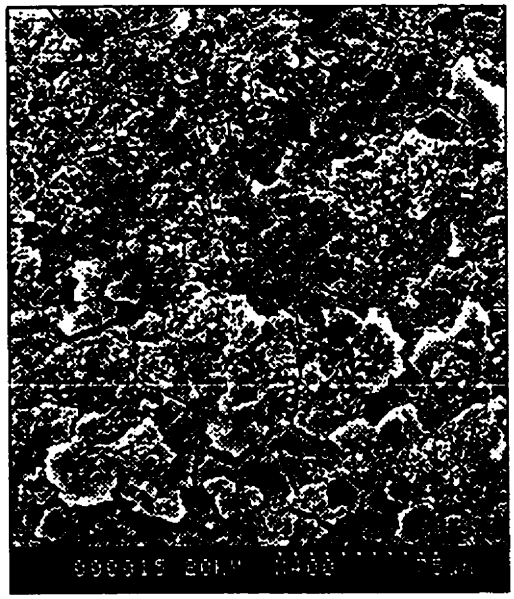

SEM of multiple additions totalling (100ppm)

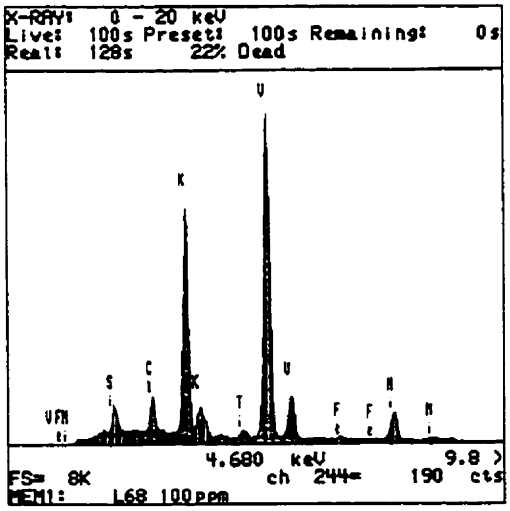

EDX spectrum of single addition

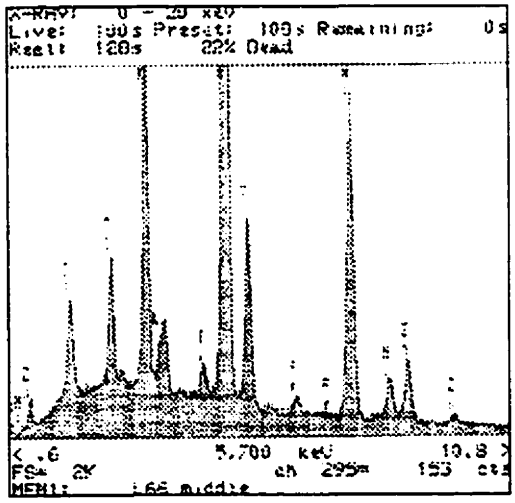

EDX spectrum of multiple addition

Fig. 5.1.27 : SEM and EDX spectrum of electrode surface after single and multiple catalyst additions.

5.1.10 Effect of Impurities

This section includes the results from the tests using both treated (for pre-electrolysis procedure refer to section 4.3.2) and non-treated electrolyte. Fig. 5.1.28 shows the chronopotentiograms using both types of electrolytes with 100 ppm catalyst addition. There was a difference between the potentials before and after catalyst addition. Before addition, the potential of the treated and non-treated electrolyte was -2000mV and -1850mV respectively. After addition, the potential of the treated and non-treated electrolyte was -1800mV and -1710mV respectively.

Fig. 5.1.29 shows the SEM micrograph and corresponding EDX spectrum of electrode surface after a catalyst addition using both the treated and non-treated electrolyte. Using non-treated electrolyte, the surface coating was flat with no cracks. Using the treated electrolyte, the coating was rougher and had cracks. The coating using non-treated electrolyte was composed of both vanadium and iron in similar quantity, while the coating of treated electrolyte had vanadium as the major specie.

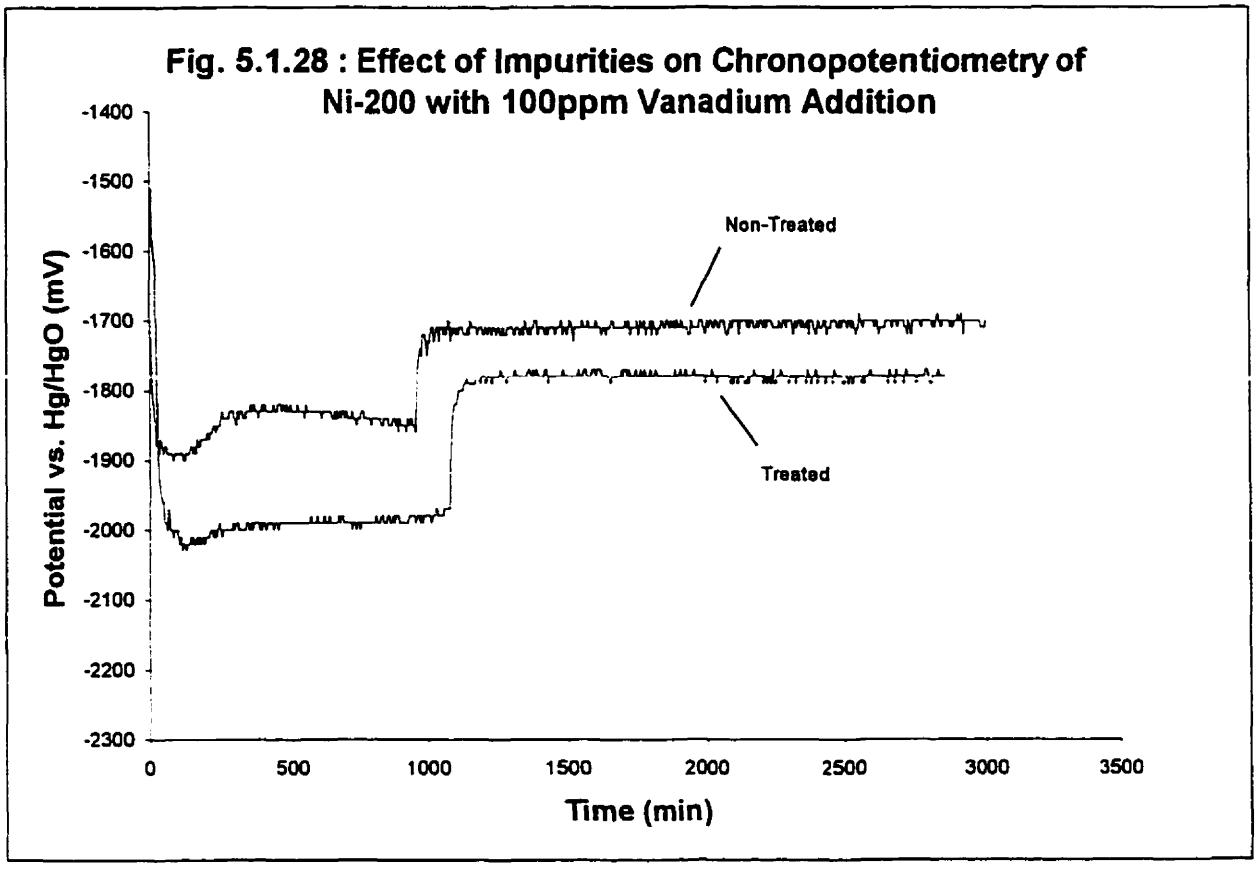
Fig. 5.1.28 : Effect of Impurities on Chronopotentiometry of Ni-200 with 100ppm Vanadium Addition
Potential vs. Hg/HgO (mV)
-1400
-1500
-1600
-1700
-1800
-1900
-2000
-2100
-2200
-2300
Non-Treated
Treated
0
500
1000
1500
2000
2500
3000
3500
Time (min)

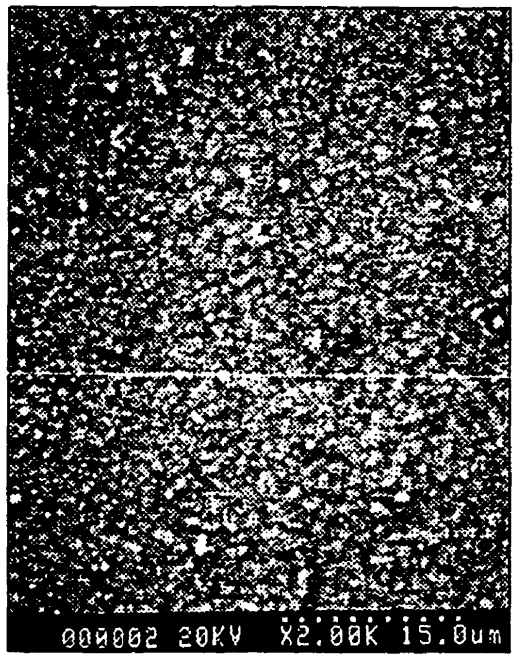

SEM on coating using non-treated KOH (100ppm)

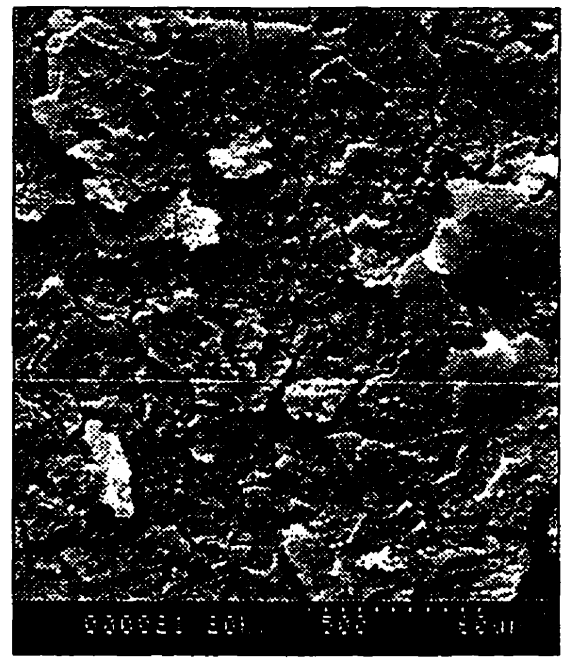

SEM on coating using treated KOH (100ppm)

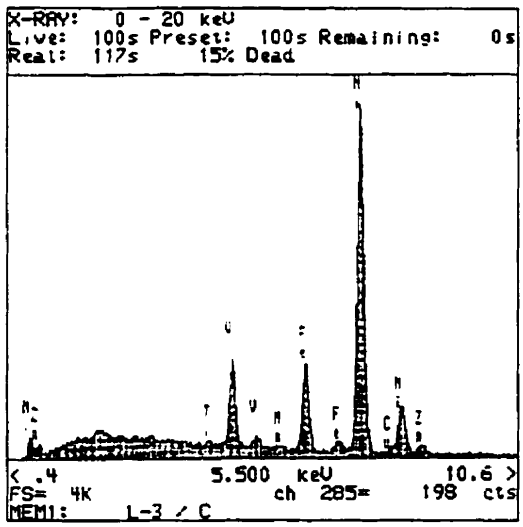

EDX spectrum of coating using non-treated KOH.

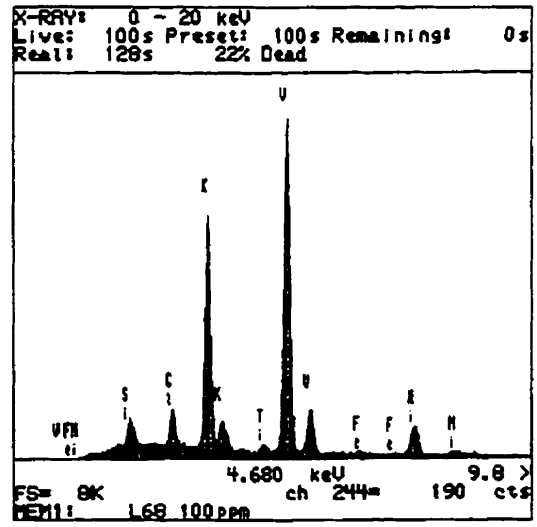

EDX spectrum of coating using treated KOH.

Fig. 5.1.29 : SEM and EDX spectrum of electrode surface after catalyst addition using treated and non-treated electrolyte.

5.1.11 XRD and XPS Analysis on Electrode Surface

The results of XRD and XPS analysis of the coated Ni-200 electrode surface will be presented in this section. Fig. 5.1.30 shows the XRD spectrum after catalyst addition. The peaks positions, d, were compared with the literature values of nickel and several vanadium oxides listed in Table 5.1.1. Except for nickel, there was no match of the experimental values with the listed vanadium species. The intensities of the sample d values were unable to obtain since the amount of the coating was too small for accurate analysis. One purpose of this spectrum will be to compare with the coating formed on Ni-base amorphous alloy electrode.

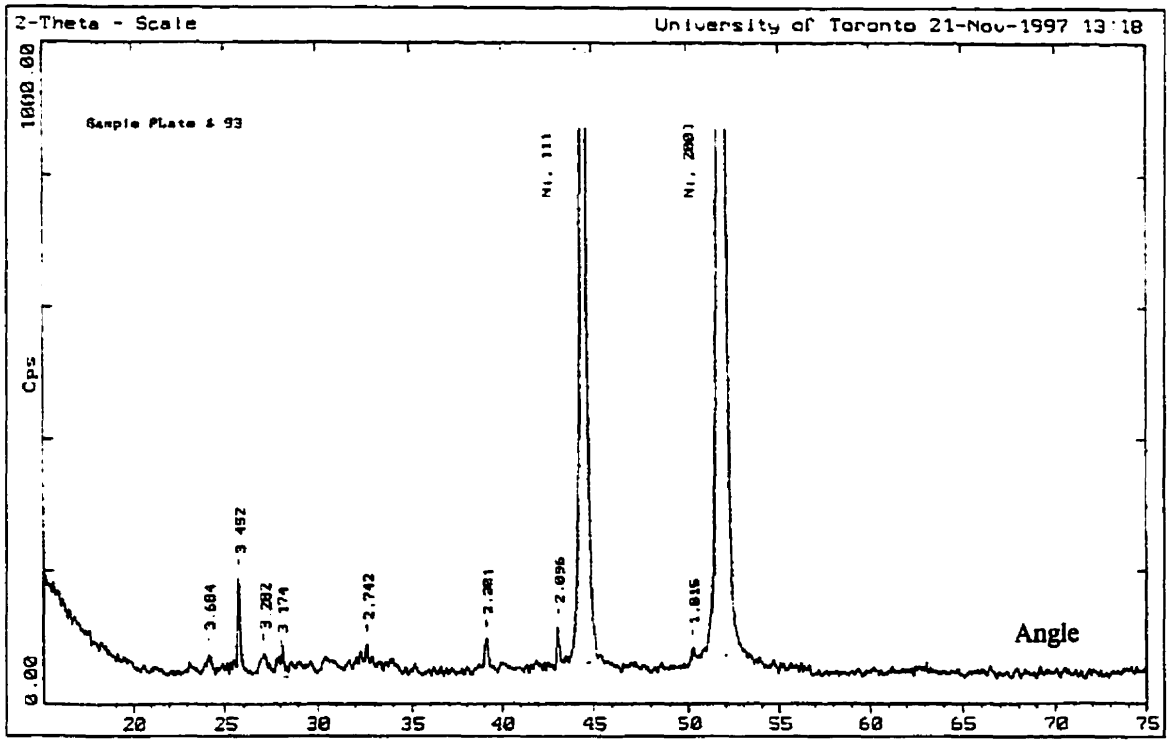

Fig. 5.1.30 XRD spectrum of electrode surface after catalyst addition.

Table 5.1.1 : Literature and Experimental Values of XRD Peak Values, d, and intensities, I, of Nickel and Several Vanadium Oxides [73].

Vanadium	V_2O_5	VO_2	V_2O_4	V_2O_3	Nickel	Experimental values
d I	d I	d I	d I	d I	d I	d I
2.14 100,	4.38 100,	3.25 100,	3.20 100,	1.69 100,	2.03 100,	1.76 100,
1.24 20,	3.40 90,	3.15 100,	2.43 60,	2.70 80,	1.76 40,	1.815 1.05,
1.51 10	2.88 70	2.44 50	2.14 50	3.65 60	1.25 20,	2.03 42.56,
					1.06 20,	2.096 1.5,
					0.79 20	2.301 1.23,
						2.742 1.14,
						3.174 1.09,
						3.282 0.93,
						3.452 2.46,
						3.684 0.92

Fig. 5.1.31 and 5.1.32 show the XPS spectra of electrode surface after catalyst addition with O1s peak and V2P peaks respectively. Table 5.1.2 shows the literature values of XPS binding energies of several vanadium oxides which would be used to compare with the experimental values. Table 5.1.3 shows the experimental values of the XPS binding energies. It was found that, the coating contained both V^{3+} and V^{5+} species.

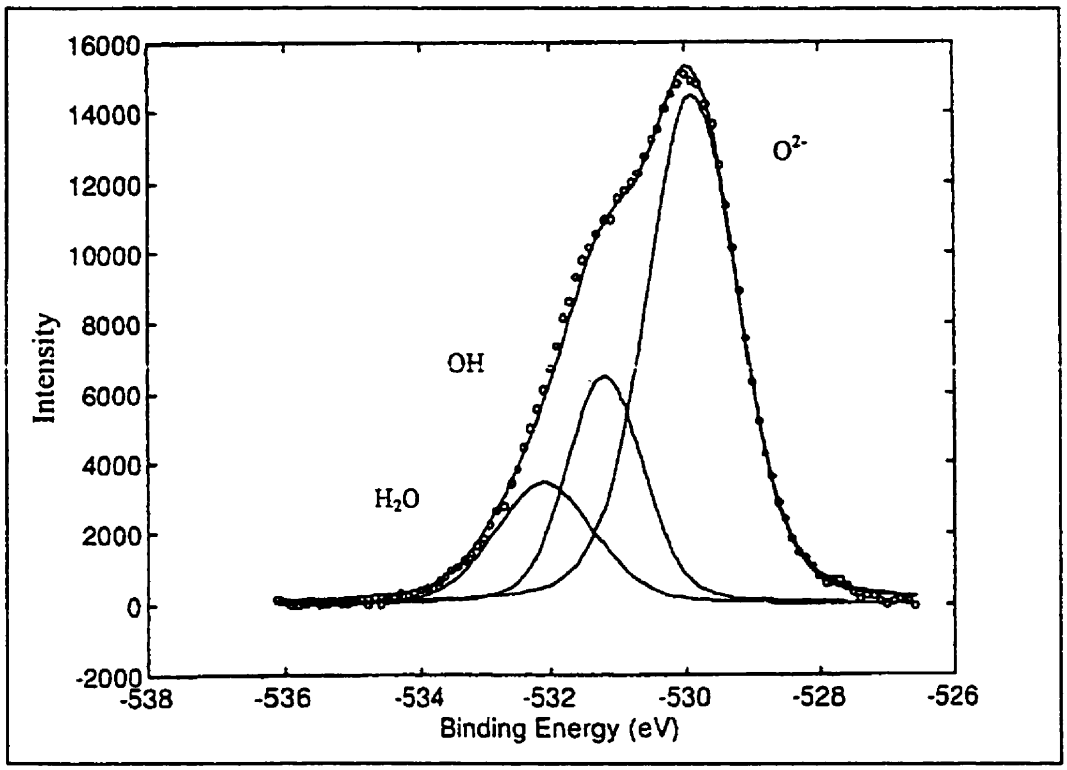

Fig. 5.1.31 XPS spectrum of Ni-200 after catalyst addition showing O 1s peak.

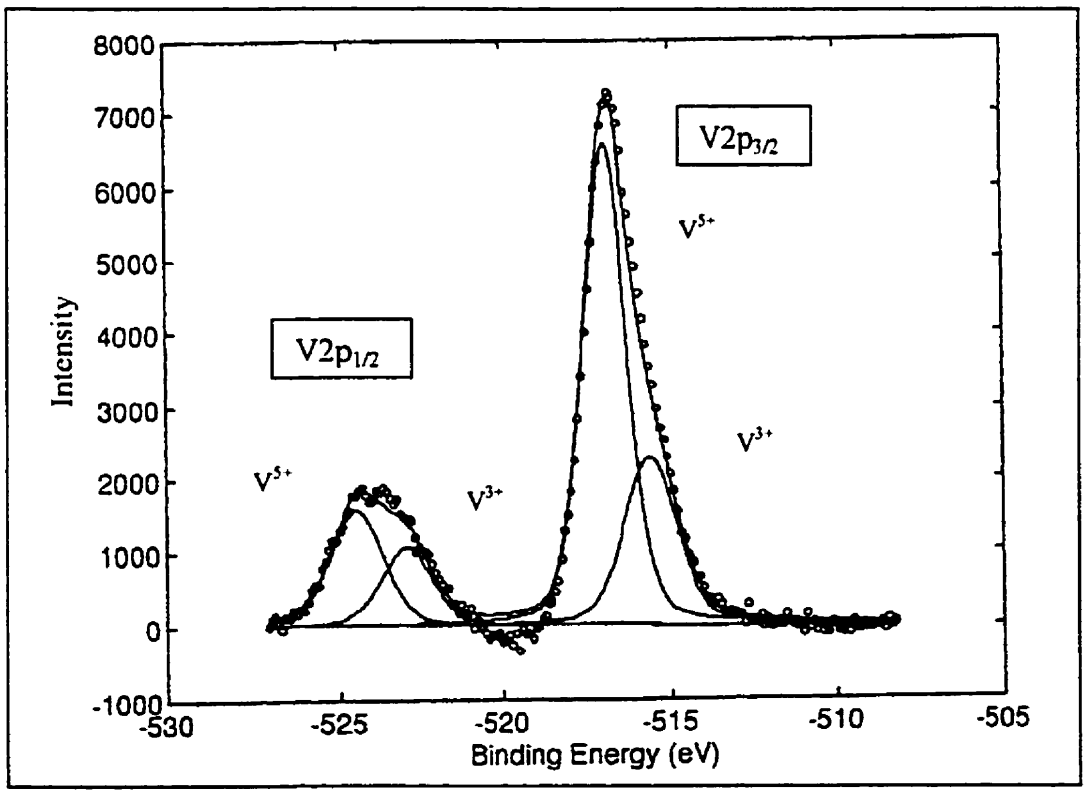

Fig. 5.1.32 XPS spectrum of Ni-200 after catalyst addition showing V 2P peaks.

Table 5.1.2 : Literature Values of XPS Binding Energies of Several Vanadium Oxides.

Shell	Species	Binding Energies (eV)	Δ eV	References	FWHM (eV)
V2p$_{1/2}$	V_2O_5	523.8,		54,	
		524.4,	7.48	55,	
		524.8,	7.6	56,	
		524.3	7.4	59	3.7
	V_2O_3	523,	7.58	55,	
		523.2,	6.9	58,	
		523.3	7.6	59	4.9
	VO_2	523.1,	7.0	54,	
		523.5	7.3	59	4.5
	V	520.3,	7.6	54,	
		519.7,	7.67	55,	
		519.6,	7.64	56,	
		519.9	7.5	59	2.4
V2p$_{3/2}$	V_2O_5	517.1,		52,	
		517.5,		53,	
		516.4,		54,	3.0,
		517,		55,	1.0,
		517.2,		56,	
		518.1,		57,	
		516.9		59	1.6
	V_2O_3	515.5,		55,	3.0
		516.6,		57,	
		516.3,		58,	
		515.7		59	4.2
	VO_2	516.1,		54,	3.4,
		516.2		59	3.2

Shell	Species	Binding Energies (eV)	Δ eV	References	FWHM (eV)
	V	512.7, 512.1, 512, 512.4		54, 55, 56, 59	1.7, 1.0, 2.0
O1s	V_2O_5	530.3, 530.4, 529.6, 529.8, 529.8		52, 53, 54, 55, 59	 1.7
	V_2O_3	530.3, 530.7, 530.1		55, 58, 59	 1.6
	VO_2	529.8, 529.9		54, 59	 1.8

Table 5.1.3 : Experimental binding energies for vanadium species for catalyst modified Ni-200 electrode surface.

Sample	Binding Energy (eV)	FWHM (eV)	Valence State	Chemical Species
Vanadium ($V\ 2p_{3/2}$)	516.87	1.48	+5	V_2O_5
	515.56	1.80	+3	V_2O_3
($V\ 2p_{1/2}$)	524.47	1.80	+5	V_2O_5
	523.05	1.80	+3	V_2O_3
Oxygen	529.94	1.61	-2	oxide of V
	531.23	1.30	-2	OH^- of V
	532.06	1.72	-2	water

The energy difference of $V2p_{3/2}$ and $V2p_{1/2}$ (eV) from the analysis are:

V_2O_5 : 7.6

V_2O_3 : 7.49

5.2 Ni-base Amorphous Alloy ($Ni_{50}Co_{25}P_{15}B_{10}$)

5.2.1 Ni-base Amorphous Alloy

The results obtained for $Ni_{50}Co_{25}P_{15}B_{10}$ samples without catalyst addition will be presented in this section. Fig. 5.2.1 shows the SEM micrograph for an as-polished $Ni_{50}Co_{25}P_{15}B_{10}$ sample and Fig. 5.2.2 shows the corresponding EDX spectrum for this sample. The featureless smooth surface shown in Fig. 5.2.1 serves as a standard to compare with the coated $Ni_{50}Co_{25}P_{15}B_{10}$ electrode surfaces in the later sections. The corresponding EDX spectrum shows Ni, Co and P peaks of the $Ni_{50}Co_{25}P_{15}B_{10}$ electrode.

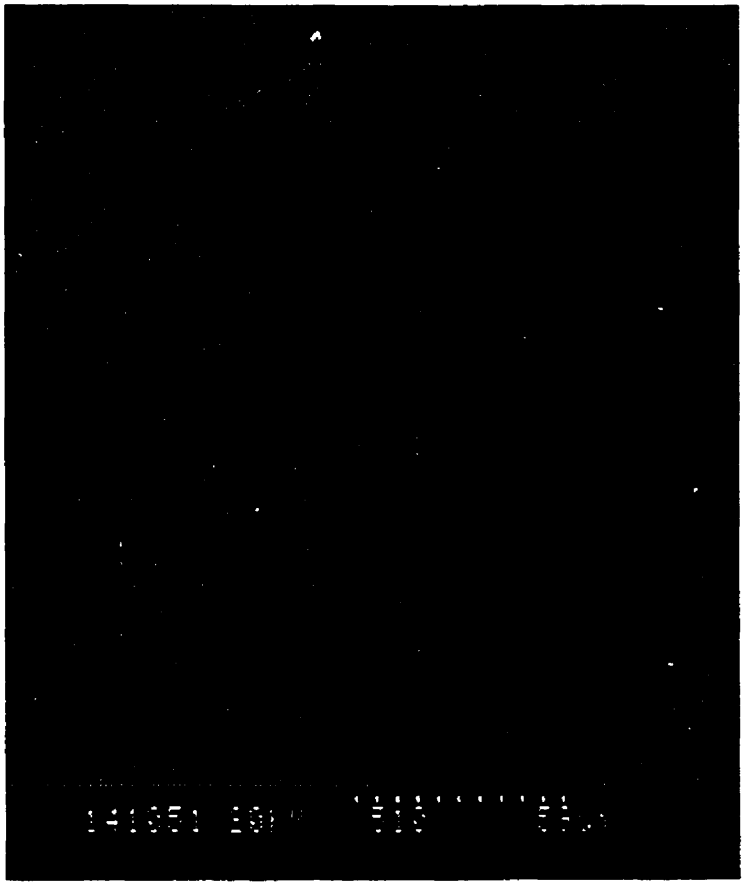

Fig. 5.2.1 SEM micrograph showing as-polished $Ni_{50}Co_{25}P_{15}B_{10}$ sample.

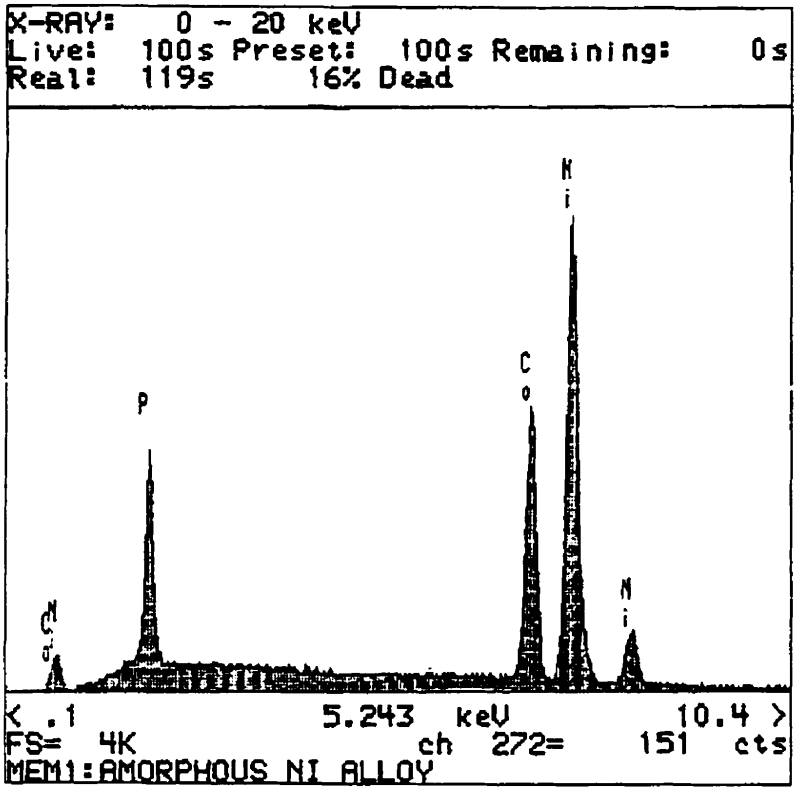

Fig. 5.2.2 EDX spectrum of as-polished $Ni_{50}Co_{25}P_{15}B_{10}$ sample.

5.2.2 $Ni_{50}Co_{25}P_{15}B_{10}$ with 50 ppm Catalyst Addition

The results obtained for an $Ni_{50}Co_{25}P_{15}B_{10}$ sample with 50 ppm catalyst addition will be presented in this section. Fig. 5.2.3 shows the chronopotentiograms for three separate tests. The final potential after the addition of catalyst was about -1800mV for all three tests.

Fig. 5.2.4 shows the SEM micrograph for the electrode after 50 ppm catalyst addition and Fig. 5.2.5 shows the corresponding EDX spectrum for this sample. The SEM shows a rough flat surface with no crack in the coating. Vanadium was the major component of the coating with the presence of iron as shown in the corresponding EDX spectrum.

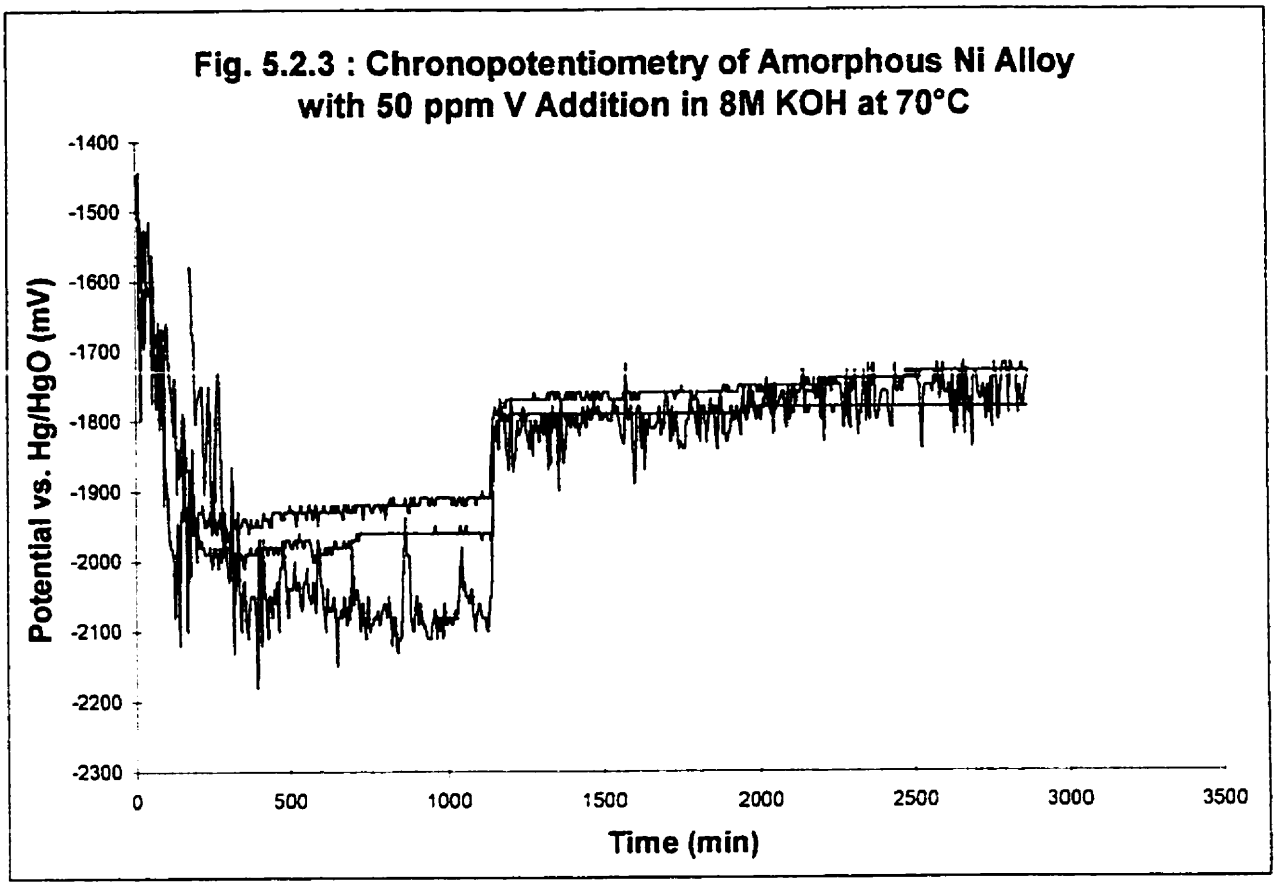
Fig. 5.2.3 : Chronopotentiometry of Amorphous Ni Alloy with 50 ppm V Addition in 8M KOH at 70°C
Potential vs. Hg/HgO (mV)
-1400
-1500
-1600
-1700
-1800
-1900
-2000
-2100
-2200
-2300
0
500
1000
1500
2000
2500
3000
3500
Time (min)

Fig. 5.2.4 SEM micrograph showing amorphous alloy after 50 ppm catalyst addition.

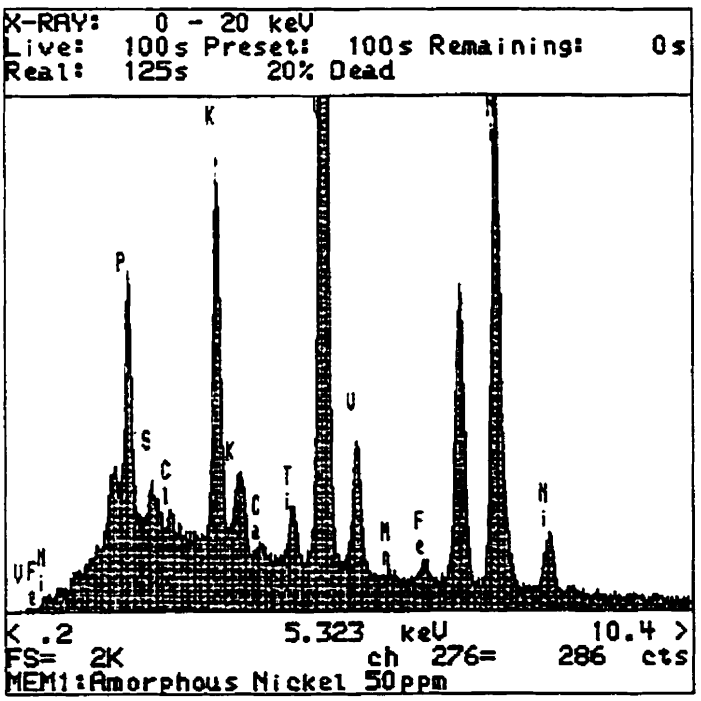

Fig. 5.2.5 EDX spectrum of amorphous alloy after 50 ppm catalyst addition.

5.2.3 $Ni_{50}Co_{25}P_{15}B_{10}$ with 100 ppm Catalyst Addition

The results obtained for an $Ni_{50}Co_{25}P_{15}B_{10}$ sample with 100 ppm catalyst addition will be presented in this section. Fig. 5.2.6 shows the chronopotentiograms for three separate tests. The potential dropped to -1800mV after the catalyst addition and then continued to decrease after about 600 min of polarization. The final potential after the addition of catalyst was about -1700mV for all three tests.

Fig. 5.2.7 shows the SEM micrograph for the electrode after 100 ppm catalyst addition and Fig. 5.2.8 shows the corresponding EDX spectrum for this sample. The SEM shows a multi-layer cracked coating. The coating contained mainly vanadium with a trace amount of iron as shown in the EDX spectrum. Except for vanadium, all other peaks were much smaller than those in 50ppm catalyst addition.

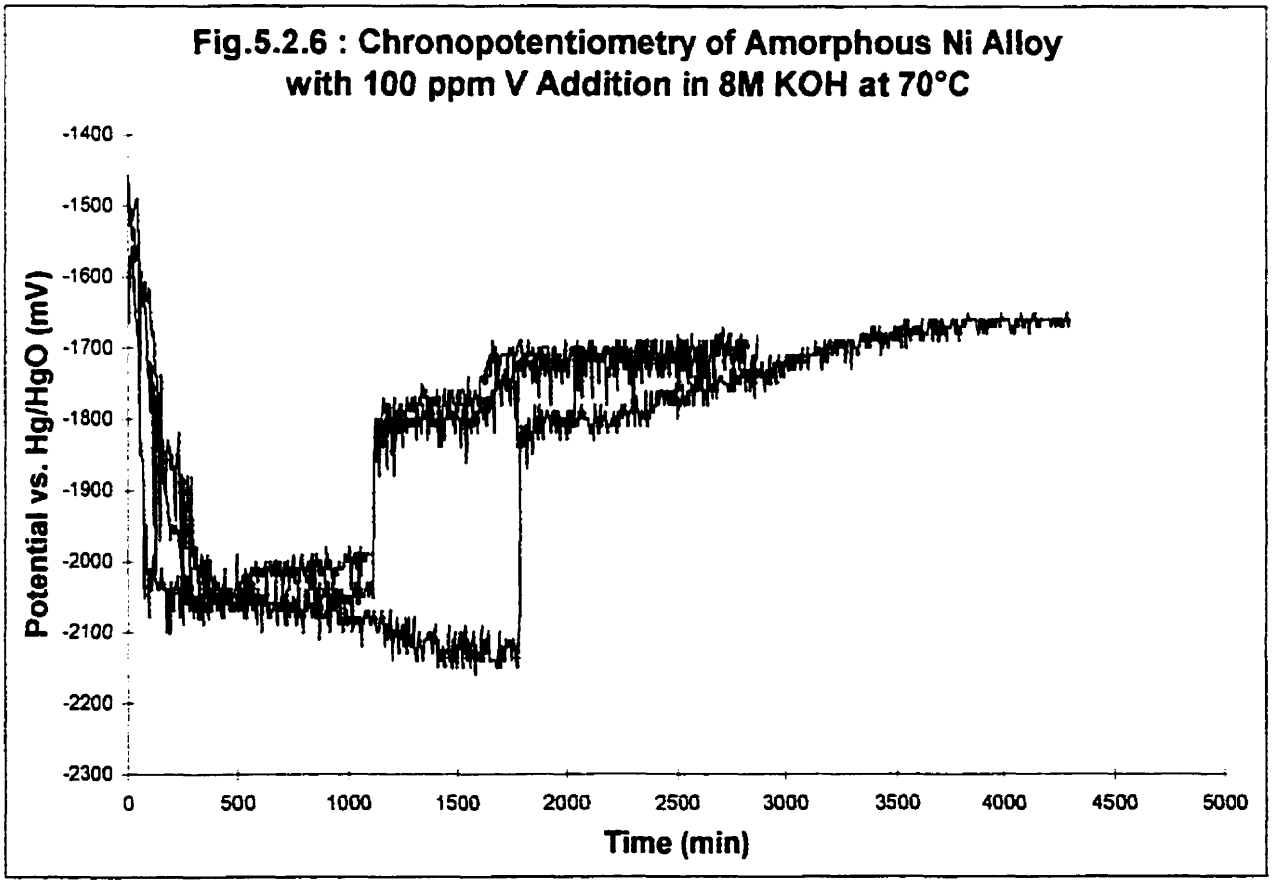

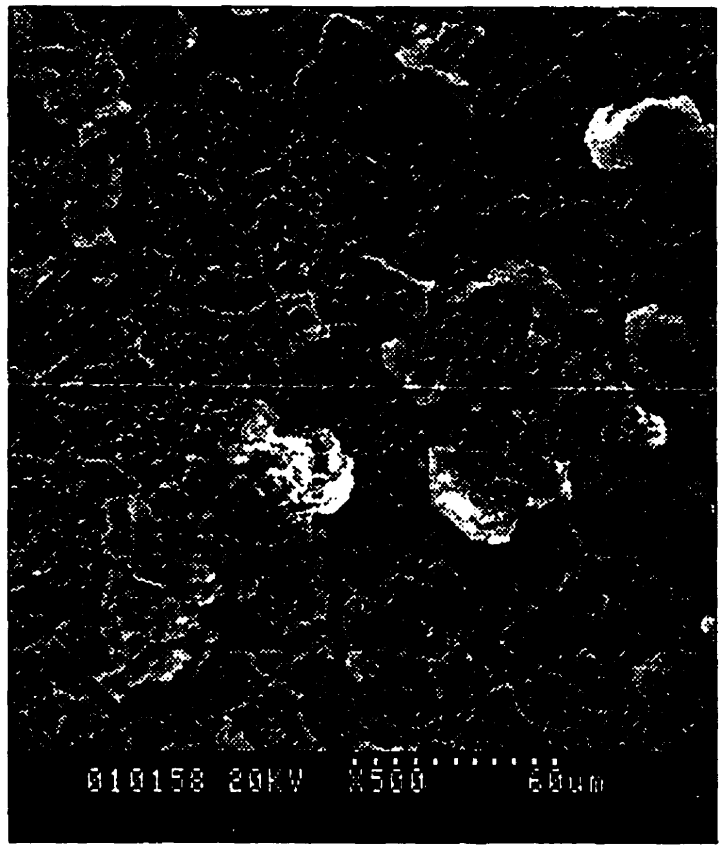

Fig. 5.2.7 SEM micrograph showing amorphous alloy after 100 ppm catalyst addition.

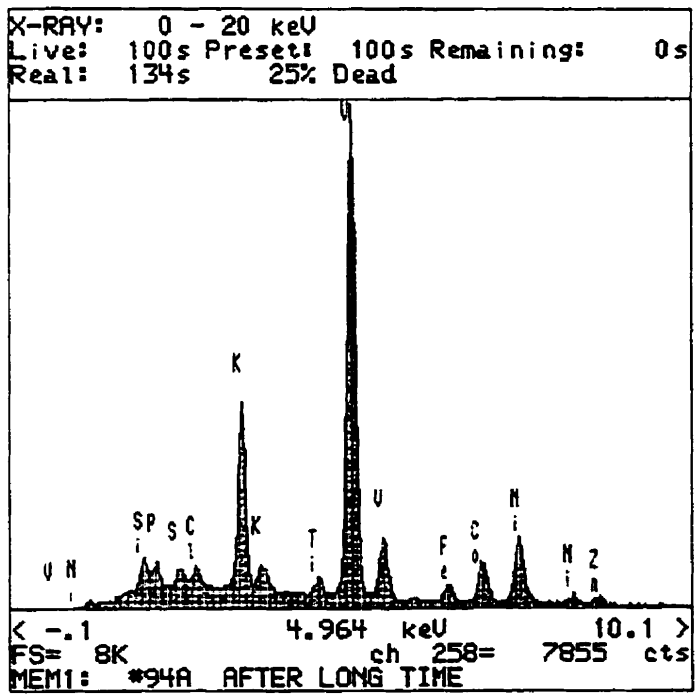

Fig. 5.2.8 EDX spectrum of amorphous alloy after 100 ppm catalyst addition.

5.2.4 $Ni_{50}Co_{25}P_{15}B_{10}$ with 500 ppm Catalyst Addition

The results obtained for a $Ni_{50}Co_{25}P_{15}B_{10}$ sample with 500 ppm catalyst addition will be presented in this section. Fig. 5.2.9 shows the chronopotentiograms for three separate tests. The final potential after the addition of catalyst was about -1800mV for the tests.

Fig. 5.2.10 shows the SEM micrograph for the electrode after 500 ppm catalyst addition and Fig. 5.2.11 shows the corresponding EDX spectrum for this sample. The surface was fully covered by a multi-layer coating with cracks all over it. Vanadium was almost the only component of the coating with no iron present as shown in the EDX spectrum.

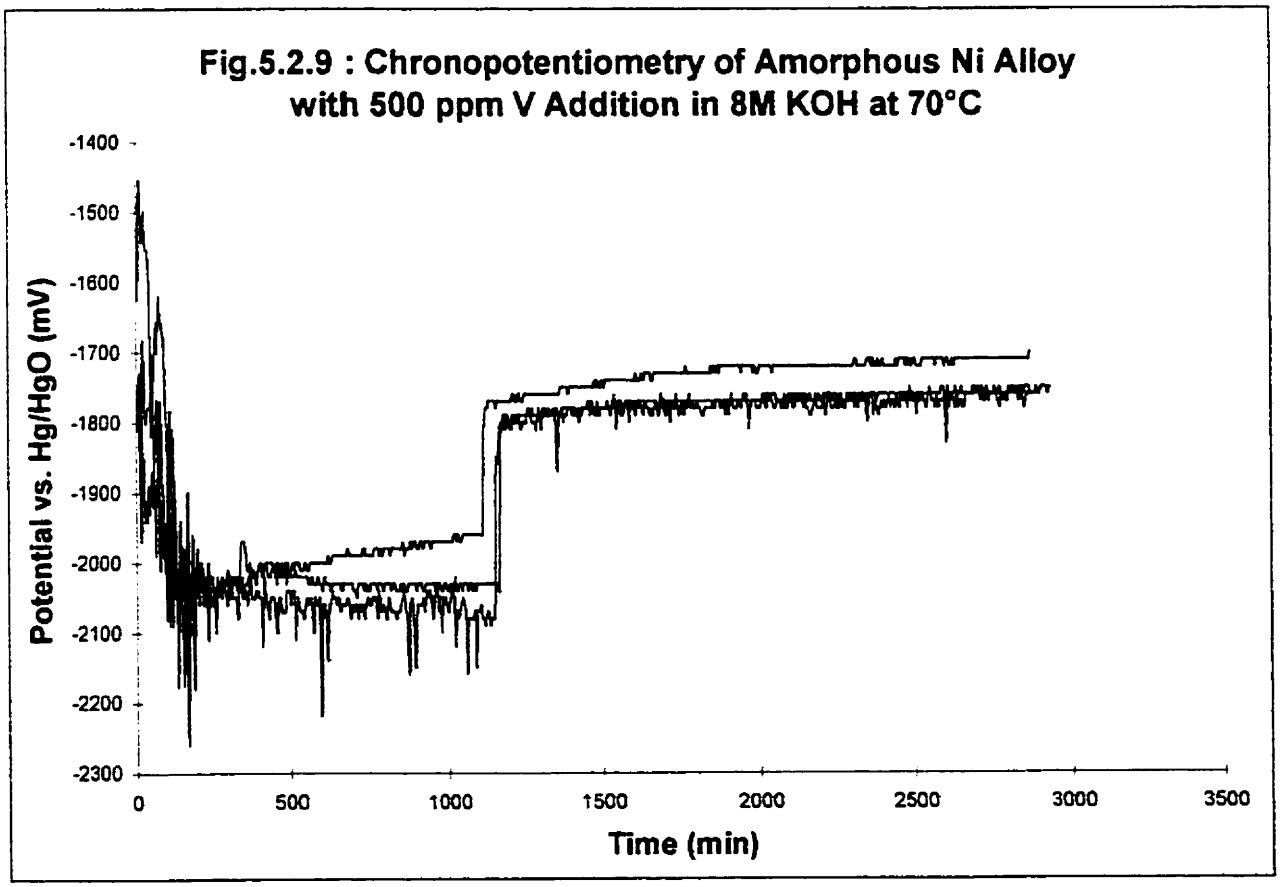

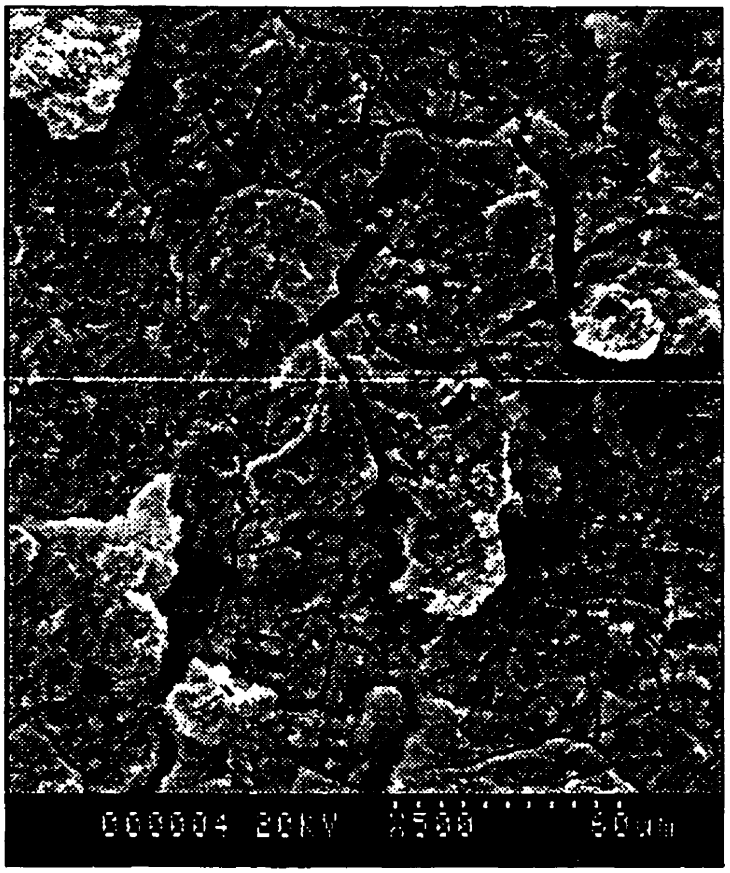

Fig. 5.2.10 SEM micrograph showing amorphous alloy after 500 ppm catalyst addition.

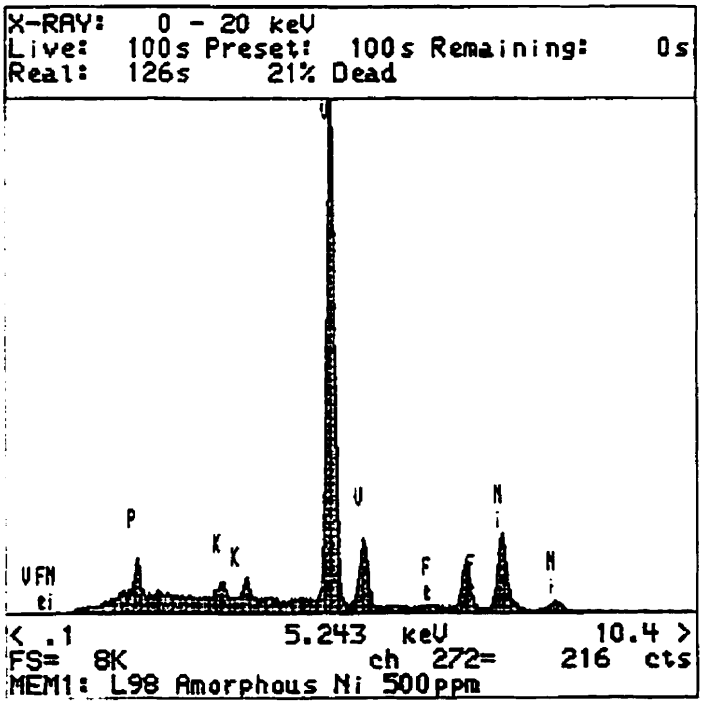

Fig. 5.2.11 EDX spectrum of amorphous alloy after 500 ppm catalyst addition.

5.2.5 Effect of Catalyst Concentration

This section will summarize the effect of different catalyst concentration additions on the $Ni_{50}Co_{25}P_{15}B_{10}$ electrode potential. Fig. 5.2.12 shows the potential versus catalyst concentration plot. The electrode potential was quite variable with some measurements at 100ppm vanadium addition showing -1700mV. Fig. 5.2.13 shows the SEM images of the electrode surface after different vanadium concentration additions.

A rough flat coating was found at 50ppm catalyst addition and multi-layer coatings were found at higher catalyst concentrations.

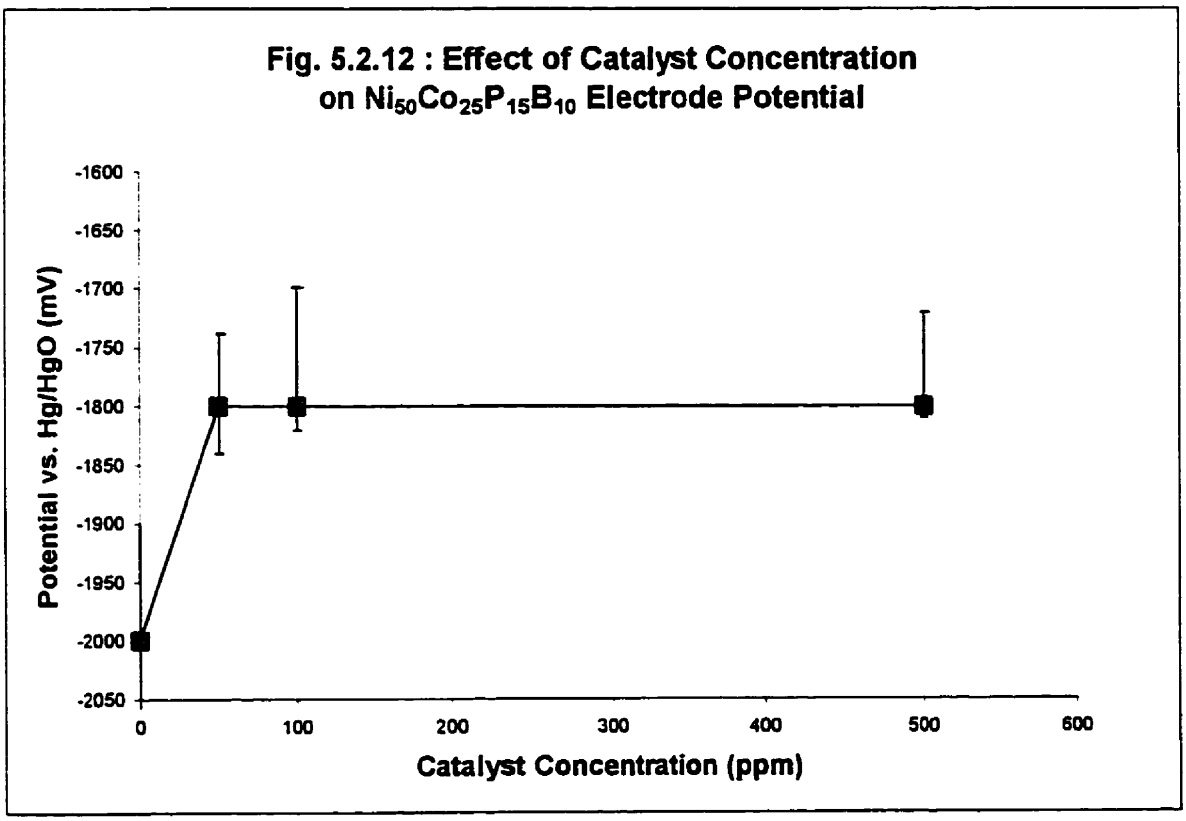

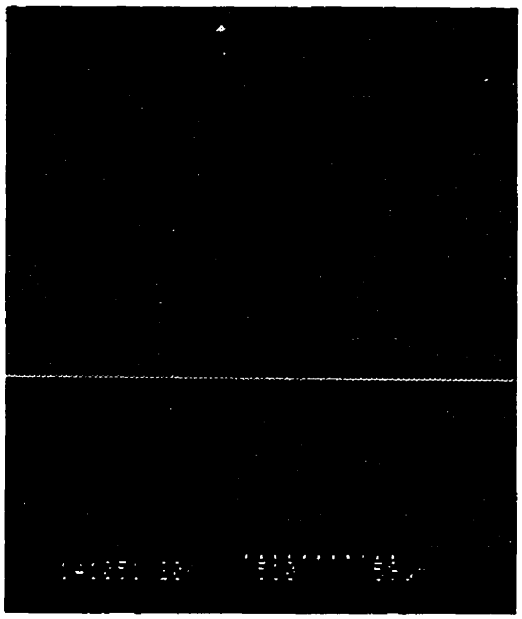

$Ni_{50}Co_{25}P_{15}B_{10}$ (as polished)

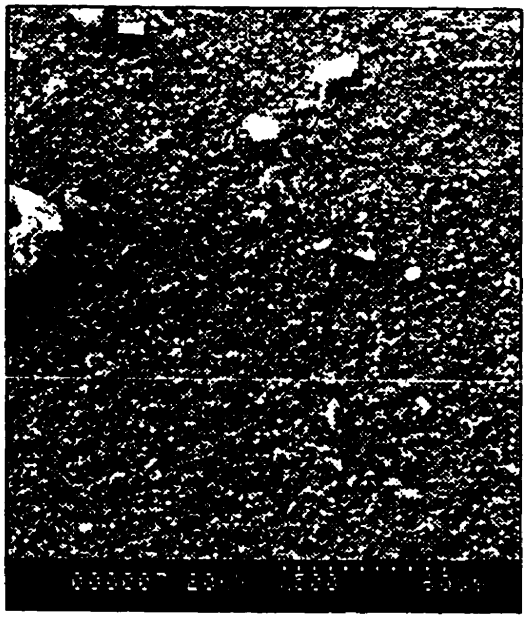

50 ppm

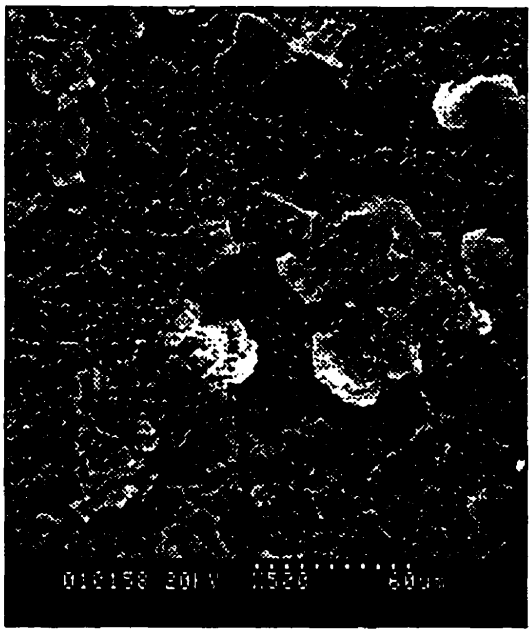

100 ppm

500 ppm

Fig. 5.2.13 : SEM images of electrode surface with different vanadium concentration additions ($Ni_{50}Co_{25}P_{15}B_{10}$).

5.2.6 Tafel Test for $Ni_{50}Co_{25}P_{15}B_{10}$ and $Ni_{50}Co_{25}P_{15}B_{10}$ with 100 ppm Catalyst Addition

Fig. 5.2.14 and Fig. 5.2.15 show the Tafel tests for $Ni_{50}Co_{25}P_{15}B_{10}$ sample before and after 100 ppm catalyst addition respectively.

Fig. 5.2.14 : Tafel Plot on Amorphous Ni Alloy

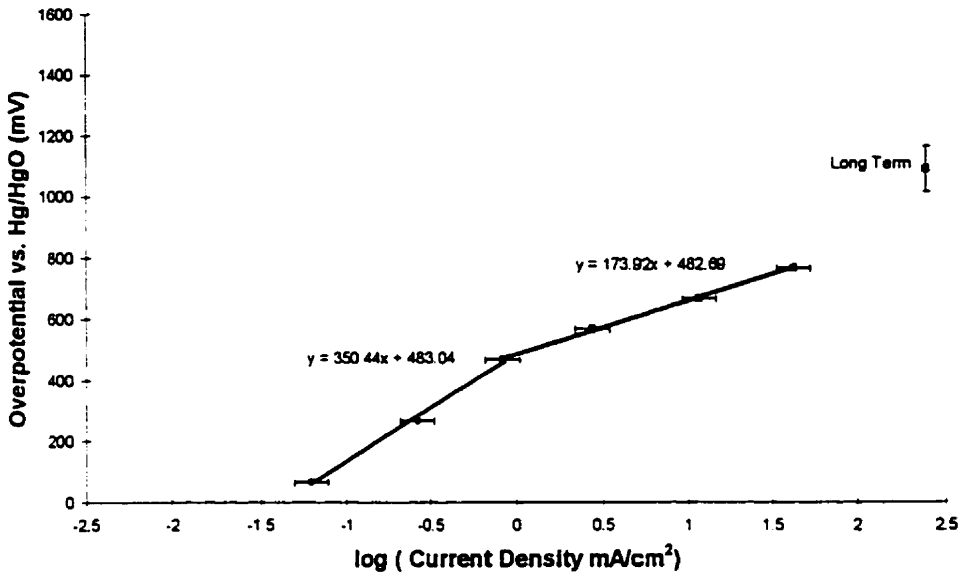

Fig. 5.2.15 : Tafel Plot for Amorphous Ni Alloy After 100 ppm Catalyst Addition

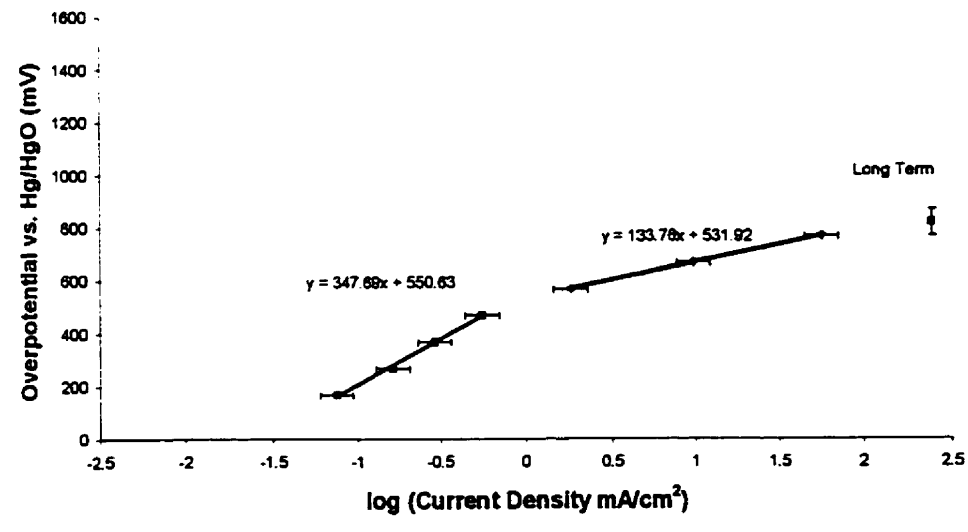

The error bars of the Tafel measurements represented the noise level of the current densities of an experiment. A long term point from the chronopotentiometry measurement was included in the figures which showed the vanadium coated electrode had Tafel data closer to steady state value.

5.2.7 XRD Analysis on Ni-base Amorphous Alloy Electrode Surface

The result of XRD analysis of the Ni-base amorphous alloy electrode surface will be presented in this section. Fig. 5.2.16 shows the XRD spectrum after catalyst addition. There is a broad peak the spectrum at 45°. The rest of the small crystalline peaks which correspond to the coating match Ni-200 as follows:

Amorphous Ni Alloy	Nickel
2.297	2.301
2.742	2.742
3.449	3.452

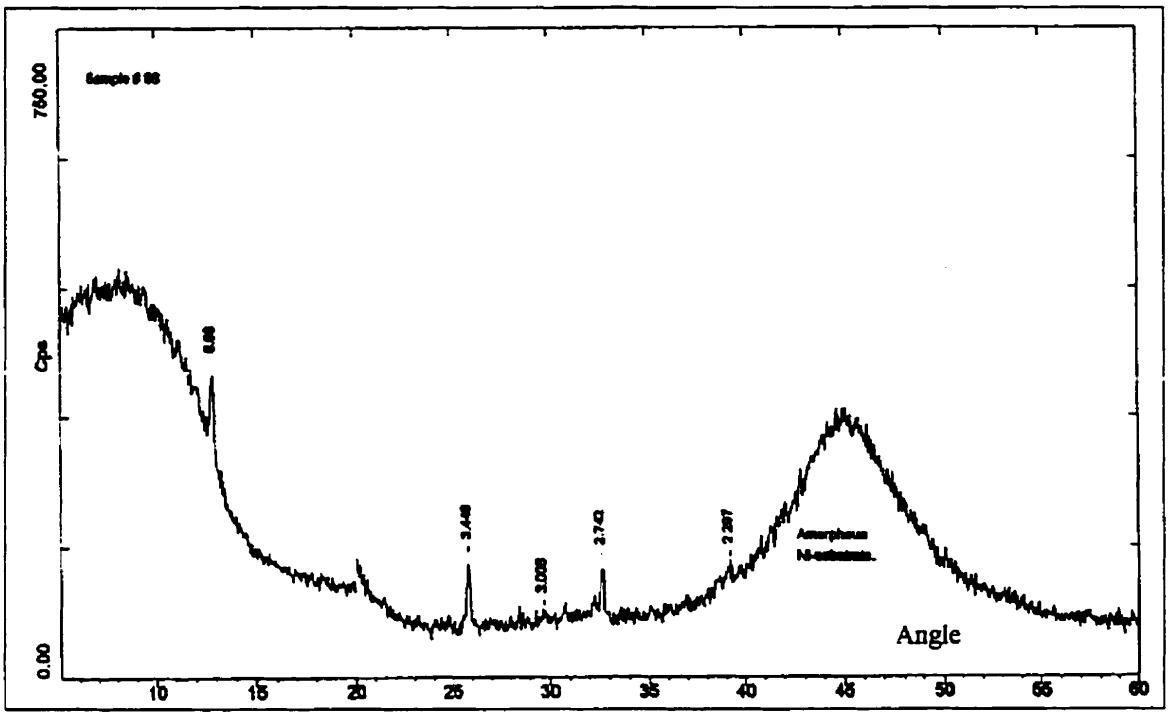

Fig. 5.2.16 XRD spectrum of Amorphous Ni Alloy electrode surface after catalyst addition.

5.3 Comparison of Ni-200 with $Ni_{50}Co_{25}P_{15}B_{10}$ Results

5.3.1 Effect of Catalyst Concentration with Different Electrode Materials

Fig. 5.3.1 shows the final potential versus catalyst concentration plot of both Ni-200 and $Ni_{50}Co_{25}P_{15}B_{10}$. Except for some fluctuating for 100ppm catalyst addition, the final potential of both electrode materials were the same at -1800mV after the catalyst additions.

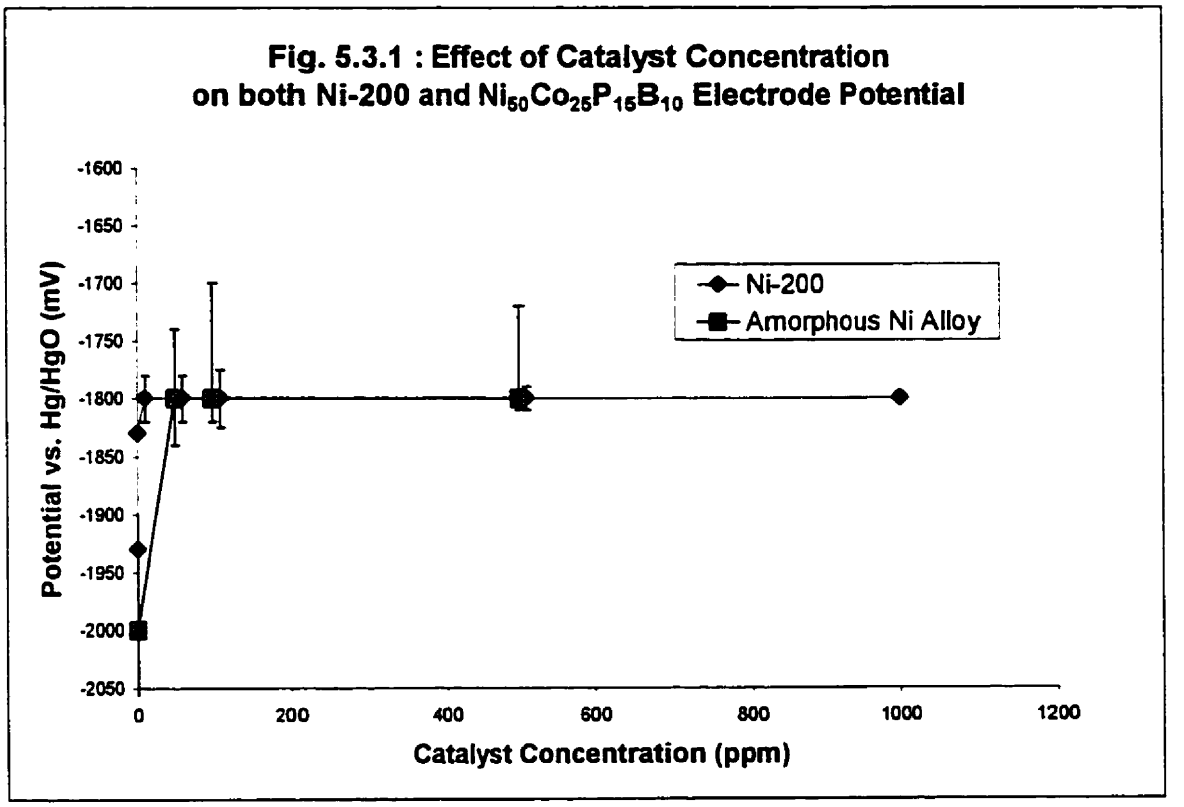

5.3.2 Tafel results with Different Electrode Materials

This section will present the Tafel plots before and after catalyst additions of both electrode materials and compare the two electrode materials. Fig. 5.3.2 shows the Tafel plot of Ni-200 at two sweep rates at 10 hours and half an hour between each measurement. Fig. 5.3.3 shows the Tafel plot of $Ni_{50}Co_{25}P_{15}B_{10}$ with and without 100ppm catalyst addition. Fig. 5.3.4 shows the Tafel plot of Ni-200 and $Ni_{50}Co_{25}P_{15}B_{10}$ with 100ppm catalyst addition. Table 5.3.1 shows the Tafel data of both electrode materials which includes overpotential range, exchange current densities, i_o, and Tafel slope, b, with and without catalyst additions.

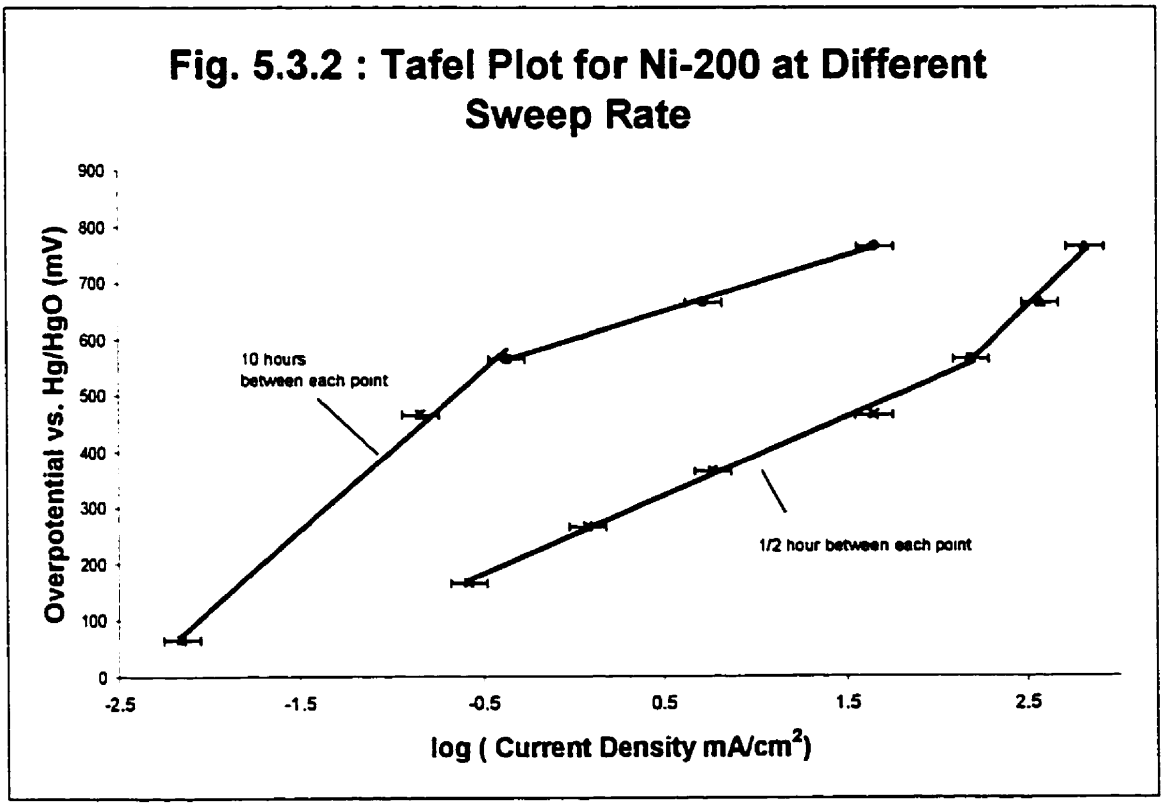

Fig. 5.3.3 : Tafel Plot for Amorphous Ni Alloy and After 100 ppm Catalyst Addition

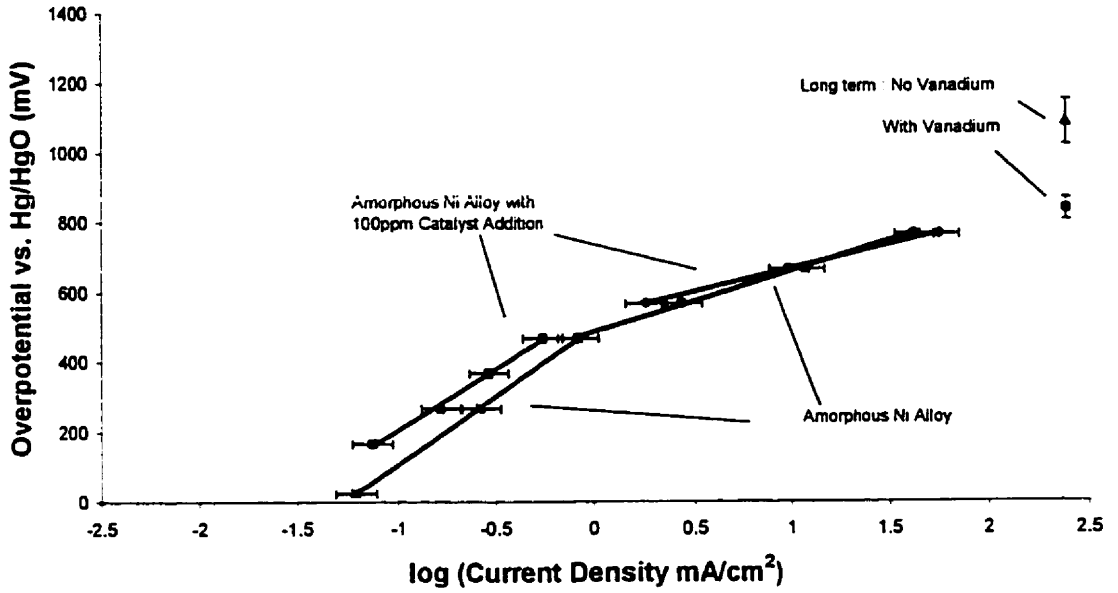

Fig. 5.3.4 : Tafel Plot for Amorphous Ni Alloy and Ni-200 After 100 ppm Catalyst Addition

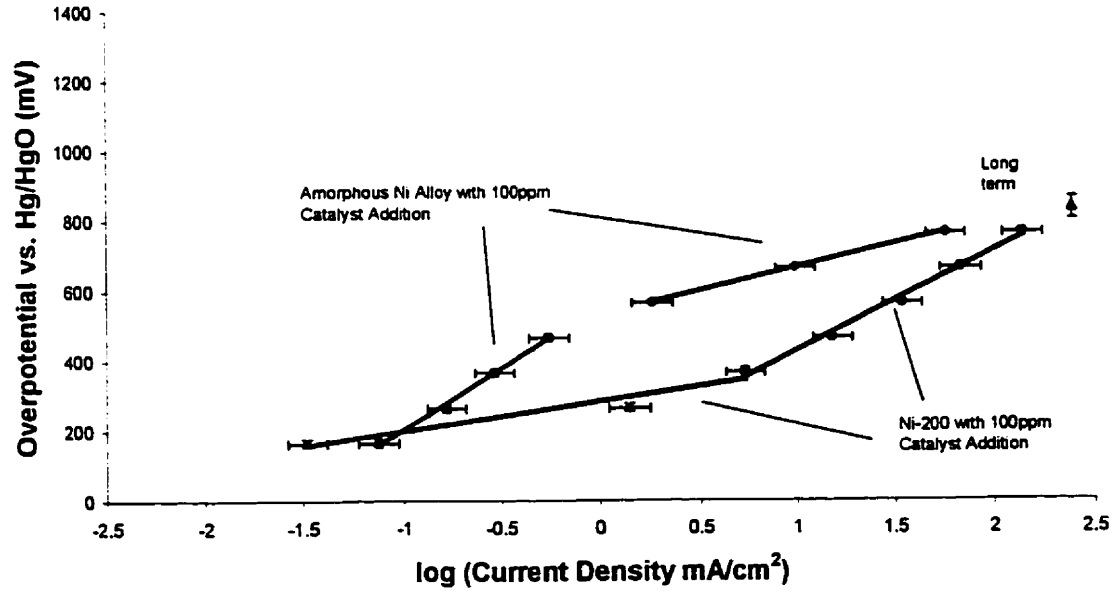

Table 5.3.1 : Tafel Parameters of Ni-200 and $Ni_{50}Co_{25}P_{15}B_{10}$ with and without catalyst.

	Overpotential Range (mV)	i_o (mA/cm^2)	b (mV/dec.)
Ni-200 (no catalyst) 10 hours between points	100 - 550	0.004	286
	550 - 750	0.00000086	99
1/2 hours between points	150 - 550	0.016	140
	550 - 750	2.41	311
(with 100ppm V)	100 - 400	0.00044	84
	400 - 750	0.32	286
$Ni_{50}Co_{25}P_{15}B_{10}$ (no catalyst)	50 - 550	0.042	350
	550 - 750	0.0017	173
(with 100ppm V)	100 - 550	0.026	347
	550 - 750	0.00011	133

All Tafel plots contained two linear regions. Ni-200 showed a significant change of Tafel slopes at different sweep rate. The electrode was deactivated as the sweep rate decreased. With 100ppm catalyst addition, Ni-200 had a larger slope at high overpotentials and was the same value as the slope for Ni-200 at low overpotentials without catalyst addition. For $Ni_{50}Co_{25}P_{15}B_{10}$, the values of the slopes were very similar with and without catalyst addition. At low overpotentials, the values of the slopes were almost the same. At high overpotentials, there was an intersection point between the Tafel

slopes with and without catalyst addition. Above the overpotential of about 600mV, the $Ni_{50}Co_{25}P_{15}B_{10}$ electrode with catalyst addition became more catalytic than that without catalyst addition. In comparing both electrode materials at 100ppm catalyst addition, Ni-200 had lower activity than $Ni_{50}Co_{25}P_{15}B_{10}$ at most current densities but converged to the same overpotential at the current density of $250mA/cm^2$.

5.3.3 Morphology of the Coatings on different Electrode Materials

This section will compare the morphology of the catalyst coatings on both electrode materials (Ni-200 and $Ni_{50}Co_{25}P_{15}B_{10}$). Fig. 5.3.5 shows the surface of the coated electrodes at 50, 100 and 500ppm catalyst additions. At 50ppm catalyst addition, the surface of Ni-200 electrode has a few thicker coated regions than the $Ni_{50}Co_{25}P_{15}B_{10}$ surface. At 100ppm catalyst addition, Ni-200 was fully coated with multi layer coated regions while $Ni_{50}Co_{25}P_{15}B_{10}$ was not fully coated. At 500ppm catalyst addition, both coated surfaces were fully covered with cracked coatings.

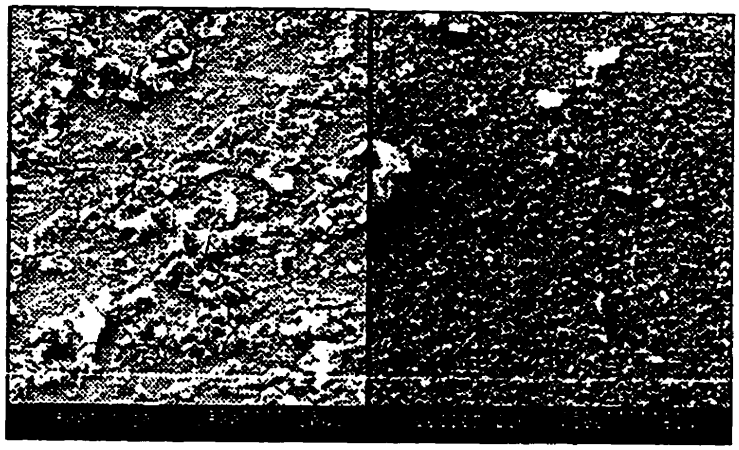

50ppm catalyst addition

Ni-200 $Ni_{50}Co_{25}P_{15}B_{10}$

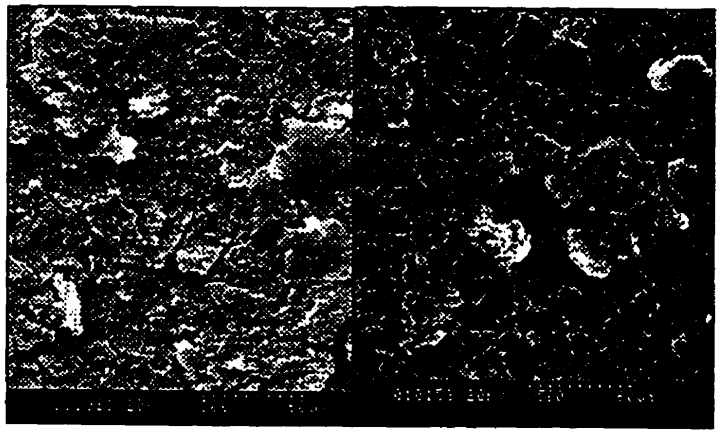

100ppm catalyst addition

Ni-200 $Ni_{50}Co_{25}P_{15}B_{10}$

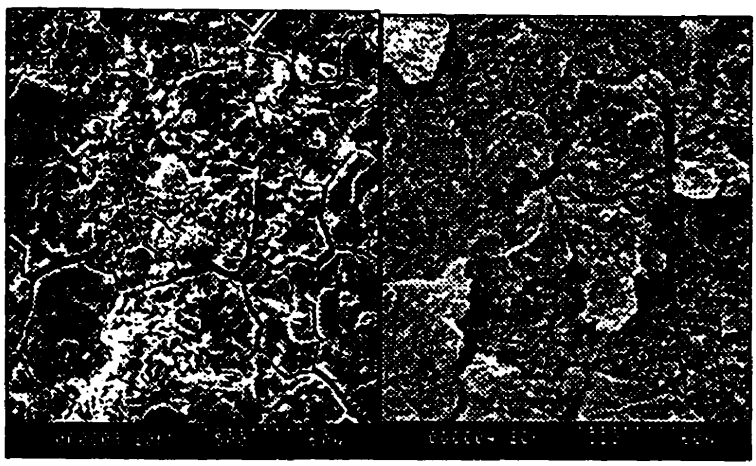

500ppm catalyst addition

Ni-200 $Ni_{50}Co_{25}P_{15}B_{10}$

Fig. 5.3.5 : SEM on Coated Surface of Ni-200 and $Ni_{50}Co_{25}P_{15}B_{10}$ at different catalyst concentration.

6. Discussion

This section will discuss the results presented in Section 5. There are four main sections in the discussion. Section 6.1 will discuss the electrochemical behaviour and the surface properties of the Ni-200 electrodes before and after the addition of vanadium as a homogeneous catalyst. Another electrode material, amorphous nickel base alloy ($Ni_{50}Co_{25}P_{15}B_{10}$), will then be discussed in Section 6.2 and will be compared with the Ni-200 electrodes. Section 6.3 will discuss the effect of impurities in the electrolyte on the cathodic overpotential. Section 6.4 will propose a reaction mechanism to explain the catalyzing effect of the addition of vanadium on the HER.

6.1 Ni-200

6.1.1 Steady State Potentiostatic Measurement (Tafel)

As discussed in Section 3, a Tafel plot is a graph of overpotential versus the log of current density. The overpotentials are the actual measured potential minus the equilibrium potential. An electrochemical reaction mechanism can be described using the Tafel slope, b, by comparing the experimental and the theoretical values.

The equilibrium hydrogen evolution potential at 8M KOH and 70°C is calculated to be -934mV versus Hg/HgO (Appendix A). Fig. 5.1.24 showed that there were two linear regimes in the Tafel plot. At low overpotentials, 100 to 550 mV versus Hg/HgO, a Tafel slope of 286 ± 57 mV/dec. was obtained, while at higher overpotentials, 550 to 750 mV versus Hg/HgO, a Tafel slope of 99 ± 19mV/dec. was obtained. The sweep range of the Tafel plot was from 100mV to 750mV at a step rate of 10 hours between each data

point. Tafel plots with two linear regions were reported by a number of authors. Suzuki [40] had reported two Tafel regions on crystalline nickel electrode, with 120 mV/dec. at very low overpotentials (~0 - 274mV versus Hg/HgO) and 239 mV/dec. at a high overpotentials (~274 - 584mV versus Hg/HgO) which is in good agreement with this work (286 mV/dec.). Lian et al [37] and Kibria et al. [26] also reported two Tafel regions in their results as shown in Table 7. In the overpotential range of 200 - 300mV, the reported Tafel slopes were in the range of 120 - 167 mV/dec. which are in reasonable agreement with Suzuki. A summary of Tafel slopes reported on nickel in different overpotential regimes is summarized in Table 7.

Table 7 : Nickel Tafel slopes in different overpotential range and temperatures

Overpotential range (mV vs. Hg/HgO)	Tafel slope (mV/dec.)	Temperature (K)	Author
100 - 200	80	325	[26]
200 - 400	167	325	
355 - 555	148	303	[37]
555 - 705	96	303	
0 - 316	120	303	[40]
316 - 626	239	303	
145 - 675	158	303	[71]
100 - 550	286 (252)	343 (303)	present work
550 - 750	99 (79)	343 (303)	

From Table 7, it can be seem that there are three Tafel slopes in the overpotential range between 0 to 700 mV. At very low overpotentials, 0 - 200 mV, the Tafel slope is ≤120mV/dec. [26, 40]. At medium overpotentials, 200 - 550 mV, the Tafel slope becomes >120mV/dec. [26, 37, 40]. At high overpotentials, 550- 750 mV, the Tafel slope decreases again to a value around 96 to 99 mV/dec. [37]. The range of overpotential (100 to 750mV) of the Tafel sweep in the present work covered the medium and high overpotentials regions and two linear regions were found. The slopes were in good agreement with the results of Suzuki and Lian et al and the transition point, where the Tafel slope changed, at an overpotential of about 550mV was also consistent with the literature. These results indicated that there is a change in reaction mechanism at about 550mV.

The small Tafel slope obtained above the overpotential of 500mV showed an increase in electroactivity at high overpotentials and current densities. This is of benefit to the operation of industrial electrolysers since they all operate at high current densities (~250 mA/cm^2). The long term steady state galvanostatic measurement was added to the plot in Fig. 5.1.24. The long term overpotential of about 1000mV, was measured after 18 - 20 hours at 250mA/cm^2 from the chronopotentiometry experiments. The Tafel data predicts an overpotential at 250mA/cm^2 of 800mV. This is less than the long term measured value of 1000mV. Thus there appears to be additional loss of activity for long term measurements which may due to continuing impurity deposition or hydride formation.

6.1.2 Scanning Electron Microscopy (SEM) with EDX

The scanning electron micrograph of a polished Ni-200 electrode surface is shown in Fig.5.1.2. The photo shows a flat surface with scratches arising from the final polishing at 1μm and some holes from the metal defects, probably inclusions, of the Ni-200 coupon.

The corresponding EDX spectrum in Fig. 5.1.3 shows prominent peaks for nickel only. The impurities listed in Table 5 were not detected by EDX which has a lower elemental resolution of about 0.5%.

6.1.3 Catalyst Coated Electrodes

6.1.3.1 Chronopotentiometry

Chronopotentiometry was performed using Ni-200 electrodes at various electrolyte catalyst concentrations (0.1, 10, 50, 100, 500 and 1000ppm), with a nominal cathodic current density of 250 mA/cm^2. The experimental results are shown in sections 5.1.2 to 5.1.7. Each potential time plot contains three replicates in order to show the reproducibility of the results. All the experiments showed the same endpoint potential to catalyst addition at the applied current density.

When current was first applied to the electrode, there was always a rapid increase in overpotential. This overpotential increase would usually end in the first 500 minutes and has been ascribed to a number of phenomena. At high current densities or overpotentials, the deactivation process during the first hour of polarization is reported to be due to hydrogen absorption in the electrode, while for longer times the deposition of metal impurities from the electrolyte influences the hydrogen discharge [32]. The

solubility of hydrogen in nickel is < 111μmol/100g [65]. Theoretically the hydrogen concentration in the nickel electrode could reach 20% of the hydrogen concentration at the surface of the electrode after 1 hour of polarization. The calculation of the amount of hydrogen that can diffuse into nickel is shown in Appendix D. Nickel containing hydrogen can form two types of hydride. The α-hydride is a solid solution of hydrogen atoms in the octahedral interstices of nickel and is characterized by a H/Ni ratio of 0.03. Above an atomic ratio of 0.06, the β-hydride phase exists. This phase acts as a diffusion barrier to hydrogen and leads to an increase in overpotential [66].

The electroactivity of nickel could change due to the deposition of various metallic impurities in the electrolyte on the nickel surface such as iron and molybdenum . In KOH electrolyte, the major metallic impurity present is iron. It is known that over this range of overpotentials, iron would electrodeposited on nickel cathodes by two reduction steps [8]:

$$Fe^{3+} + e^- \rightarrow Fe^{2+} \qquad \text{followed by} \qquad Fe^{2+} + e^- \rightarrow Fe$$

The dissolved ferric ions species would reduce to Fe^{2+} species close to the hydrogen equilibrium potential, followed by reduction of Fe^{2+} to metallic iron close to 200mV hydrogen overpotential. Since these are diffusion limited steps and occur in parallel with the HER, the Tafel slope would change accordingly. According to the revised Pourbaix diagram of Fe [75], the dissolved Fe^{3+} is $Fe(OH)_4^-$ which would reduce to $Fe(OH)_3^-$ and then further reduce to Fe. The nature of the change in Tafel slope may depend on the concentration of iron. In 30 w/w KOH at 70°C, the presence of 0.5ppm of dissolved iron was reported to be detrimental to the hydrogen discharge, while at 37°C with the same KOH concentration, the presence of 3ppm of iron improved the electroactivity of the

nickel cathode [9]. In another study by Brossard et al., the presence of 14ppm of iron at 70°C, lowered the overpotential for the HER reaction. The authors concluded that the improved electrocatalytic activity was due to the formation of small crystallites of pure iron on the electrode substrate which reduced the Tafel slope[12]. As the pre-treated KOH in the present work contained trace amounts of dissolved iron, ~0.5ppm, the subsequent increase in overpotential may due to the iron-base metallic deposit. Evidence could be found from the electrode surface analysis in Fig.5.1.18 where iron was found deposited. As mentioned above, iron can deposit on the electrode surface even from almost undetectable low concentrations. This iron deposit has been shown to increase the HER overpotential even at concentrations less than 0.5ppm. The measured increase in overpotential could continue for 8 hours due to the fact that time is needed for the iron to deposit as mentioned by Brossard [12]. It took him almost 20 hours to obtain a detectable iron deposit using EDX. As the accumulation of iron increases, the overpotential increases.

After the sharp increase in overpotential (Fig. 5.1.7), a steady state potential is reached. This potential varied in the range from -1.9V to -2.3V versus Hg/HgO, i.e. an overpotential range between 966mV and 1366mV. As noted above, very low levels of iron can affect the overpotential. EDX analysis on the coating of the platinum electrode (Fig. 6.1) used for pre-electrolysis found that only iron was coated on

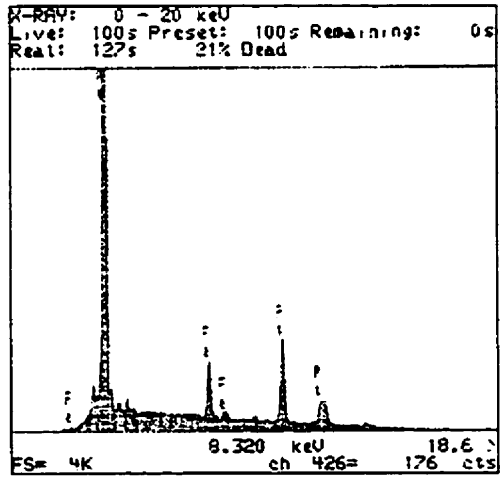

Fig. 6.1 : EDX spectrum on coating of the Pt pre-electrolysis electrode.

the electrode, even though the electrolytes were pre-electrolyzed for 48 hours. Differences in measured overpotentials may due to the different iron content in the electrolyte between different experiments. It was found that the pre-electrolyzed KOH still contained about 0.5 ppm of dissolved iron using ICP analysis of the treated electrolyte. Although a reduced value was expected, the combination of very low concentrations of Fe in an 300,000 ppm K matrix makes the accurate quantification difficult.

Surface finish of an electrode can be another factor for electrode potential since surface area of the electrode is affected which in turn, would change the electrode potential. However, since the electrodes were prepared using the same procedure, the surface finish effect should not be significant.

When the catalyst was added to the electrolyte, a sharp decrease in overpotential occurred. The drop was immediate and a new steady state value was reached in a short time (~ 0.5 hour). This drop was clearly due to the catalyst addition. The final potentials were in the range of -1.75 to -1.80V (overpotential range 775 - 825mV) versus Hg/HgO and did not depend on the catalyst concentration (>0.1ppm) in the electrolyte as can be seen in the potential versus time plots in sections 5.1.2 to 5.1.7. This means that the catalytic effect is not due to the presence of a homogeneous species in the electrolyte at catalyst concentrations higher than 0.1ppm. In section 6.1.3.3 below, vanadium species will be shown to have been deposited on the electrode surface.

6.1.3.2 Steady State Potentiostatic Measurements

Fig. 5.1.24 shows the Tafel plot for Ni-200 after 100ppm of vanadium addition. The Tafel plot contained two linear regions, with a Tafel slope of 84 ± 16 mV/dec. between the overpotential range of 100 and 550mV and a slope of 286 ± 56 mV between the range of 550 - 750mV. The Tafel slope of a vanadium stationary electrode could not be found in the literature, however a Tafel slope of 111mV/dec. was reported at a rotating vanadium electrode at a pH of about 10 in the overpotential range between 500 to 700mV versus Hg/HgO rotating at 2500 rev/min [67].

The Tafel value from the current study is high compared to this. However with a rotating electrode, there is a constant regeneration of reactant on the electrode surface and faster removal of bubbles than with a stationary electrode. Therefore, a rotating electrode might expect to display a smaller Tafel slope than a stationary one. Another reason for the differences of Tafel slopes may due to a difference in the nature of the electrode surface. A long term steady state galvanostatic measurement from the effect of catalyst addition was also plotted in the Fig. 5.1.25 for 250mA/cm^2. By extrapolating the Tafel line to 250mA/cm^2, it can be seem that the point matches the extrapolation. This suggests that all the Tafel data points were at steady state.

The Tafel behaviour of the catalyst modified electrode Tafel plot is different from that observed for the Ni-200 electrode. It has a smaller slope in the low overpotential region than the slope in the high potential region. The slope in the high overpotential range was about 300% higher than that for the Ni-200 electrode. This increase in Tafel slope does not imply that the catalyst has decreased the activity. In fact, the whole curve has shifted to higher current densities. This means that the catalyst modified electrode

has a higher activity than the Ni-200 electrode since it has a higher current at any given overpotential. In the low overpotential range, the Tafel slope was lower than 120mV/dec. showing that the rate determining step was moved towards the electrochemical reaction (Heyrovsky (10)) from the hydrogen adsorption reaction (Volmer (9)) as the theoretical Tafel slopes for Heyrovsky and Volmer reactions were 40 and 120 mV/dec. respectively. The HER mechanism may be a mixed controlled rate determining reaction. At high overpotential range, there is no reported mechanism for the HER at the Tafel slope above 120mV/dec.

6.1.3.3 Scanning Electron Microscopy (SEM) with EDX

The SEM micrographs and the corresponding EDX spectra of the electrode surface at different catalyst concentrations are presented in Sections 5.1.2 to 5.1.7. Except for the 0.1ppm catalyst addition, the electrode surface at all other catalyst concentrations was covered by a coating which contained vanadium. Nickel, vanadium, potassium and iron were the major peaks in most of the EDX spectra. The SEM micrographs showed that as the vanadium concentration increased, the thickness of the coating increased. The electrode surface after a 10ppm vanadium addition (Fig. 5.1.5) showed a rough, cracked surface. As the vanadium concentration increased (Fig. 5.1.8, 50ppm vanadium addition), multi-layers or laminations of coating began to develop. At higher vanadium concentrations, the coating contained several well developed layers as shown in Fig. 5.1.20. As the vanadium concentration in the electrolyte increased, the peak ratio of nickel to vanadium decreased. Since The nickel signal was from the Ni-200 substrate, when the vanadium rich coating increased in thickness, the signal of nickel

became weaker. Even with the highest level of addition (1000ppm), the nickel signal could still be seen (Fig. 5.1.21 for 1000ppm vanadium addition). Since x-rays of the EDX can penetrate the sample 1 to 2 μm depending on the sample material, the thickness of the coating should not exceed 2 μm even at a vanadium concentration of 1000ppm. Assuming the thickness of the coating for 1000ppm vanadium addition was 2 μm and using the nickel to vanadium peak ratio of the EDX spectrum, the thickness of the coating of 100, 50 and 10ppm of vanadium addition were estimated to be 1.4, 0.04 and 0.005 μm respectively (sample calculations in Appendix G). The atomic percentage of the elements was generated from the program in the EDX analyzer where corrections have been made for absorption and secondary fluorescence effect. However, since the coating and the Ni electrode were not homogeneous, inaccurate corrections would occur due to the matrix and grain effect. Therefore, the calculation from Appendix G only gives a rough estimation of the coating thickness.

Pre-electrolysis of the KOH solution reduced the iron content in the electrolyte to a very low level but still left in residual iron to be deposited together with vanadium on the electrode surface after prolonged polarization. However, this was not the only source of iron in the coating. Iron was present in the vanadium salt solution where it was an impurity at a level of 0.003%. Fig. 5.1.18 showed the SEM micrograph of the electrode surface after 0.1ppm vanadium addition. At very low vanadium concentration of 0.1ppm, no vanadium was found coated on the electrode surface. The surface was not "coated" as the polishing scratches could still be seen. There were many hexagonal crystallites deposited on the electrode surface. EDX spot analysis of the crystallites, iron containing crystals which deposit instead of vanadium. At high vanadium concentrations

(≥ 100ppm), the iron signal had disappeared in the EDX spectra. This indicated that iron was not co-deposited with vanadium and it was underneath the vanadium coating. Therefore, the major source of iron appears to arise from the potassium hydroxide electrolyte. The micrograph (Fig. 5.1.18) showed that the iron crystals were concentrated around the edge of the holes in the Ni-200 electrode. This may due to the active sites located on the edges of exposed dislocations [68].

A potassium signal can also be seen in the EDX spectra. The intensity varied with different experiments but because the potassium presence is difficult to avoid due to the electrolyte remaining on the electrode surface, no correlation with operating condition was performed.

6.1.3.4 X-ray Photoelectron Spectroscopy (XPS) and XRD

X-ray Photoelectron Spectroscopy was used to identify the vanadium species present in the Ni-200 electrode surface coating. Fig. 5.1.31 shows the XPS spectrum of oxygen (O 1s) and Fig. 5.1.32 shows the XPS spectrum of vanadium (V 2p 1/2, V 2p 3/2) from a vanadium addition of 100ppm. A quick reference of the literature and the experimental binding energies of the respective valence states of vanadium and oxygen and their associated valence state are given in Table 8. More detail was given in Table 5.1.2 and 5.1.3 in Section 5.1.11.

Table 8 : Binding Energies of vanadium and oxygen for XPS

Species	Binding Energies (eV) (present work)	Binding Energies (eV) (literature)	References
V2P$_{1/2}$			
V^{5+} (V_2O_5)	524.47	523.8, 524.4, 524.8, 524.3	54, 55, 56, 59
V^{4+} (VO_2)		523.1, 523.5	54, 59
V^{3+} (V_2O_3)	523.05	523, 523.2, 523.3	55, 58, 59
V		520.3, 519.7, 519.6, 519.9	54, 55, 56, 59
V2P$_{3/2}$			
V^{5+} (V_2O_5)	516.87	517.1, 517.5, 516.4, 517, 517.2, 518.1, 516.9	52, 53, 54, 55, 56, 57, 59
V^{4+} (VO_2)		516.1, 516.2	54, 59
V^{3+} (V_2O_3)	515.56	515.5, 516.6, 516.3, 515.7	55, 57, 58, 59
V		512.7, 512.1, 512, 512.4	54, 55, 56, 59
O1s			
V^{5+} (V_2O_5)	529.94	530.3, 530.4, 529.6, 529.8, 529.8	52, 53, 54, 55, 59
V^{4+} (VO_2)		529.8, 529.9	54, 59
V^{3+} (V_2O_3)	531.23	530.3, 530.7, 530.1	55, 58, 59

The analysis shows that the vanadium is present in the layer as V^{3+} and V^{5+} corresponding to the species V_2O_3 and V_2O_5 respectively. The binding energies of the experimental peaks correspond well with literature values. Note that it is difficult to distinguish the peaks of V^{4+} and V^{3+} . As shown in Table 8, the reported binding energies of the two species are just different by 0.1 eV or in some cases the values overlap. But from the result of the V2p$_{3/2}$ binding energy, it was clear that V^{3+} was present when compared to the literature values. The abundance of V_2O_5 present in the existing coating may not represent the coating in the solution phase. Since V_2O_3 is thermodynamically

unstable, it would react with oxygen in the air and be converted to V_2O_5. An attempt was made to obtain standard V_2O_3 and VO_2 XPS spectrum using high purity powder samples as a standard. The sample was prepared under argon gas in a glove bag. The resulting XPS spectrum indicated that the samples were composed of V_2O_5 with trace amount of the corresponding oxide species. Thus both V_2O_3 and VO_2 are unstable and will be converted to V_2O_5 after exposure to oxygen. According to the Pourbaix diagram, the stable species should be V_2O_3 or VO_2 at the experimental pH (pH calculations in Appendix C) and potential range. Therefore, the V_2O_5 could have formed on the surface after the electrode was removed from the cell.

Fig. 5.1.30 shows the result of the XRD analysis. No specific vanadium species could be identified from the spectrum. The only well developed peaks were the two nickel peaks which came from the nickel substrate when compared the experimental and literature values in Table 5.1.1. The other peaks were very small and some were almost undetectable as shown by their small intensities. The spectrum was used qualitatively to compare with the $Ni_{50}Co_{25}P_{15}B_{10}$ XRD spectrum.

6.1.4 Effect of Method of Catalyst Addition

This section will discuss the results presented in section 5.1.9. The effect of different catalyst addition methods to the electrochemical behaviour of the Ni-200 electrode will be discussed followed by their corresponding SEM and EDX spectra.

6.1.4.1 Chronopotentiometry

The chronopotentiograms of both addition methods were shown in Fig. 5.1.26. The final vanadium concentration of both experiments was 100ppm. The single addition experiment consisted of one 100ppm of vanadium addition to the electrolyte while the multiple addition test consisted of two 10ppm followed by two 20ppm and a final 40ppm additions in the time intervals about 500 to 1000 minutes between each addition which added to 100ppm of vanadium in the electrolyte after the final addition.

The electrochemical behaviour of both types of addition methods are the same. The potential response to the applied current density before the addition of vanadium had been discussed in section 6.1.3.1. The same principle would apply to the experiment with multiple catalyst additions during the period of time before the addition of catalyst.

After the vanadium addition, there was a sharp drop of overpotential for both experiments. When looking at the multiple addition test, the sharp drop of overpotential was due to the addition of the first 10ppm of vanadium. Further additions of vanadium into the electrolyte had no additional effect on the overpotential. The final potential of the multiple addition test was the same as one would get with single addition test (-1.75 to -1.80V versus Hg/HgO). This is consistent with the results of the single addition experiments which showed the final potential was not dependent on the vanadium concentration. The small drift of potential over time may due to the deposition of impurities from the electrolyte since this experiment was more than twice the duration of the usual experiments (116 hours).

6.1.4.2 Scanning Electron Microscope (SEM) with EDX

Fig. 5.1.27 showed the SEM micrographs and their corresponding EDX spectra of the electrode surface after 100ppm vanadium addition via both addition methods.

The single addition result was the same as discussed in section 6.1.3.3. The electrode surface was covered by a vanadium rich coating. In comparing the single and multiple addition experiments, the electrode coating with multiple vanadium additions had a similar coating to the single addition coatings. Cracks were found in the coatings for both experiments. Greater abundance of impurities were found in the multiple addition coating. Since each addition was done after the potential became steady, the long polarization time may allow more impurities to deposit. However, as the potential did not change after the first addition, these impurities did not have any significant effect on the potential. The presence of zinc in the coating may be due to the failure of the epoxy coating which was used to mask the electrode and the flux used in soldered connection at the back of the electrode to leach out (section 4.3.1) which contained zinc chloride. Nevertheless, the concentration of zinc was small compared to that of vanadium. From the above analyses, the morphology of the coatings were essentially identical for both addition methods.

6.2 Amorphous Nickel Base Alloy ($Ni_{50}Co_{25}P_{15}B_{10}$)

This section will discuss the result of homogeneous catalyst additions of vanadium using amorphous nickel base alloy ($Ni_{50}Co_{25}P_{15}B_{10}$) as the electrode material. These results will then be compared with the results obtained with Ni-200 electrodes.

6.2.1 Steady State Potentiostatic Measurements (Tafel)

Fig. 5.2.14 shows the Tafel plot of $Ni_{50}Co_{25}P_{15}B_{10}$. Two linear regions were found. In the low overpotential range, 50 - 550mV, the Tafel slope was found to be 350 ± 70 mV/dec. while at high overpotentials , 550 - 700mV, the Tafel slope was 173 ± 34 mV/dec. The decrease in Tafel slope at the high overpotential is consistent with the finding of Lian et al [37]. As shown in Table 4, different amorphous nickel base alloys had different Tafel slopes and two linear regions with smaller slopes at high overpotentials. A summary of $Ni_{50}Co_{25}P_{15}B_{10}$ Tafel slopes in different overpotential range is given in the following Table 9.

Table 9 : $Ni_{50}Co_{25}P_{15}B_{10}$ Tafel slopes in different overpotential range

Overpotential range (mV vs. Hg/HgO)	Tafel slope (mV/dec.)	Temperature (K)	Author
355 – 555	144	303	37
555 - 705	101	303	
240 - 440	189	343	72
50 - 550	350	343	present work
550- 750	173	343	

The transition point of the Tafel slopes in the present work was in reasonable agreement with Lian et al's result [37]. However, the slopes obtained in the present work were high when compared with Lian et al's. There are two possible reasons: (i) temperature and (ii) impurities. As the temperature was higher in the present study, the Tafel slope would

increase according to equation (16). Since the Tafel slope is directly proportional to temperature, the result of Lian et al when corrected to 343K should be 163 and 114 mV/dec. at low and high overpotentials respectively. However, the Tafel slopes were still small when compared with the present work measurements.

A second possible reason for the observed difference in Tafel slopes may be the effect of iron impurity in the electrolyte. Since Lian et al did not use pre-electrolysis in her procedure, the iron content in her electrolyte was higher than this study. Iron deposited on the electrode surface would reduce the Tafel slope at high iron concentration (>0.5 ppm) as discussed in Section 6.1.3.1. In an investigation by Huot on an amorphous alloy containing iron, the improved electrode activity is attributed to the formation of very fine iron particles on the amorphous matrix resulting from an electrochemical process which significantly reduces the Tafel slope and the overpotential of the HER [12]. In Lian et al's case, this was unlikely to happen and the surface deposit was a better explanation.

A 'long term' point from the results of chronopotentiometry experiments was included in Fig. 5.2.14. By extrapolating the line at high overpotential, it was noticed that the point was not on the line, showing that the Tafel data was not able to represent long term steady state values which may due to impurities deposition at long polarization.

In comparison with the nickel Tafel plot, the change in Tafel slopes were the same for both materials. $Ni_{50}Co_{25}P_{15}B_{10}$ had larger slopes than Ni-200 but had higher current densities over the sweep range, showing that $Ni_{50}Co_{25}P_{15}B_{10}$ was more catalytic than Ni-200 at a sweep rate 10 hours per step. Since there was a significant difference in Tafel behaviour at different sweep rates for Ni-200 as shown in Fig. 5.3.2, the

comparison with the literature may not be valid for the sweep rates were not the same. In the current study, the sweep rate of 10 hours per step was used in the Tafel plots of both electrode materials for comparison.

6.2.2 Scanning Electron Microscopy (SEM) with EDX

Fig. 5.2.1 showed the SEM micrograph of a polished $Ni_{50}Co_{25}P_{15}B_{10}$ electrode surface. The surface is featureless except for a small scratch shown in the left of the photo.

The corresponding EDX spectrum showed the well defined peaks for elements Ni, Co and P in the amorphous nickel base alloy. Boron was unable to be detected since the x-ray detector cannot detect elements with atomic weight less than carbon unless a thin window or a windowless detector is employed.

6.2.3 *Catalyst Coated Electrodes*

6.2.3.1 Chronopotentiometry

As with Ni-200, chronopotentiometry was performed at a nominal current density of -250 mA/cm^2. Three catalyst addition concentrations were chosen which included 50, 100 and 500ppm and compared with the results from Ni-200 electrodes (chronopotentiograms were shown in sections 5.2.2 to 5.2.5).

The electrochemical behaviour of $Ni_{50}Co_{25}P_{15}B_{10}$ was the same as nickel. There was a rapid increase in overpotential for the first 500 minutes of polarization before steady state was reached. The steady state potential varied from -1.95 to -2.10V

(overpotential range 1016 - 1166mV) from run to run. The same potential range was observed for Ni-200 electrodes.

A sharp drop of overpotential was obtained after the addition of vanadium into the electrolyte. The final potential after the catalyst addition was in the range of -1.7 to -1.8V (overpotential range 766 - 866mV). Similar to Ni-200, the final potential was reached in a very short time after the catalyst addition (for example, compare Fig 5.1.14 and Fig. 5.2.10 for 500ppm addition). However, in the 100ppm vanadium addition experiments, the potential stayed at -1.8V right after the addition and changed slowly until it reached another steady potential at -1.7V. This second transition was not detected in the 50 and 500ppm catalyst addition tests or in any of the Ni-200 results. No explanation could be found for this transition except that it was due to some common experimental feature of the three tests such as contamination present in the electrolyte. The morphology of coating will be discussed in section 6.2.3.3.

6.2.3.2 Steady State Potentiostatic Measurements (Tafel)

Fig. 5.2.15 showed the Tafel plot for $Ni_{50}Co_{25}P_{15}B_{10}$ after 100ppm of vanadium addition. Two linear regions were found. At low overpotentials, 100 - 500mV, a Tafel slope of 347 $\pm$ 65mV/dec. was obtained while at high overpotentials, 500 - 750mV, the Tafel slope was 133 $\pm$ 25 mV/dec.

Similar Tafel slopes were obtained in the catalyst coated electrodes and the non-coated ones, showing the same reaction mechanism was occurring on the surface of the uncoated and catalyst added substrate. The effect of vanadium addition on $Ni_{50}Co_{25}P_{15}B_{10}$ electrodes was not as significant as on Ni-200 since the curve did not

shift to higher current densities. In fact, vanadium had no catalytic effect on $Ni_{50}Co_{25}P_{15}B_{10}$ at low overpotentials. In Fig. 5.3.3, vanadium started to show a catalytic effect only at an overpotential of about 600mV. Above this value, a higher current density was obtained with coated $Ni_{50}Co_{25}P_{15}B_{10}$ electrode. The reason for this might due to that there were less adsorption sites on $Ni_{50}Co_{25}P_{15}B_{10}$ surface. Since Ni-200 had more macro scale metal defects than $Ni_{50}Co_{25}P_{15}B_{10}$ which provided more exposed edges where adsorption initiated. Also, as polarization continued nickel hydride was reported to form after long polarization, and cracks would appear on the nickel surface [29] which would provide more active adsorption site. At low overpotentials, vanadium did not have enough driving force to deposit on the electrode surface and therefore could not affect the electrochemical behaviour of the electrode. At high overpotentials, vanadium did deposit and therefore a catalytic effect was found.

The change of Tafel slope of $Ni_{50}Co_{25}P_{15}B_{10}$ was opposite to that observed on Ni-200 for it displayed a decrease in slope at high overpotentials. This could be explained by the ease of vanadium deposition. Since it is easier to deposit on the Ni-200 surface, vanadium starts to coat the Ni-200 electrode surface at a lower overpotential and therefore catalytic effect initiates right at the beginning. When the coating is developed, the reaction mechanism changed and thus a change in Tafel slope at low and high overpotentials was obtained for Ni-200. The same applies to $Ni_{50}Co_{25}P_{15}B_{10}$, since vanadium cannot coat the electrode surface for the reason discussed above, the Tafel slope did not change until high overpotentials. This is why a decrease in Tafel slope at high overpotentials was obtained for $Ni_{50}Co_{25}P_{15}B_{10}$.

6.2.3.3 Scanning Electron Microscopy (SEM) with EDX and XRD

SEM micrographs of coated electrode surfaces at different catalyst additions were presented in sections 5.2.2 to 5.2.5. There was an increase in the amount of coating as the concentration of vanadium increased. This was confirmed by the EDX spectrum. As the vanadium concentration increased, the peaks of the electrode elements decreased, showing that the thickness of the coating had increased. At 50ppm of vanadium addition, there appeared to be only a single coating layer and there were few cracks in the coating (Fig.5.2.4). For 100ppm, a second layer of coating was found (Fig. 5.2.7) while for 500ppm, the surface was covered by multiple coatings (Fig. 5.2.10). This coating morphology was the same as found on Ni-200. On Ni-200, the second layer was initiated at 50ppm vanadium addition which is lower than the 100ppm required for $Ni_{50}Co_{25}P_{15}B_{10}$. Using the Ni and vanadium peak ratio from the EDX spectrum, the thickness of the film on $Ni_{50}Co_{25}P_{15}B_{10}$ in 100ppm vanadium addition was estimated to be 0.84μm compared to 1.4μm for coating on Ni-200 electrode. This supports the discussion in the previous section that it was harder for vanadium to deposit on $Ni_{50}Co_{25}P_{15}B_{10}$.

Section 5.2.7 showed the XRD result of the coated $Ni_{50}Co_{25}P_{15}B_{10}$ surface. A very broad band 'peak' was present due to the amorphous nickel base substrate. A few small crystalline peaks were present which were almost exactly at the same position as found for the Ni-200 samples. Thus the coatings on Ni-200 and amorphous nickel were composed of the same component species. Since the amount of coating was small for XRD analysis, the analysis was performed at different geometrical positions for specific sections of the spectrum to improve resolution of the peaks and combined the data to

obtain one spectrum. Therefore, the peaks did not have a common reference calibration. Thus the spectrum could only be used qualitatively. The details of the coating components was discussed in section 6.1.3.4.

6.3 Effect of Pre-electrolysis of Electrolyte

This section will discuss the difference in results between using treated and non-treated electrolyte with Ni-200 electrodes. The treated electrolyte had lower iron contamination but was otherwise identical to the untreated electrolyte. It was found that the treated KOH contained about 0.5 ppm of iron while the non-treated KOH contained <5 ppm of iron as specified by the manufacturer.

6.3.1 Chronopotentiometry

Fig. 5.1.28 showed the chronopotentiograms of Ni-200 using treated and non-treated potassium hydroxide electrolytes with a 100ppm vanadium addition. There was a drop of overpotential after the addition of catalyst in both tests, but the steady potentials pre- and post-vanadium addition for the two tests were different.

The potential before vanadium addition using non-treated electrolyte was stabilized at -1.87V compared to -1.98V when using treated electrolyte. The potential difference may due to the different Fe content in the electrolytes. As mentioned in Section 6.1.3.1, the presence of 0.5ppm of dissolved iron was reported detrimental to the hydrogen discharge, while at 37°C with the same KOH concentration, the presence of 3ppm of Fe improved the electroactivity of the nickel cathode [9]. Since the non-treated KOH contained about 5 ppm of Fe, the electroactivity of the nickel cathode should be

improved. The -1.87V was close to the final potential recorded in the 0.1ppm vanadium addition test which showed vanadium did not make significant catalytic effect. Thus the catalytic effect was due to the deposition of iron crystallites on the electrode surface as discussed in sections 6.1.1 and 6.1.3.1. The presence of iron was further confirmed by the EDX analysis on the black coating found on the platinum cathode used for the pre-electrolysis of the electrolyte (Fig. 6.1). Nothing except iron was found in the coating showing that iron was the major impurity in the electrolyte which could be electrodeposited.

After the vanadium addition, a sharp drop of overpotential was detected for both experiments. Experiments using non-treated electrolyte had smaller overpotential drops.

The final potential for non-treated electrolyte was more catalytic than the treated one by 100mV. This difference was because of the different coating compositions. The high concentration of iron in the non-treated electrolyte would co-deposit simultaneously with vanadium on the electrode surface. This helped the HER probably by providing larger surface area, i.e. more active sites for reaction to occur.

6.3.2 Scanning Electron Microscopy (SEM) with EDX

A SEM micrograph of the coated Ni-200 electrode surface with 100ppm vanadium addition using treated and non-treated electrolyte and their EDX spectrum was provided in Fig. 5.1.29.

Using 100ppm vanadium addition tests for comparison, the SEM photo of the electrode surface using non-treated electrolyte shows a much thinner coating as indicated by the EDX spectrum. For the non-treated KOH, a large Ni peak was present with a

small vanadium peak, while a big vanadium peak was found with a very small Ni peak in the EDX spectrum with treated KOH. Since the strong nickel signal was due to the nickel substrate underneath the coating, therefore the coating with non-treated KOH was thinner. Using the Ni to vanadium peak ratio, the coating thickness was estimated to be 0.03μm for non-treated KOH compared to 1.4μm for treated KOH. The reason might be that iron inhibits vanadium to deposit which prevented the formation of a thick vanadium coating.

6.4 Proposed Reaction Mechanism of Catalysis Process

A reaction mechanism will be proposed in this section based on the results discussed in the previous sections.

As shown from the Tafel plots in Fig. 5.1.24 and 5.1.25, there was a change of the reaction mechanism of the HER on Ni-200 before and after the vanadium addition as indicated by a change in Tafel slope. The reason for the Tafel slope change was due to the change in electrode surface material from Ni to vanadium coating. This coating resulted in a decrease in overpotential. In order to cause a catalytic effect, the vanadium species on the electrode surface must change the electronic and geometric configuration of the reactants which increased the reaction rate. For maximum activity, the surface should have an intermediate heat of formation or adsorption for hydrogen as stated by the Principle of Sabaties [37]. At both very low and very high heats of adsorption, the chemisorption will be either too weak to support the reaction or too stable resulting in the formation of a stable compound which will lower the activity of the electrode. The elements which optimize the chemisorption criterion are transition metals. Among these,

group VIII metals exhibit maximum activity. Their high activity is reported to be due to their high percentage d-band character [37]. This percentage reflects the extent of filling up of d shells by dsp hybridization. The unpaired d-band electrons in the metal can pair with unpaired electrons from H and chemisorption occurs. Since transition metals with high percentage d-band character have intermediate heat of hydrogen adsorption, they thus have high catalytic activities. As a member of group VIII, nickel should have a higher catalytic activity than vanadium (group V). However, during prolonged cathodic polarization, nickel hydride forms which changes the surface structure of the nickel electrode. The hydrogen absorption changes the d-character of the metal to a s-p character for the intermetallic Ni-H. This results in a decrease in percentage d-character of the metal which reduces the number of available electrons and consequently lowers electrode activity [29]. This hydride formation effect was seen in the Tafel data in Fig. 5.3.2. As the time between each step increased, the electrode activity decreased (i.e. i_o decreased). With vanadium coating on the electrode, the reacting surface became active again likely because of the higher percentage d-band character of vanadium oxide compared to nickel hydride. The i_o of the vanadium coated electrode increased to a value closer to the initial nickel Tafel plot (1/2 hour step rate, Table 5.3.1). The coated electrodes attained a stable potential much faster than nickel, and this may due to the small affinity for hydrogen by vanadium oxides. In the cathodic reduction of V_2O_5 , a low hydrogen content phase of $H_xV_2O_5$ forms where $x<0.5$ as -OH in the molecule, and it has almost identical lattice structures as V_2O_5 [76].

Since there was a change in Tafel slope after the vanadium was coated on the electrodes, a change in reaction mechanism was expected. Since the Tafel slopes of the

coated electrodes were above 120 mV/dec at the high overpotential range, the HER reaction pathway would no longer be Volmer (9) followed by Heyrovsky (10). Theoretically from equations (16) and (17), for a high Tafel slope (>120mV/dec), the rate determining step must be a chemical reaction with no electron transfer step before it in the mechanism. Using the literature for the mechanism of anodic dissolution of vanadium in alkaline solution [67], the following reaction mechanism is proposed to account for the catalytic role of vanadium on the electrode:

$$V_2O_5 + 6OH^- \Leftrightarrow 2VO_4^{3-} + 3H_2O \qquad (20)$$

$$3H_2O + 2VO_4^{3-} \Leftrightarrow (V_xO_y)_{ads} + 6OH^- \qquad (21)$$

$$(V_xO_y)_{ads} + OH^- \Leftrightarrow (V_xO_y \bullet OH^-)_{ads} \qquad (22)$$

$$(V_xO_y \bullet OH^-)_{ads} + H_2O + e^- \Leftrightarrow H_2 + (V_xO_y)_{ads} + 2OH^- \qquad (23)$$

Reaction (20) and (21) would occur at the beginning of the experiment and when V_xO_y was formed, reaction (22) and (23) would become self-sustaining steps. Reaction (22) would be the rate determining step and is not an electron transfer step, hence the Tafel slope assumes a large value (>120mV/dec). Since the adsorbed vanadium oxide could be V^{3+} or V^{5+} according to the XPS results, a mixed V_xO_y is used in the proposed mechanism.

For the case of $Ni_{50}Co_{25}P_{15}B_{10}$, the nickel hydride effect was not as significant as with Ni-200. The Tafel plot before and after vanadium addition showed similar electrode activities except at high current density (~250mA/cm^2). Also, the change in Tafel slopes on the coated $Ni_{50}Co_{25}P_{15}B_{10}$ electrode was different from that of the coated Ni-200 (Fig.5.3.4). As mentioned above (section 6.2.3.2), this could due to the poorer vanadium

coating formation. The hydrogen adsorption on partially coated electrode surface would be affected resulting in different Tafel slopes.

Another factor for the increase in catalytic activity is the increase in active surface area. As mentioned by Huot, the improved electroactivity of Ni-200 cathodes in the presence of an iron deposit was ascribed to the increased active surface area [9]. This is also true in the present work. Vanadium deposits on the electrode surface which increased the active surface area of the electrode. Using the Tafel data of Ni-200 before and after vanadium addition (Fig. 5.1.24 and 5.1.25), the amount of electrode active surface area increased corresponding to the amount of shift of the Tafel line with a slope of 286mV/dec. is calculated (Appendix E). The area is 80 times larger with the coated electrode. This area increase is not unreasonable comparing data for a very high surface area material, Raney nickel. Fig. 6.2 and 6.3 shows the SEM image of the Raney nickel coated surface and the vanadium coated surface with 100ppm addition respectively.

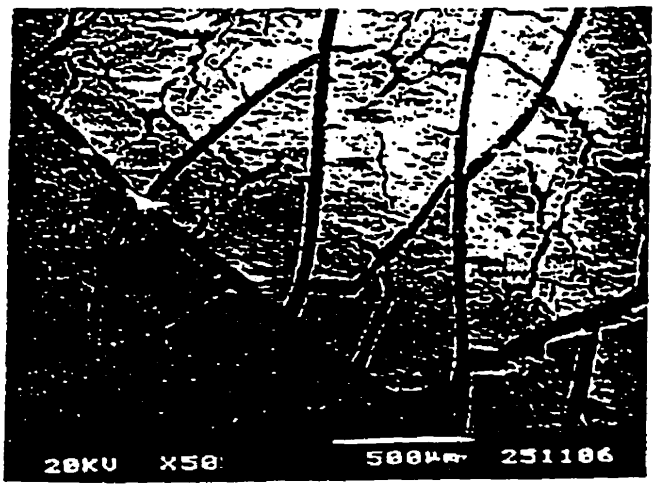

Fig. 6.2 Surface of a Raney nickel coated electrode.

Fig. 6.3 Surface of vanadium coated electrode (100 ppm addition)

For Raney nickel electrode, the specific area was roughly 10^4 cm^2 per cm^2 apparent area with a coating thickness of ~50μm [28]. In comparison with the vanadium electrode, Raney Ni has much larger cracks (a magnified vanadium coated image is given in Fig. 5.1.11) and much larger specific area. However, the thickest vanadium coating was ~2μm, thus it should correspond to 400 cm^2 per cm^2 apparent area using Raney nickel's standard. Moreover, the lack of cracks on the vanadium coating would reduce the active surface area by a significant amount since the active area under the surface coating could not be used. Given that the specific area of a polished nickel surface is 2 cm^2 per cm^2 apparent area and comparing with the Raney nickel coating of 10^4 cm^2 per cm^2 apparent area, the vanadium coated electrode at about 80 cm^2 per cm^2 apparent area is a reasonable value. However, the final potential did not change much between experiments thus indicating similar active surface area. Thus the increase in active surface area could not be responsible for the entire overpotential drop since the coating surface areas could not be identical in different experiments.

From the above discussion, the catalytic effect appears to be due to the formation of the coating without involving any homogeneous specie. More evidence comes from the fact that if homogeneous catalysis is involved, the degree of the catalytic effect should be catalyst concentration dependent. However, the results did not show any of this dependency. Moreover, the Tafel slope of $Ni_{50}Co_{25}P_{15}B_{10}$ did not change at low overpotentials which implied that no catalytic effect and modification of the reaction mechanism was present in the absence of the vanadium coating. In the case of the coated electrodes, the hydrogen would probably be adsorbed on the hydrated vanadium metallic intermediate or salt species. Since the vanadium coating was re-dissolved into the

electrolyte immediately after the applied current was halted, the coating should be composed of vanadium salt which contained V^{3+} and V^{5+} ions.

More research is required to definitively identify the mechanism by which vanadium catalyzed the HER. The following conclusions can be drawn from the work.

7. CONCLUSIONS

For electrodes with prolonged polarization at 250mA/cm^2, 8M KOH at 70°C:

1. The addition of vanadium to the electrolyte lowers the cathodic overpotential for the HER for both Ni-200 and $Ni_{50}Co_{25}P_{15}B_{10}$ electrodes. The time required for the catalyst effect to occur was less than 30 minutes and was very rapid compared to the time required to stabilize the uncatalyzed electrode.
2. Vanadium is found in the coatings of both Ni-200 and $Ni_{50}Co_{25}P_{15}B_{10}$ electrodes and is associated with the catalytic effect observed with vanadium addition to the electrolyte.
3. The final potential after catalyst addition is not dependent on the catalyst concentration except for very low catalyst concentrations. For catalyst concentrations $\leq$0.1ppm, the electrode did not produce sufficient vanadium coverage to provide a full catalytic effect.
4. The morphology of electrode coating is not dependent on the method of vanadium addition. However thicker coatings were observed with higher vanadium solution loadings and these coatings have multiple layers and a mud crack structure.
5. The reaction mechanism of the HER after vanadium addition is a complex mechanism which involves adsorbed vanadium oxide species.

6. Iron impurities which are almost impossible to completely remove from the electrolyte alter the surface of the Ni-200 electrodes which increase the their electroactivity by forming Fe crystals on the electrode surface which increase the active surface area. They also affect the morphology of the vanadium coatings in forming thin coatings which increase the vanadium catalytic effect slightly.
7. The Tafel slopes of Ni-200 is dependent on the step time between each data point. Electrode deactivation continues over very long time frames and makes comparison of Tafel data from the literature very difficult since many different stabilization times are used. In the current work, there was a decrease in the exchange current density fom 2.14 to 0.004 mA/cm^2 for measurements at 0.5 hour per data point to 10 hours per data point.

8. REFERENCES

1 Viktor Engelhardt, " The Electrolysis of Water Processes and Applications ", The Chemical Publishing Company, 1904, P. 1-3.

2 American Machinist, June 1991, P.23.

3 A. G. Barnstaple, A. J. Petrella, " Hydrogen A Challenging Opportunity ; Hydrogen Supply, A Report Prepared for the Ontario Hydrogen Energy Task Force.", Ontario Hydro, Vol. 3, Sept. 1981.

4 M. P. S. Ramani, " Electrolytic Hydrogen Production ", Progress in Hydrogen Energy, Reidel Publishing Company, 1987, P. 15-29.

5 Joseph G. Santangelo, W. Norvis Smith, " Hydrogen : Production and Marketing ", American Chemical Society, 1980, P. 191-212.

6 John Redman, " Electrolysis for High Purity Gases ", The Chemical Engineer, Vol. 482, Sept. 27, 1990, P. 18.

7 Kirk-Othmer, " Encyclopedia of Chemical Technology ", 4th Ed. John Wiley & Sons, Inc., Vol. 13, 1995, P. 852-885.

8 J. Y. Huot, " Hydrogen Evolution and Interface Phenomenon a Nickel Cathode in 30 w/o KOH ", J. Electrochem. Soc., Vol. 136, No. 7, The Electrochemical Society, Inc., July 1989, P. 1933-1939.

9 J. Y. Huot, L. Brossard, " Time Dependence of the Hydrogen Discharge at 70°C on Nickel Cathodes ", Int. J. Hydrogen Energy, Vol. 12 No. 12, Pergamon Journals Ltd., 1987, P. 821-830.

10 G. I. Lacconi, H. M. Villullas, V. A. Macagno, " The Effect of Metallic Impurities on the Hydrogen Evolution Reaction Rate on Group-Ib Metals in Alkaline Solution ", J. Applied Electrochemistry, Vol. 21, Chapman & Hall Ltd., 1991, P. 1027-1030.

11 L. Brossard, " Electrocatalytic Performance for Alkaline Water Electrolysis of Ni Electrodes Electrocoated with Fe or Fe/Mo ", Int. J. Hydrogen Energy, Vol. 16, No. 1, Pergamon Press , 1991, P. 13-21.

12 L. Brossard, J. Y. Huot, " Influence of Iron Impurities on Time Dependence of the Hydrogen Evolution Reaction on Platinum Cathodes During Electrolysis of 30 w/o KOH ", J. Applied Electrochemistry, Vol. 19, Chapman & Hall Ltd., 1989, P. 882-888.

13 Alexander A. Kamnev, Boris B. Ezhov, " Electrocatalysis of Anodic Oxygen Evolution at the Nickel Hydroxide Electrode by Ferric Hydroxo Species in Alkaline Electrolytes ", Electrochimica Acta, Vol. 37, No. 4, Pergamon Press, 1992, P. 607-613.

14 L. Brossard, " Oxygen Discharge on Nickel and Cobalt Anodes in 30 w/o KOH at 70°C in the Presence of Dissolved Iron and Vanadium ", Int. J. Hydrogen Energy, Vol. 16, No. 2, Pergamon Press, 1991, P. 87-92.

15 L. Brossard, " O_2 Evolution on Nickel After Preanodization in 30 wt% KOH in the Presence of Dissolved Cobalt ", Mater. Chem. Phys., Vol. 28, 1991, P. 213-226.

16 Dennis A. Corrigan, " The Catalysis of the Oxygen Evolution Reaction by Iron Impurities in Thin Film Nickel Oxide Electrodes ", J. Electrochem. Soc., The Electrochemical Society, Inc., Vol. 134, No. 2, Feb. 1987, P. 377-384.

17 Amoy K. Cheong, Andrzej Lasia, J. Lessard, " Hydrogen Evolution Reaction at Composite-Coated Raney Nickel Electrodes in Aqueous and Aqueous-Methanolic Solutions ", J.. Electrochem. Soc, Vol.140, No.10, The Electrochemical Society, Inc., Oct. 1993, P. 2721-2725.

18 Andrzej Lasia, Dany Gregoire, " General Model of Electrochemical Hydrogen Absorption into Metals ", J. Electrochem. Soc., Vol.142, No. 10, The Electrochemical Society, Inc., Oct. 1995, P. 3393-3399.

19 Andrzej Lasia, Linlin Chen, " Influence of the Adsorption of Organic Compounds on the Kinetics of the Hydrogen Evolution Reaction on Ni and Ni-Zn Alloy Electrodes ", J. Electrochem. Soc., Vol. 139, No. 4, The Electrochemical Society, Inc., Apr. 1992, P. 1058-1064.

20 J. Fournier et al., " Hydrogen Evolution Reaction in Alkaline Solution ", J. Electrochem. Soc., Vol. 143, No. 3, The Electrochemical Society, Inc., Mar. 1996, P. 919-926.

21 R. L. LeRoy, A. K. Stuart, " Advanced Unipolar Electrolysis ", Hydrogen Energy Progress, Proceedings of the 3rd World Hydrogen Energy Conference, Jun. 1998, P. 1817-1830.

22 K. Christiansen, T. Grundt, " Large Scale Hydrogen Production Technology, Experience and Application ", Proceedings of the Symposium on Industrial Water Electrolysis, Vol. 78-4, 1978, P. 24-38.

23 C. J. Winter, J. Nitsch, " Hydrogen as an Energy Carrier, Technologies, Systems, Economy ", Springer-Verlag Berlin Heidelberg, 1988, P. 190-205.

24 Y. Yurum, " Hydrogen Energy System, Production and Utilization of Hydrogen and Future Aspects ", Kluwer Academic Publishers, 1995, P. 69-82, 49-51, 95-110.

25 F. R. Foulkes, " Electrochemistry 553F ", course notes, 1996, P. 35-1 to 35-8.

26 M. F. Kibria, M. Sh. Mridha, A.H. Khan, " Electrochemical Studies of a Nickel Electrode for the Hydrogen Evolution Reaction ", Int. J. Hydrogen Energy, Vol.20, No. 6, Pergamon Press, 1995, P. 435-440.

27 H. E. G. Rommal, P.J. Moran, " Time-Dependent Energy Efficiency Losses at Nickel Cathodes in Alkaline Water Electrolysis Systems ", J. Electrochem. Soc., Vol. 132, No. 2, The Electrochemical Society, Inc., Feb. 1985, P. 325-329.

28 S. Rausch, H. Wendt, " Morphology and Utilization of Smooth Hydrogen-Evolving Raney Nickel Cathode Coatings and Porous Sintered-Nickel Cathodes ", J. Electrochem. Soc., Vol. 143, No. 9, The Electrochemical Society, Inc., Sept. 1996, P. 2852-2862.

29 D. M. Soares, O. Teschke, I. Torriani, " Hydride Effect on the Kinetics of the Hydrogen Evolution Reaction on Nickel Cathodes in Alkaline Media ", J. Electrochem. Soc., Vol. 139, No. 1, The Electrochemical Society, Inc., Jan. 1992, P. 98-105.

30 A. C. Chialvo, M. R. Gennero De Chialvo, " Electrocatalytic Activity of Nickel Black for the Hydrogen Evolution Reaction in Alkaline Solutions ", J. Applied Electrochemistry, No. 21, Chapman & Hall Ltd., 1991, P. 440-445.

31 J. Y. Hout, L. Brossard, " In Situ Activation of Nickel Cathodes by Sodium Molybdate during Alkaline Water Electrolysis at Constant Current ", J. Applied Electrochemistry, No. 20, Chapman & Hall Ltd., 1990, P. 281-288.

32 L. Brossard, J. Y. Hout, " In Situ Activation of Cathodes during Alkaline Water Electrolysis by Dissolved Iron and Molybdenum Species ", J. Applied Electrochemistry, No. 21, Chapman & Hall Ltd., 1991, P. 508-515.

33 F. E. Luborsky, " Amorphous metallic alloys ", Amorphous Metallic Alloys, Chapter 1, Butterworths, 1983, P. 1-7.

34 M. Shibata, T. Masumoto, " Amorphous Alloys as Catalysts or Catalyst Precursors ", Preparation of Catalysts IV, Elsevier Science Publichers, 1987, P. 353-371.

35 H. Komiyama, A. Yokoyama, " Catalytic Properties of Amorphous $Fe_{40}Ni_{40}P_{40}B_{40}$ Ribbons ", Symposium on Structure & Properties of Amorphous Metals, Series A, Vol. 28, 1980, P. 217-221.

36 K. Hashimoto, " Chemical Properties ", Amorphous Metallic Alloys, Chapter 24, Butterworths, 1983, P. 471-486.

37 K. Lian, " The Electrocatalytic Behaviour of Ni-Co Alloys for the Hydrogen Evolution Reaction in Alkaline Solution ", University of Toronto Master's Thesis, 1990.

38 " Corrosion Resistance of Nickel and Nickel Alloys ", Chapter 15, Metals Handbook, American Society for Metals, U.S., 1991, P. 23.

39 Thorne, Stevenson, Kellogg, "Hydrogen A Challenging Opportunity ; Hydrogen Supply, A Report Prepared for the Ontario Hydrogen Energy Task Force.", Vol. 2, Sept. 1981.

40 H. Suzuki, " Production and Electrochemical Behaviour of Ni-Co-Mo-B Amorphous Alloys for Alkaline Water Electrolysis ", University of Toronto Master's Thesis, 1993

41 V. Yu. Karpov et al., " Application of Hydrogenation for the Refining and Pulverization of Metals ", Int. J. Hydrogen Energy, Vol 21, No. 11/12, Pergamon Press, 1996, P. 919-922.

42 T. N. Veziroglu, " Hydrogen Movement and the Next Action: Fossil Fuels Industry and Sustainability Economics ", Int. J. Hydrogen Energy, Vol. 22, No.6, Pergamon Press, 1997, P. 551-556.

43 H. Vandenborre and R. Sierens, " Greenbus: A Hydrogen Fuelled City Bus ", Int. J. Hydrogen Energy, Vol. 21, No.6, Pergamon Press, 1996, P. 521-524.

44 W. Peschka, " Hydrogen: The Future Cryofuel in Internal Combustion Engines", Int. J. Hydrogen Energy, Vol. 23, No. 1, Pergamon Press, 1998, P.27-43.

45 K. Yamane et al., " Somw Performance of engine and Cooling System of LH_2 Refrigerator Van Musashi-9 ", Int. J. Hydrogen Energy, Vol. 21, No. 9, Pergamon Press, 1996, P. 807-811.

46 A. Contreras et al., " Hydrogen as Aviation Fuel: A Comparison with Hydrocarbon Fuels ", Int. J. Hydrogen Energy, Vol. 22, No. 10/11, Pergamon Press, 1997, P. 1053-1060.

47 P. Millet et al., " Design and Performance of a Solid Polymer Electrolyte Water Electrolyzer ", Int. J. Hydrogen Energy, Vol. 21, No. 2, Pergamon Press, 1996, P. 87-93.

48 Y. Tadokoro et al. " Technical Evaluation of UT-3 Thermochemical Hydrogen Production Process for an Industrial Scale Plant ", Int. J. Hydrogen Energy, Vol. 22, No. 1, Pergamon Press, 1997, P. 49-56.

49 J. R. Benemann, " Feasibility Analysis of Photobiological Hydrogen Production", Int. J. Hydrogen Energy, Vol. 22, No. 10/11, Pergamon Press, 1997, P. 979-987.

50 T. Bergene, " The Efficiency and Physical Principles of Photolysis of Water by Microalgae ", Int. J. Hydrogen Energy, Vol. 21, No. 3, Pergamon Press, 1996, P. 189-194.

51 L. Brossard, B. Marquis, " Electrocatalytic Behavior of Co/Cu Electrodeposits in 1M KOH at 30°C " Int. J. Hydrogen Energy, Vol. 19, No. 3, Pergamon Press, 1994, P. 231-237.

52 V. I. Nefedov, Ya. V. Salyn, " A Comparison of Different Spectrometers and Charge Corrections Used in X-ray Photoelectron Spectroscopy ", J. Electron Spectroscopy and Related Phenomena, Vol.10, Elsevier Scientific Publishing Co., 1977, P. 121-124.

53 V. I. Nefedov, M. N. Firsov, I. S. Shaplygin, " Electronic Structures of $MRhO_2$, MRh_2O_4, $RhMO_4$ and Rh_2MO_6 on the Basis of X-ray Spectroscopy and ESCA Data ", J. Electron Spectroscopy and Related Phenomena, Vol.26, Elsevier Scientific Publishing Co., 1982, P. 65-78.

54 J. Kasperkiewicz, J. A. Kovacich, D. Lichtman, " XPS Studies of Vanadium and Vanadium Oxides ", J. Electron Spectroscopy and Related Phenomena, Vol.32, Elsevier Scientific Publishing Co., 1983, P. 123-132.

55 R. J. Colton, A.M. Guzman, J. W. Rabalais, " Electrochromism in Some Thin-film Transition-metal Oxides Characterized by X-ray Electron Spectroscopy ", J. Appl. Phys. Vol. 49, No. 1, Jan. 1978, P. 409-416.

56 J. F. Moulder, W. F. Stickle, P. E. Sobol, K. D. Bomben, " Handbook of X-ray Photoelectron Spectroscopy ", Perkin-Elmer Crop. Physical Electronics Div., 1992.

57 N. K. Nag, F. E. Massoth, " ESCA and Gravimetric Reduction Studies on V/Al_2O_3 and V/SiO_2 Catalysts ", Journal of Catalysis, Academic Press Inc., Vol. 124, 1990, P. 127-132.

58 R. L. Kurtz, V. E. Henrich, " Surface Electronic Structure and Chemisorption on Corundum Transition-metal Oxides : V_2O_3 ", Physical Review B, Vol. 28, No. 12, Dec. 15, 1983, P. 6699-6706.

59 G. A. Sawatzky, D. Post, " X-ray Photoelectron and Auger Spectroscopy Study of Vanadium Oxides ", Physical Review B, Vol. 20, No. 4, 1979.

60 D.C. Harris, " Quantitative Chemical Analysis ", 3rd Ed., W.H. Freeman and Co., 1991, P. AP36.

61 V.M.M. Lobo, " Handbook of Electrolyte Solutions ", Part A, Elsevier, 1989, P. 69.

62 " CRC Handbook of Chemistry and Physics ", 51st Ed., 1970-71, The Chemical Rubber Co., P. D-143.

63 W.F. Smith, " Principles of Materials Science and Engineering ", 2nd Ed., McGraw-Hill, 1990, P. 162.

64 W. Jost, " Diffusion in Solids, Liquids, Gases ", Academic Press Inc., 1960, P.130.

65 M.H. Armbruster, " Solubility of Hydrogen at Low Pressure in Iron and Nickel", J. Am. Chem. Soc., vol. 65, 1943, P. 1043-1054.

66 M.C. Stemp," Homogeneous Catalysis in Alkaline Water Electrolysis ", University of Toronto Master's Thesis, 1997.

67 M. Privman, T. Hepel, " Electrochemistry of Vanadium Electrodes, Part 2. Anodic and Cathodic Polarization over a Wide Range of pH and Temperature", J. of Electroanal. Chem., Elsevier, vol. 382, 1995, P. 145-152.

68 L. Angely, G. Bronoel, G. Peslerbe, " Relation Between Nickel Crystalline Structures and Their Electrocatalytic Properties, Part 2, Determination of the Nature of Adsorption Sites for Hydrogen ", J. of Electroanal. Chem., Elsevier, vol. 96, 1979, P. 191-201.

69 G. Kreysa, B. Hakansson, J. Electroanal. Chem., vol. 201, 1986, P. 61.

70 M. F. Kibria, M. SH. Mridha, A.H. Khan, Int. J. Hydrogen Energy, vol. 20, 1995, P. 435.

71 C. J. Cochran, " Electrochemical Study of the Hydrogen Evolution Reaction on Nickel-Palladium-Phosphorous Amorphous Metal Alloys for use in Alkaline Hydrogen Systems ", University of Toronto Master's Thesis, 1996.

72 D. Anthony, University of Toronto Master's Thesis, in progress.

73 Index to the Powder Diffraction File, American Society for Testing and Materials, 1972.

74 D. C. Silverman, " Revised EMF-pH Diagram for Nickel ", National Association of Corrosion Engineers, Vol. 37, No. 9, Sept.1981, P. 546-548.

75 D. C. Silverman, " Presence of Solid $Fe(OH)_2$ in EMF-pH Diagram for Iron ", National Association of Corrosion Engineers, Vol. 28, No. 8, Aug. 1982, P. 453- 455.

76 S.J. Hibble, A.M. Chippindale, P.G. Dickens, " Hydrogen Insertion at a Vanadium Pentoxide Cathode ", J. Electrochem. Soc., Vol. 132, No. 11, The Electrochemical Society, Inc., Nov. 1985, P. 2668-2669.

Appendix A

Calculation for Hydrogen Equilibrium Potential, ϕ, at 70°C

Cathodic Reaction: $2H_2O + 2e^- \rightarrow 2OH^- + H_2$ $\phi°_{25°C} = -0.829V$ vs. SHE

Using Nernst Equation:

$$\phi_{SHE}^{70°C} = \phi°_{70°C} - \frac{RT}{nF}\ln\left(\frac{a_{OH^-}^2 \, a_{H_2}}{a_{H_2O}^2}\right) \qquad \text{(i)}$$

$\phi°_{70°C} = \phi°_{25°C} + d\phi°/dT$ where $d\phi°/dT = -0.8360$ mV/K [60]

$= -0.829-(0.826)(45)/(1000)$

$= -0.886V$

For a_{OH^-} :

$a_{OH^-} = \gamma_{\pm} \, m_{OH^-}$ (assume $\gamma_{OH^-} = \gamma_{\pm}$)

where $\gamma_{\pm} = 3.374$ [61],

30% KOH = 7.639 mol/kg

Therefore : $a_{OH^-} = (3.274)(7.639)$

$= 25.77$

For a_{H_2O} :

$a_{H_2O} = P_{H_2O,70°C,8M\ KOH} / P_{H_2O,70°C,pure}$

where $P_{H_2O,70°C,8M\ KOH} = 18849$ Pa
(Properties of Aqueous Solutions, from Andrei Tchouvchev)
$P_{H_2O,70°C,pure} = 31157$ Pa [62]

Therefore : $a_{H_2O} = 11849/31157$

$= 0.604$

For a_{H_2} :

$a_{H_2} = P_{H_2} = 1 - P_{H_2O}$ (assume 1 atm in hydrogen bubbles)

$= 1 - 0.186$

$= 0.814$

Put back all values into (i) :

$$\phi_{SHE}^{70°C} = \phi°_{70°C} - \frac{RT}{nF}\ln\left(\frac{a_{OH^-}^2 \, a_{H_2}}{a_{H_2O}^2}\right)$$

$= -0.866 - (8.314)(343)/(2)(96486)\ln((25.77)^2(0.814)/(0.604)^2)$

$= -0.975$ V

Since the experiments were done with reference electrode at 25°C, the variation of SHE was found to be +0.91mV/K, therefore :

$\phi°_{25°C} = -0.975 \text{ V} + (0.91/1000)(70-25)$

$= -0.975 + 0.04$

$= -0.934$V

Appendix B

Calculation of Equilibrium Potential of Hg/HgO versus SHE at 25°C

Reference Electrode Reaction : $HgO + H_2O + 2e^- \Leftrightarrow Hg + 2OH^-$

where $\phi^\circ_{25°C,Hg/HgO}$ = -0.0976 V vs. SHE

Using Nernst Equation:

$$\phi_{25°C,Hg/HgO} = \phi^\circ_{25°C,Hg/HgO} - \frac{RT}{F} \ln \frac{a_{OH^-}}{\sqrt{a_{H_2O}}} \qquad \text{(ii)}$$

For a_{OH^-} :

$a_{OH^-} = \gamma_\pm m_{OH^-}$

where $\gamma_\pm$ = 3.65 [61],

30% KOH = 7.639 mol/kg

Therefore : a_{OH^-} = (3.65)(7.639)

= 27.9

For a_{H_2O} :

$\psi = -1000\, a_{H_2O} / (\upsilon m M_w)$

where ψ = osmotic coefficient = 1.91 [61]

υ = number of ions in the molecule = 2

M_w = molecular weight of water = 18g

m = molal of KOH = 7.639 mol/kg

Therefore :

a_{H_2O} = 0.591

Put back all values into (ii):

$$\phi_{25°C,Hg/HgO} = \phi°_{25°C,Hg/HgO} - \frac{RT}{F}\ln\frac{a_{OH^-}}{\sqrt{a_{H_2O}}}$$

$$= 0.0976 - (8.314)(298)/(96486)\ln(27.9/(0.591)^{0.5})$$

$$= 0.0054 \text{ V vs. SHE}$$

Appendix C

Calculation of pH

$K_w = a_{H^+} \cdot a_{H_2O}$

$-\log a_{H^+} = \log a_{OH^-} - \log K_w$

$= \log a_{OH^-} - pK_w$

$= pH$

At 70°C,

$pK_w = 12.728$ [60]

$a_{OH^-} = 25.77$ (from Appendix A)

Therefore :

$pH = \log 25.77 + 12.728$

$= 14.14$

Appendix D

Calculation of the Amount of Hydrogen Diffused into Nickel

Diffusion in nickel can be expressed by [63] :

$$\frac{C_s - C_x}{C_s - C_o} = erf\left(\frac{x}{2\sqrt{Dt}}\right) \qquad \text{(iii)}$$

where C_s = surface concentration of element in gas diffusing into the surface (mol/L),

C_o = initial uniform concentration of element in solid (mol/L),

C_x = concentration of element at distance x from surface at time t (mol/L),

x = distance from surface (m)

D = diffusivity of diffusing solute element (m^2/s)

t = time (s)

Diffusivity of hydrogen in nickel can be expressed as [64] :

$$D = 2.04 \times 10^{-3} \exp(-18700/RT)$$

At 70°C :

$$D = 2.04 \times 10^{-3} \exp(-18700/(8.314)(343))$$

$$= 2.89 \times 10^{-6} \text{ cm}^2/\text{s}$$

$$= 2.89 \times 10^{-10} \text{ m}^2/\text{s}$$

Thickness of nickel sheet : 4.5×10^{-4} m

Huot and Brossard [32] suggested that the first hour of deactivation process was ascribed to hydrogen absorption. Therefore 1 hour is used as the time in this calculation.

Put values into equation (iii):

$$\frac{C_s - C_x}{C_s - C_o} = erf\left(\frac{4.5x10^{-4}}{2\sqrt{2.89x10^{-10}\ x\ 3600}}\right)$$

$$= \text{erf}\,(0.22)$$

$$= 0.2$$

Therefore the hydrogen concentration in the nickel electrode is 20% of the hydrogen concentration on the surface of the nickel electrode.

Appendix E

Calculation of Electrode Area Enhancement by the Coating

Using exchange current density ratio for calculation,

From Fig. 5.1.24 (with no vanadium addition) :

log of exchange current density at overpotential range of 150 - 550mV = -2.39

exchange current density at overpotential range of 150 - 550mV = 0.004

From Fig. 5.1.25 (with 100 ppm vanadium addition) :

log of exchange current density at overpotential range of 550 - 750mV = -0.49

exchange current density at overpotential range of 550 - 750mV = 0.32

The number of times of area increased :

0.32/0.004 = 80

Therefore, the coating has increased the active electrode surface area by 80 times.

Appendix F

Modification of Data Compiling Program

Before compile the chronopotentiometry tests data, the following modification is needed to applied to the program.

First go to the hokuto program, in the main menu choose option 8, then choose 1 following by option 3. After pressing 3, press ctrl plus break together.

List the following line and make corrections:

Line 540 becomes : dfile$(1)=dfile$(1)

Line 1155 becomes : print "Output file will be:" ;ddr$+dfile$(1)+".prn"

Line 1160 becomes : open ddr$+dfile$(1)+".prn" for output as #2

Appendix G

Sample Calculation of Coating Thickness

Assume coating thickness of 1000ppm vanadium addition is 2μm (Ni-200).

From EDX data:

$$\frac{\text{Atom\% Ni}}{\text{Atom\% V}} = \frac{7.981}{68.178} = 0.117$$

For 100ppm vanadium addition:

$$\frac{\text{Atom\% Ni}}{\text{Atom\% V}} = \frac{9.321}{54.392} = 0.17$$

Using peak ratio:

$$\text{Thickness of coating for 100ppm vanadium addition} = \frac{0.117}{0.17} \times 2\ \mu m = 1.4\mu m$$

Coating Thickness (Estimation)

Vanadium Concentration	Coating Thickness (μm)
(Ni-200) 1000 ppm	2
500 ppm	2.3
100 ppm	1.4
50 ppm	0.04
10 ppm	0.005
Using Non-Treated KOH (100ppm)	0.03
$(Ni_{50}Co_{25}P_{15}B_{10})$ 100ppm	0.84